UNIVERSITÀ DEGLI STUDI DI SALERNO

Dipartimento di Matematica

Dottorato di Ricerca in Matematica
XIV ciclo - Nuova serie

Cardiovascular System: Modelling and Optimization

Candidato: **D'Arienzo Maria Pia**

Coordinatore: **Chiar.ma Prof.ssa Patrizia Longobardi**

Tutor: **Chiar.mo Prof. Ciro D'Apice**

Cotutor: **Prof.ssa Rosanna Manzo**

Anno Accademico 2014-2015

Contents

VI

List of Figures

X

XII

XIII

List of Tables

Introduction

A conservation law is a partial differential equation, in which the variable is a quantity which remains constant in time, that is it cannot be created and destroyed. Thanks to the conservation laws it is possible to define models able to describe real systems in which something is stored. Fluid dynamic models, which are based on them, have a wide range of applications, because they can be used to describe blood flows, traffic evolution on street networks of big cities or on motorways of big states, data flows on telecommunication networks, flows of goods on supply chains, electric networks, etc.

The model of the blood flow in the cardiovascular system will be treated in this thesis. Because of the increasing request from the medical community of scientifically and rigorous investigations about cardiovascular diseases, which are the cause of about the 40% of death, the research in this field is very active. Most of these disturbs are connected to arteriosclerosis, which leads to ictus, hearth attacks, etc. It is a common practice, in the vascular surgery, to face vascular and coronaries diseases by doing a bypass, but sometimes it fails. So, it is very important to have a better understanding of the local hemodynamic, such that the doctor can understand how different surgeries' solutions influences blood circulation and he/she can be led to the choice of the best procedure for the specific patient. All this is possible thanks to the study realized with numerical simulations, less invasive of *in vivo* investigations, and more accurate respect to *in vitro* ones.

The development of mathematical models of the cardiovascular system hails from the latest three decades, since the first centuries

before Christ, when some of the main characters of the human history studied and analyzed blood circulation, such as Aristotele, Prassagora, Galeno, Harvey, Bernoulli, Eulero, Poiseuille, Young, Frank, Womersley.

The models currently known can be classified according to the dimension, which goes from 0-D to 3-D, the prefixed goals and the required accuracy. In 0-D models with lumped parameters, the parameters are distributed spatially in a discrete way, that is all the elastic, inertial or resistive effect is concentrated in one point and it represents the global behavior of a certain district (organ, vessel, part of a vessel). They are developed in order to simulate the dynamics of the blood flow in the entire cardiovascular system, and they often use the hydraulic-electric analogy. These models can be divided in two categories: *mono-compartment models* in which increasing levels of sophistication are used to capture the systemic response, and *multi-compartment models*, in which the different parts of the vascular system are represented as distinct components. Higher-dimension models, instead, permit the variation of the parameters in the space with continuity (so models with distributed parameters are used), and they can include the term of the convective acceleration (non-linear). One of the advantages for such models is that they can reveal the detailed pressure and the distribution of the velocity in a specific segment of the vascular network, but limited computational resources restrict the dimension of the studied domain. That is why the 1-D model is usually chosen for the study of the variations of pressure and flow along the whole length of the considered vessel. During the latest years multi-scale modeling techniques have been developed, in which 0-D models are coupled with 1-D, 2-D and/or 3-D models, to give complete representations of the cardiovascular system.

The thesis is organized as follows. The conservation laws will be introduced, which are characterized by the fact that, for smooth initial data, the solution of the Cauchy problem can have discontinuities in finite time. To have global solutions it is necessary to work in a class of discontinuous functions, and look for weak entropic solutions. This will be done in chapter 1. Since the

definition of such solutions is not restrictive enough to guarantee the uniqueness of the solution for the corresponding Riemann and Cauchy problems, some admissibility conditions will be proposed, such as vanishing viscosity, entropy inequality, Lax condition.

The chapter 2 will be dedicated to a brief description of the cardiovascular system and a classification of the models of blood flow, considering different dimensions.

The attention will be focused on a specific 1-D model in chapter 3. In particular, in such model, the arteries are seen like thin, homogeneous and elastic tubes, while the blood like a homogeneous, incompressible and Newtonian fluid. The governing equations will be analyzed through the characteristic method and they will be solved using the discontinuous Galerkin method and a two-step time integration scheme of Adam-Bashfort. A linearized model will be studied too, to obtain analytic solutions. To make this model realistic, also inflow and outflow boundary conditions are considered.

In chapter 4 some numeric results are presented, using different formulations of the model and different types of networks. In particular, four optimization scenarios on artificial networks are investigated, such as the effect that truncation in a fractal network has to the flow in the root edge, the effect that adding or subtracting an edge has to the network dynamics, the effect that growth of a given network has on the dynamics when a desired total outflow is obtained and optimization of the heart rate in the event of a blockage/unblockage of an edge or of an entire subtree. In addition, the simulation of the tilt table test is performed, considering the 55-edge tree with the main arteries of the cardiovascular system, modeling the cardiac valve. Finally, an optimization scenario including the convective term in the mathematical formulation is presented, in order to optimize heart rate and terminal reflection coefficient, to obtain a desired pressure.

Chapter 1

Conservation Laws

The model presented in this thesis is based on conservation laws, which are special partial differential equations, where the variable is a *conserved quantity*, i.e. a quantity which can neither be created nor destroyed.

In this chapter some basic preliminaries about systems of conservation laws are given.

1.1 Definitions

Definition 1. *A system of conservation laws in one space dimension is a system of the form*

$$\begin{cases} \partial_t u_1 + \partial_x f_1(u) = 0, \\ \vdots \\ \partial_t u_n + \partial_x f_n(u) = 0. \end{cases} \tag{1.1.1}$$

It can be written as

$$u_t + f(u)_x = 0, \tag{1.1.2}$$

where $u = (u_1, ..., u_n) : [0, +\infty[\times \mathbb{R} \to \mathbb{R}^n$ *is the "conserved quantity" and* $f = (f_1, ..., f_n) : \mathbb{R}^n \to \mathbb{R}^n$ *is the flux.*

Remark 2. ***The scalar case****. If* $n = 1$, u *takes values in* $\mathbb{R}$ *and* $f : \mathbb{R} \to \mathbb{R}$, *then (1.1.2) is a single equation. In this case it is said that (1.1.2) is a scalar equation.*
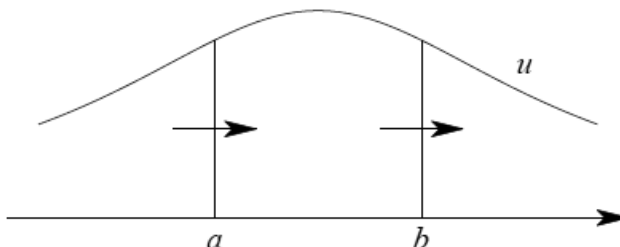
Figure 1.1   Conservation of flux.

In the scalar case, if (1.1.2) is integrated on an arbitrary space interval $[a, b]$, then

$$\frac{d}{dt} \int_a^b u(t, x)dx = - \int_a^b f(u(t, x))_x dx = f(u(t, a)) - f(u(t, b)).$$

In other words, the quantity u is neither created nor destroyed: the total amount of u in any interval $[a, b]$ can change only due to the quantity of u entering and exiting at $x = a$ and $x = b$.
f is always assumed to be smooth, thus, if u is a smooth function, then (1.1.2) can be rewritten in the quasi linear form

$$u_t + A(u)u_x = 0, \tag{1.1.3}$$

where $A(u)$ is the Jacobian matrix of f at u.

Definition 3. *The system (1.1.3) is said hyperbolic if, for every $u \in R^n$, all the eigenvalues of the matrix $A(u)$ are real. Moreover (1.1.3) is said strictly hyperbolic if it is hyperbolic and if, for every $u \in \mathbb{R}^n$, the eigenvalues of the matrix $A(u)$ are all distinct.*

It is clear that equations (1.1.2) and (1.1.3) are completely equivalent for smooth solutions. If instead u has a jump, the quasilinear equation (1.1.3) is in general not well defined, since there is a product of a discontinuous function $A(u)$ with the distributional derivative, which in this case is a Dirac measure.

Example 4. *(Gas dynamics). The Euler equations describing the evolution of a non viscous gas take the form*

$$\rho_t + (\rho v)_x = 0, \qquad \text{(conservation of mass)}$$
$$(\rho v)_t + (\rho v^2 + p)_x = 0, \qquad \text{(conservation of momentum)}$$
$$(\rho E)_t + (\rho E v + p v)_x = 0, \qquad \text{(conservation of energy)}.$$

Here ρ is the mass density, v is the velocity while $E = e + v^2/2$ is the energy density per unit mass. The system is closed by a costitutive relation of the form $p = p(\rho, e)$, giving the pressure as a function of the density and the internal energy. The particular form of p depends on the gas under consideration.

A basic feature for the nonlinear system (1.1.2) is that classical solutions may not exist for some positive time, even if the initial datum is smooth. This can be shown by the method of characteristics, briefly described for a quasilinear system.
Consider the Cauchy problem

$$\begin{cases} u_t + a(t, x, u) u_x = h(t, x, u), \\ u(0, x) = \bar{u}(x), \end{cases} \tag{1.1.4}$$

and, for every $y \in \mathbb{R}$, the curves $x(t, y)$, $u(t, y)$ solving

$$\begin{cases} \frac{dx}{dt} = a(t, x, u), \\ \frac{du}{dt} = h(t, x, u), \\ x(0, y) = y, \\ u(0, y) = \bar{u}(y). \end{cases} \tag{1.1.5}$$

The curves $t \mapsto x(t, y)$ when $y \in \mathbb{R}$ are called characteristics. The implicit function theorem implies that the map

$$(t, y) \mapsto (t, x(t, y)) \tag{1.1.6}$$

is locally invertible in a neighborhood of $(0, x_0)$ and so it is possible to consider the map $u(t, x) = u(t, y(t, x))$ where $y(t, x)$ is the inverse of the second component of (1.1.6). It is easy to check that $u(t, x)$ satisfies (1.1.4).

Example 5. *Consider the scalar conservation law (inviscid Burgers' equation)*

$$u_t + \left(\frac{u^2}{2}\right)_x = 0 \qquad\qquad (1.1.7)$$

with the initial condition

$$u(0, x) = u_0(x) = \frac{1}{1 + x^2}. \qquad\qquad (1.1.8)$$

For $t > 0$ small the solution can be found by the method of characteristics. Indeed, if u is smooth, la (1.1.7) is equivalent to

$$u_t + u\, u_x = 0,$$

from which is get that the directional derivative of the function $u = u(t, x)$ along the vector $(1, u)$ vanishes.
Therefore, u must be constant along the characteristic lines in the (t, x)-plane:

$$t \to (t, x + t u_0(x)) = \left(t, x + \frac{t}{1 + x^2}\right).$$

For $t < T \doteq \frac{8}{\sqrt{27}}$, these lines do not intersect (see Figure 1.2). The solution to the Cauchy problem is thus given implicitly by:

$$u\left(t,\ x + \frac{t}{1 + x^2}\right) = \frac{1}{1 + x^2}. \qquad\qquad (1.1.9)$$

On the other hand at $t = \frac{8}{\sqrt{27}}$ the characteristics intersect together and a classical solution can not exist for $t \geq \frac{8}{\sqrt{27}}$. In fact, the map

$$x \to x + \frac{t}{1 + x^2}$$

is not one-to-one and (1.1.9) no longer defines a single valued solution of the Cauchy problem.

To achieve a global existence result, it is thus essential to work within a class of discontinuous functions. Hence it is indispensable to deal with weak solutions.
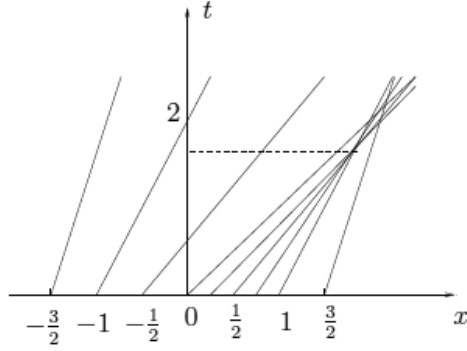
Figure 1.2 The characteristic for the Burgers equation in the (t, x)-plane.

Definition 6. *Fix $u_0 \in L^1_{loc}(\mathbb{R}; \mathbb{R}^n)$ and $T > 0$. A function $u :$ $[0, T] \times \mathbb{R} \to \mathbb{R}^n$ is a weak solution to the Cauchy problem*

$$\begin{cases} u_t + f(u)_x = 0, \\ u(0, x) = u_0(x), \end{cases} \qquad (1.1.10)$$

if u is continuous as a function from $[0, T]$ into L^1_{loc} and if, for every C^1 function ψ with compact support contained in the set $]-\infty, T[\times\mathbb{R}$, it holds

$$\int_0^T \int_R \{u \cdot \psi_t + f(u) \cdot \psi_x\} \, dx dt + \int_R u_0(x) \cdot \psi(0, x) dx = 0.$$
$$(1.1.11)$$

Notice that a weak solution u to (1.1.10) satisfies

$$u(0, x) = u_0(x) \quad \text{for a.e. } x \in \mathbb{R}.$$

This is a consequence of the fact that u is continuous as a function from $[0, T]$ to L^1_{loc} and of equation (1.1.11).
Weak solutions may develop discontinuities in finite time. Some notations are introduced to treat such discontinuities.

Definition 7. *A function $u = u(t, x)$ has an approximate jump discontinuity at the point (τ, ξ) if there exist vectors $u^-, u^+ \in \mathbb{R}^n$*

and $\lambda \in \mathbb{R}$ such that

$$\lim_{r \to 0^+} \frac{1}{r^2} \int_{-r}^{r} \int_{-r}^{r} |u(\tau + t, \xi + x) - U(t, x)| \, dx dt = 0,$$

where

$$U(t, x) := \begin{cases} u^-, & \text{if } x < \lambda t, \\ u^+, & \text{if } x > \lambda t. \end{cases} \tag{1.1.12}$$

The function U is called a shock travelling wave.

The following theorem holds.

Theorem 8. *Consider a bounded weak solution u to (1.1.2) with an approximate jump discontinuity at (τ, ξ). Then*

$$\lambda(u^+ - u^-) = f(u^+) - f(u^-). \tag{1.1.13}$$

Equation (1.1.13), called Rankine-Hugoniot condition, gives a condition on discontinuities of weak solutions of (1.1.2) relating the right and left states with the "speed" λ of the "shock". In the scalar case (1.1.13) is a single equation and, for arbitrary $u^- \neq u^+$, there is

$$\lambda = \frac{f(u^+) - f(u^-)}{u^+ - u^-}.$$

For a $n \times n$ system of conservation laws, (1.1.13) is a system of n scalar equations.

Example 9. *Consider the Burgers equation*

$$u_t + \left(\frac{u^2}{2} \right)_x = 0 \tag{1.1.14}$$

with the initial condition

$$u_0(x) = \begin{cases} 1 - |x|, & \text{if } x \in [-1, 1], \\ 0, & \text{otherwise.} \end{cases} \tag{1.1.15}$$

The characteristics in this case are drawn in Figure 1.3.
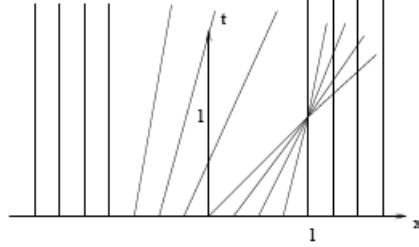
Figure 1.3 Superposition of characteristic curves for a Burgers equation.

Therefore for $0 \leqslant t < 1$, the function

$$u(t,x) = \begin{cases} \frac{x+1}{t+1}, & \text{if } -1 \leqslant x < t, \\ \frac{1-x}{1-t}, & \text{if } t < x \leqslant < 1, \\ 0, & \text{otherwise,} \end{cases}$$

is a classical solution to (1.1.14). The Rankine-Hugoniot condition in the case of Burgers equation reduces to

$$\lambda = \frac{\left[\frac{(u^+)^2}{2}\right] - \left[\frac{(u^-)^2}{2}\right]}{u^+ - u^-} = \frac{u^+ + u^-}{2}.$$

If $t \geqslant 1$, then the function

$$u(t,x) = \begin{cases} \frac{x+1}{t+1}, & \text{if } -1 \leqslant x \leqslant -1 + \sqrt{2+2t}, \\ 0, & \text{otherwise,} \end{cases}$$

satisfies the Rankine-Hugoniot condition at each point of discontinuity and so a weak solution to the Cauchy problem (1.1.14)-(1.1.15) exists for each positive time; see Figure 1.4.

Example 10. *Let u_0 be the function defined by*

$$u_0(x) := \begin{cases} 1, & \text{if } x \geqslant 0, \\ 0, & \text{if } x < 0. \end{cases}$$

For every $0 < \alpha < 1$, the function $u_\alpha : [0, +\infty[\times \mathbb{R} \to \mathbb{R}$ defined by

$$u_\alpha(t,x) := \begin{cases} 0, & \text{if } x < \frac{\alpha t}{2}, \\ \alpha, & \text{if } \frac{\alpha t}{2} \leqslant x < \frac{(1+\alpha)t}{2}, \\ 1, & \text{if } x \geqslant \frac{(1+\alpha)t}{2}, \end{cases}$$
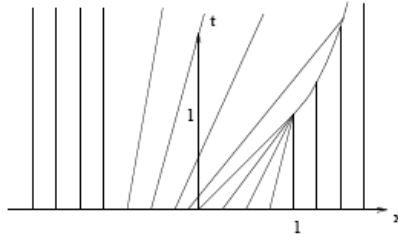
Figure 1.4 Solution to Burgers equation of the example.
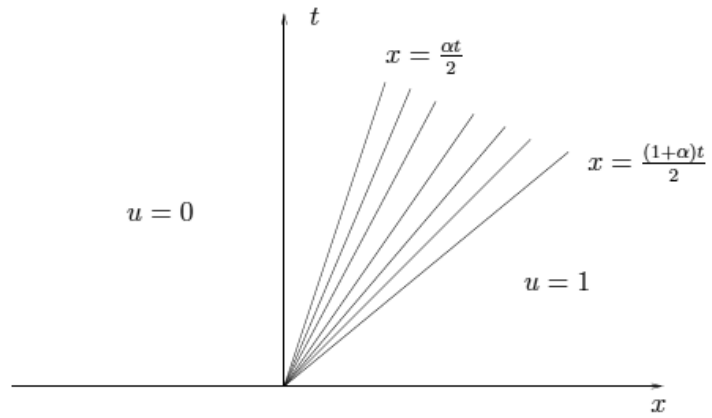
Figure 1.5 A solution u_α.

is a weak solution to the Burgers equation (1.1.14); see Figure 1.5.

1.2 Admissibility conditions

Example 10 shows that, in the presence of discontinuities, the Rankine-Hugoniot equations may not suffice to single out a unique solution to the Cauchy problem. Therefore, the notion of weak solution must be supplemented with admissibility conditions, motivated by physical considerations.

1.2.1 Admissibility Condition 1

Definition 11. *(Vanishing viscosity) A weak solution $u = u(t, x)$ to the Cauchy problem*

$$\begin{cases} u_t + f(u)_x = 0, \\ u(0, x) = u_0(x), \end{cases} \qquad (1.2.16)$$

is admissible if there exists a sequence of smooth solutions u^ε to

$$u_t^\varepsilon + A(u^\varepsilon)u_x^\varepsilon = \varepsilon u_{xx}^\varepsilon \qquad (A \doteq Df) \qquad (1.2.17)$$

which converges to u in L_{Loc}^1 as $\varepsilon \to 0^+$.

Unfortunately, it is very difficult to provide uniform estimates to the parabolic system (1.2.17) and characterize the corresponding limits as $\varepsilon \to 0^+$. From the above condition, however, one can deduce other conditions which can be more easily verified in practice.

1.2.2 Admissibility Condition 2

An admissibility criterion, coming from physical considerations, is that of the entropy-admissibility condition.

Definition 12. *A C^1 function $\eta : \mathbb{R}^n \to \mathbb{R}$ is an entropy for (1.1.2) if it is convex and there exists a C^1 function $q : \mathbb{R}^n \to \mathbb{R}$ such that*

$$D\eta(u) \cdot Df(u) = Dq(u) \qquad (1.2.18)$$

for every $u \in \mathbb{R}^n$. The function q is said an entropy flux for η. The pair (η, q) is said entropy–entropy flux pair for (1.1.2).

Definition 13. *(Entropy inequality) A weak solution $u = u(t, x)$ to the Cauchy problem (1.2.16) is said entropy admissible if, for every C^1 function $\varphi \geqslant 0$ with compact support in $[0, T[\times \mathbb{R}$ and for every entropy–entropy flux pair (η, q), it holds*

$$\int_0^T \int_{\mathbb{R}} \{\eta(u)\varphi_t + q(u)\varphi_x\}\, dxdt \geqslant 0. \tag{1.2.19}$$

Now an entropy admissible solution u and a sequence of entropy–entropy flux pairs (η_ν, q_ν) are considered, such that $\eta_\nu \to \eta$ and $q_\nu \to q$ locally uniformly in $u \in \mathbb{R}^n$. If $\varphi \geqslant 0$ is a C^1 function with compact support in $[0, T[\times \mathbb{R}$, then

$$\int_0^T \int_{\mathbb{R}} \{\eta_\nu(u)\varphi_t + q_\nu(u)\varphi_x\}\, dxdt \geqslant 0 \tag{1.2.20}$$

for every $\nu \in \mathbb{N}$. Passing to the limit as $\nu \to +\infty$ in (1.2.20), it is obtained that

$$\int_0^T \int_{\mathbb{R}} \{\eta(u)\varphi_t + q(u)\varphi_x\}\, dxdt \geqslant 0. \tag{1.2.21}$$

This permits to call a C^0 function η an entropy if there exists a sequence of entropies η_ν converging to η locally uniformly. Moreover a C^0 function q is a corresponding entropy flux if there exists a sequence q_ν, entropy flux of η_ν, converging to q locally uniformly. It is possible consider the scalar Cauchy problem (1.2.16), where $f : \mathbb{R} \to \mathbb{R}$ is a C^1 function. In this case the relation between C^1 entropy and entropy flux takes the form

$$\eta'(u)f'(u) = q'(u). \tag{1.2.22}$$

Therefore if it is taken a C^1 entropy η, every corresponding entropy flux q has the expression

$$q(u) = \int_{u_0}^u \eta'(s)f'(s)ds,$$

where u_0 is an arbitrary element of $\mathbb{R}$.
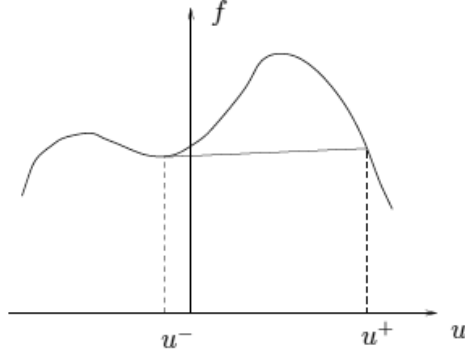
Figure 1.6 The condition (1.2.23) in the case $u^- < u^+$.

Definition 14. *A weak solution $u = u(t, x)$ to the scalar Cauchy problem (1.2.16) satisfies the Kruzkov entropy admissibility condition if*

$$\int_0^T \int_{\mathbb{R}} \{|u - k| \, \varphi_t + sgn \, (u - k) \, (f(u) - f(k)) \, \varphi_x\} \, dxdt \geqslant 0$$

for every $k \in \mathbb{R}$ and every C^1 function $\varphi \geqslant 0$ with compact support in $[0, T[\times\mathbb{R}$.

There is the following theorem.

Theorem 15. *Let $u = u(t, x)$ be a piecewise C^1 solution to the scalar equation (1.2.16). Then u satisfies the Kruzkov entropy admissible condition if and only if along every line of jump $x = \xi(t)$ the following condition holds. For every $\alpha \in [0, 1]$*

$$\begin{cases} f(\alpha u^+ + (1 - \alpha)u^-) \geqslant \alpha f(u^+) + (1 - \alpha)f(u^-), & \text{if } u^- < u^+, \\ f(\alpha u^+ + (1 - \alpha)u^-) \leqslant \alpha f(u^+) + (1 - \alpha)f(u^-), & \text{if } u^- > u^+, \end{cases}$$
$$(1.2.23)$$

where $u^- := u(t, \xi(t)-)$ and $u^+ := u(t, \xi(t)+)$.

Equation (1.2.23) implies that, if $u^- < u^+$, then the graph of f remains above the segment connecting $(u^-, f(u^-))$ to $(u^+, f(u^+))$ (see Figure 1.6), while if $u^- > u^+$, then the graph of f remains below the segment connecting $(u^-, f(u^-))$ to $(u^+, f(u^+))$ (see Figure 1.7).
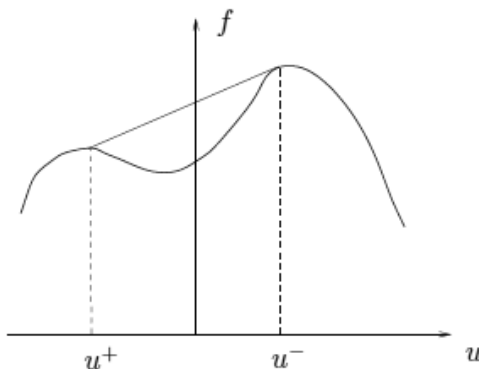
Figure 1.7 The condition (1.2.23) in the case $u^- > u^+$.

1.2.3 Admissibility Condition 3

Definition 16. *(Lax Condition) A bounded weak solution $u = u(t, x)$ to the Cauchy problem (1.2.16) is Lax admissible if, at every point of approximate jump, the speeds corresponding to the left and right states u^-, u^+ satisfy*

$$\lambda_i(u^-) \geq \lambda_i(u^-, u^+) \geq \lambda_i(u^+) \tag{1.2.24}$$

for some $i \in \{1, ..., n\}$.

1.3 Riemann Problem

This section describes the entropy admissible solutions to a Riemann problem, i.e. a Cauchy problem with Heaviside initial data. Let $\Omega \subseteq \mathbb{R}^n$ be an open set, let $f : \Omega \to \mathbb{R}^n$ a smooth flux and consider the system of conservation laws

$$u_t + f(u)_x = 0, \tag{1.3.25}$$

which it is supposed to be strictly hyperbolic.

Definition 17. *A Riemann problem for the system (1.3.25) is the Cauchy problem for the initial datum*

$$u_0(x) := \begin{cases} u^-, & \text{if } x < 0, \\ u^+, & \text{if } x > 0, \end{cases} \tag{1.3.26}$$

where $u^-, u^+ \in \Omega$.

As shown in Section 1.5, the solution of Riemann problems is the key step to solve Cauchy problems. In fact to prove existence the wave-front tracking method is used, that, roughly speaking, consists in the following:

1. approximate the initial condition with piecewise constant solutions;

2. at every point of discontinuity solve the corresponding Riemann problem;

3. approximate the exact solution to Riemann problems with piecewise constant functions and piece them together to get a function defined until two wave fronts interact together;

4. repeat inductively the previous construction starting from the interaction time;

5. prove that the functions so constructed converge to a limit function and prove that this limit function is an entropy admissible solution.

As before $A(u)$ denotes the Jacobian matrix of the flux f and with $\lambda_1(u) < \cdots < \lambda_n(u)$ the n eigenvalues of the matrix $A(u)$. For strictly hyperbolic systems, one can find bases of right and left eigenvectors, $\{r_1(u), \ldots, r_n(u)\}$, and $\{l_1(u), \ldots, l_n(u)\}$ depending strictly on u, such that

1. $|r_i(u)| \equiv 1$ for every $u \in \Omega$ and $i \in \{1, \cdots, n\}$;

2. for every $i, j \in \{1, \cdots, n\}$,

$$l_i \cdot r_j := \begin{cases} 1, & \text{if } i = j, \\ 0, & \text{if } i \neq j. \end{cases}$$

The following notation is introduced. If $i \in \{1, \cdots, n\}$, then

$$r_i \bullet \lambda_j(u) := \lim_{\varepsilon \to 0} \frac{\lambda_j(u + \varepsilon r_i(u)) - \lambda_j(u)}{\varepsilon},$$

that is the directional derivative of $\lambda_j(u)$ in the direction of $r_i(u)$.

Definition 18. *The i-characteristic field, $i \in \{1, \cdots, n\}$, is genuinely nonlinear if*

$$r_i \bullet \lambda_i(u) \neq 0 \qquad \forall u \in \Omega.$$

The i-characteristic field ($i \in \{1, \cdots, n\}$) is linearly degenerate if

$$r_i \bullet \lambda_i(u) = 0 \qquad \forall u \in \Omega.$$

If the i-th characteristic field is genuinely nonlinear, then, for simplicity, it is assumed that $r_i \bullet \lambda_i(u) > 0$ for every $u \in \Omega$.
Three cases are considered.

1. Centered rarefaction waves. For $u^- \in \Omega$, $i \in \{1, \cdots, n\}$ and $\sigma > 0$, $R_i(\sigma)(u^-)$ denotes the solution to

$$\begin{cases} \frac{du}{d\sigma} = r_i(u), \\ u(0) = u^-. \end{cases} \qquad (1.3.27)$$

   Let $\bar{\sigma} > 0$. Define $u^+ = R_i(\bar{\sigma})(u^-)$ for some $i \in \{1, \cdots, n\}$. If the i-th characteristic field is genuinely nonlinear, then the function

$$u(t,x) := \begin{cases} u^-, & \text{if } x < \lambda_i(u^-)t, \\ R_i(\sigma)(u^-), & \text{if } x = \lambda_i(R_i(\sigma)(u^-))t, \ \sigma \in [0, \bar{\sigma}], \\ u^+, & \text{if } x > \lambda_i(u^+)t, \end{cases}$$

$$(1.3.28)$$

   is an entropy admissible solution to the Riemann problem

$$\begin{cases} u_t + f(u)_x = 0, \\ u(0, x) = u_0(x), \end{cases}$$

   with u_0 defined in (1.3.26). The function $u(t, x)$ is called a centered rarefaction wave.

2. Shock waves. Fix $u^- \in \Omega$ and $i \in \{1, \cdots, n\}$. For some $\sigma_0 > 0$, there exist smooth functions $S_i(u_-) = S_i : [-\sigma_0, \sigma_0] \to \Omega$ and $\lambda_i : [-\sigma_0, \sigma_0] \to \mathbb{R}$ such that:

   (a) $f(S_i(\sigma)) - f(u^-) = \lambda_i(\sigma)(S_i(\sigma) - u^-)$ for every $\sigma \in [-\sigma_0, \sigma_0]$;

(b) $\left|\frac{dS_i}{d\sigma}\right| \equiv 1$;

(c) $S_i(0) = u^-$, $\lambda_i(0) = \lambda_i(u^-)$;

(d) $\frac{dS_i(\sigma)}{d\sigma}\big|_{\sigma=0} = r_i(u^-)$;

(e) $\frac{d\lambda_i(\sigma)}{d\sigma}\big|_{\sigma=0} = \frac{1}{2}r_i \bullet \lambda_i(u^-)$;

(f) $\frac{d^2 S_i(\sigma)}{d\sigma^2}\big|_{\sigma=0} = r_i \bullet r_i(u^-)$.

Let $\bar{\sigma} < 0$. Define $u^+ = S_i(\bar{\sigma})$. If the i-th characteristic field is genuinely nonlinear, then the function

$$u(t, x) := \begin{cases} u^-, & \text{if } x < \lambda_i(\bar{\sigma})t, \\ u^+, & \text{if } x > \lambda_i(\bar{\sigma})t, \end{cases} \tag{1.3.29}$$

is an entropy admissible solution to the Riemann problem

$$\begin{cases} u_t + f(u)_x = 0, \\ u(0, x) = u_0(x), \end{cases}$$

with u_0 defined in (1.3.26). The function $u(t, x)$ is called a shock wave.

Remark 19. *If it is considered $\bar{\sigma} > 0$, then (1.3.29) is again a weak solution, but it does not satisfy the entropy condition.*

3. Contact discontinuities. Fix $u^- \in \Omega$, $i \in \{1, \cdots, n\}$ and $\bar{\sigma} \in [-\sigma_0, \sigma_0]$. Define $u^+ = S_i(\bar{\sigma})$. If the i-th characteristic field is linearly degenerate, then the function

$$u(t, x) := \begin{cases} u^-, & \text{if } x < \lambda_i(u^-)t, \\ u^+, & \text{if } x > \lambda_i(u^-)t, \end{cases} \tag{1.3.30}$$

is an entropy admissible solution to the Riemann problem

$$\begin{cases} u_t + f(u)_x = 0, \\ u(0, x) = u_0(x), \end{cases}$$

with u_0 defined in (1.3.26). The function $u(t, x)$ is called a contact discontinuity.

Remark 20. *If the i-th characteristic field is linearly degenerate, then*

$$\lambda_i(u^-) = \lambda_i(u^+) = \lambda_i(\sigma)$$

for every $\sigma \in [-\sigma_0, \sigma_0]$.

Definition 21. *The waves defined in (1.3.28), (1.3.29) and (1.3.30) are called waves of the i-th family.*

For each $\sigma \in \mathbb{R}$ and $i \in \{1, \ldots, n\}$, it is possible to consider the function

$$\psi_i(\sigma)(u_0) := \begin{cases} R_i(\sigma)(u_0), & \text{if } \sigma \geqslant 0, \\ S_i(\sigma)(u_0), & \text{if } \sigma < 0, \end{cases} \qquad (1.3.31)$$

where $u_0 \in \Omega$. The value σ is called the strength of the wave of the i-th family, connecting u_0 to $\psi_i(\sigma)(u_0)$. It follows that $\psi_i(\cdot)(u_0)$ is a smooth function. Moreover it is possible to consider the composite function

$$\Psi(\sigma_1, \ldots, \sigma_n)(u^-) := \psi_n(\sigma_n) \circ \cdots \circ \psi_1(\sigma_1)(u^-), \qquad (1.3.32)$$

where $u^- \in \Omega$ and $(\sigma_1, \ldots, \sigma_n)$ belongs to a neighborhood of 0 in $\mathbb{R}^n$. It is not difficult to calculate the Jacobian matrix of the function Ψ and to prove that it is invertible in a neighborhood of $(0, \ldots, 0)$. Hence it is possible to apply the Implicit Function Theorem and prove the following result.

Theorem 22. *For every compact set $K \subseteq \Omega$, there exists $\delta > 0$ such that, for every $u^- \in K$ and for every $u^+ \in \Omega$ with $|u^+ - u^-| \leqslant \delta$ there exists a unique $(\sigma_1, \ldots, \sigma_n)$ in a neighborhood of $0 \in \mathbb{R}^n$ satisfying*

$$\Psi(\sigma_1, \ldots, \sigma_n)(u^-) = u^+.$$

Moreover the Riemann problem connecting u^- with u^+ has an entropy admissible solution, constructing by piecing together the solutions of n Riemann problems.
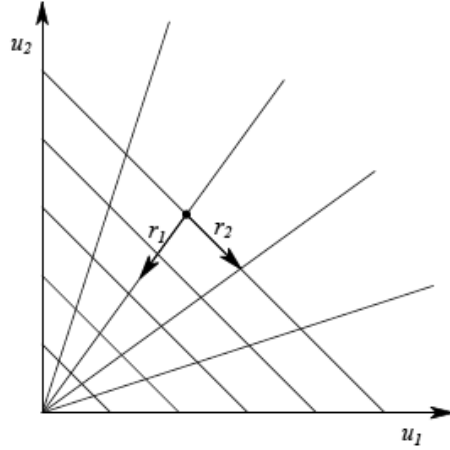
Figure 1.8 Shock and rarefaction curves.

Example 23. *The 2×2 system of conservation laws*

$$[u_1]_t + \left[\frac{u_1}{1 + u_1 + u_2}\right]_x = 0, \ \ [u_2]_t + \left[\frac{u_2}{1 + u_1 + u_2}\right]_x = 0, \ u_1, \ u_2 > 0,$$
$$(1.3.33)$$

is motivated by the study of two - components chromatography. Writing (1.3.33) in the quasi linear form (1.1.3), the eigenvalues and the eigenvectors of the corresponding 2×2 matrix $A(u)$ are found to be

$$\lambda_1(u) = \frac{1}{(1 + u_1 + u_2)^2}, \ \ \lambda_2(u) = \frac{1}{1 + u_1 + u_2},$$

$$r_1(u) = \frac{1}{\sqrt{u_1 + u_2}} \cdot \begin{pmatrix} -u_1 \\ -u_2 \end{pmatrix}, \ \ r_2(u) = \frac{1}{\sqrt{2}} \cdot \begin{pmatrix} 1 \\ -1 \end{pmatrix}.$$

The first characteristic field is genuinely nonlinear, the second is linearly degenerate. In this example, the two shock and rarefaction curves S_i, R_i always coincide, for $i = 1, 2$.

Their computation is easy, because they are straight line (Figure 1.8.):

$$R_1(\sigma)(u) = u + \sigma r_1(u), \ \ \ R_2(\sigma)(u) = u + \sigma r_2(u). \ \ (1.3.34)$$

Observe that the integral curves of the vector field r_1 are precisely the rays through the origin, while the integral curves of r_2 are the lines with slope -1. Now let two states $u^- = \left(u_1^-, u_2^-\right)$, $u^+ = \left(u_1^+, u_2^+\right)$ be given. To solve the Riemann problem (1.3.26) for the system (1.3.25), first it is computed an intermediate state u^* such that $u^* = R_1\left(\sigma_1\right)\left(u^-\right)$, $u^+ = R_2\left(\sigma_2\right)\left(u^*\right)$ for some σ_1, σ_2. By (1.3.34), the components of u^* satisfy

$$u_1^* + u_2^* = u_1^+ + u_2^+, \quad u_1^* u_2^- = u_1^- u_2^*.$$

The solution of the Riemann problem thus takes two different forms, depending on the sign of

$$\sigma_1 = \sqrt{\left(u_1^-\right)^2 + \left(u_2^-\right)^2} - \sqrt{\left(u_1^*\right)^2 + \left(u_2^*\right)^2}.$$

Case 1: $\sigma_1 > 0$. Then, the solution consists of centered rarefaction waves of the first family and of a constant discontinuity of the second family:

$$u\left(t, x\right) = \begin{cases} u^-, & \text{if } x/t < \lambda_1\left(u^-\right), \\ su^* + \left(1-s\right)u^*, & \text{if } x/t = \lambda_1\left(su^* + \left(1-s\right)u^-\right), \\ u^*, & \text{if } \lambda_1\left(u^*\right) < x/t < \lambda_2\left(u^+\right), \\ u^+, & \text{if } x/t \geq \lambda_2\left(u^+\right), \end{cases}$$

(1.3.35)

where $s \in [0, 1]$.
Case 2: $\sigma_1 \leq 0$. Then the solution contains a compressive shock of the first family (which vanishes if $\sigma_1 = 0$) and a contact discontinuity of the second family:

$$u\left(t, x\right) = \begin{cases} u^-, & \text{if } x/t < \lambda_1\left(u^-, u^*\right), \\ u^*, & \text{if } \lambda_1\left(u^-, u^*\right) \leq x/t < \lambda_2\left(u^+\right), \\ u^+, & \text{if } x/t \geq \lambda_2\left(u^+\right). \end{cases}$$

(1.3.36)

Observe that $\lambda_2\left(u^*\right) = \lambda_2\left(u^+\right) = \left(1 + u_1 + u_2\right)^{-1}$, because the second characteristic field is linearly degenerate. In this special case, since the integral curves of r_1 are straight lines, the shock speed in

(1.3.36) can be computed as

$$
\begin{aligned}
\lambda_1\left(u^-, u^*\right) &= \int_0^1 \lambda_1\left(su^* + (1-s)\,u^-\right) ds = \\
&= \int_0^1 \left[1 + s\left(u_1^* + u_2^*\right) + (1-s)\left(u_1^- + u_2^-\right)\right]^{-2} ds = \\
&= \frac{1}{\left(1 + u_1^* + u_2^*\right)\left(1 + u_1^- + u_2^-\right)}.
\end{aligned}
$$

1.3.1 The Non-Convex Scalar Case

It is possible to consider the Riemann Problem (1.3.25)-(1.3.26). Assume f is uniformly convex and $G = (f')^{-1}$.

Theorem 24. *(Solution of Riemann's problem)*

- If $u^- > u^+$, the unique weak solution of the Riemann Problem is

$$
u(t,x) = \begin{cases} u^-, & \frac{x}{t} < \lambda, \\ u^+, & \frac{x}{t} > \lambda, \end{cases} \tag{1.3.37}
$$

where

$$
\lambda = \frac{f(u^+) - f(u^-)}{u^+ - u^-}. \tag{1.3.38}
$$

- If $u^- < u^+$, the unique weak solution of the Riemann Problem is

$$
u(t,x) = \begin{cases} u^-, & \frac{x}{t} < f'(u^-), \\ G(\frac{x}{t}), & f'(u^-) < \frac{x}{t} < f'(u^+), \\ u^+, & \frac{x}{t} > f'(u^+). \end{cases} \tag{1.3.39}
$$

Remark 25. *In the first case the states u^-, u^+ are separated by a shock wave with constant speed λ. In the second case the states u^-, u^+ are separated by a (centered) rarefaction wave.*

Remark 26. *Assume f is uniformly concave. In this case, if $u^- > u^+$ the unique weak solution of the Riemann Problem is a rarefaction wave, while if $u^- < u^+$ the solution is a shock wave.*
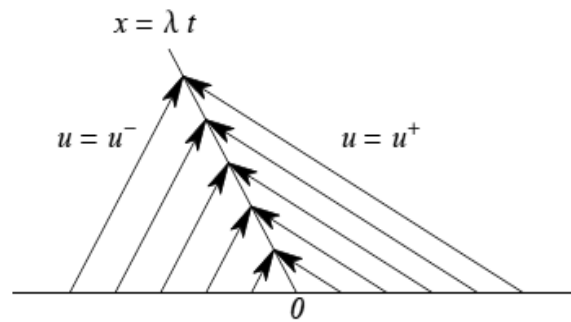
Figure 1.9 Shock wave.
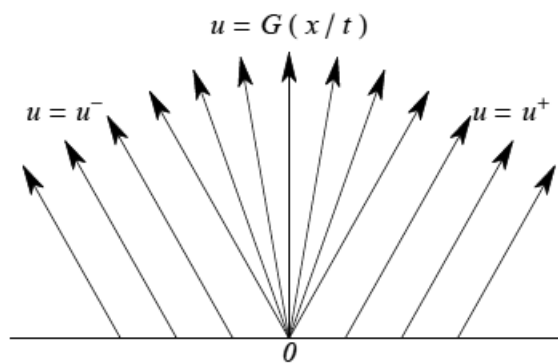
Figure 1.10 Rarefaction waves.
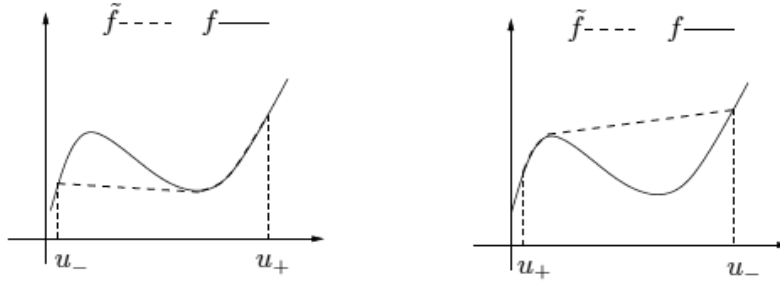
Figure 1.11 Definition of $\tilde{f}$.

In the scalar case, the construction of solutions to Riemann problems can be done not only in the genuinely nonlinear case, i.e. for convex or concave flux or linearly degenerate case, i.e. affine flux. Consider thus a scalar conservation law:

$$u_t + f(u)_x = 0,$$

with $f : \mathbb{R} \to \mathbb{R}$ smooth. Given (u^-, u^+) the solution to the corresponding Riemann problem is done in the following way.
If $u^- < u^+$, $\tilde{f}$ is let to be the largest convex function such that for every $u \in [u^-, u^+]$, it holds:

$$\tilde{f}(u) \leqslant f(u);$$

see Figure 1.11.
If $u^- > u^+$, $\tilde{f}$ is let to be the smallest concave function such that for every $u \in [u^+, u^-]$, it holds:

$$\tilde{f}(u) \geqslant f(u);$$

see Figure 1.11.
Then the solution to the Riemann problem with data (u^-, u^+) is the solution for the flux $\tilde{f}$ to the same Riemann problem.
Notice that, in this case, the flux $\tilde{f}$ is in general not strictly convex or concave but may contain some linear part. The solution to the corresponding Riemann problems may contain combinations
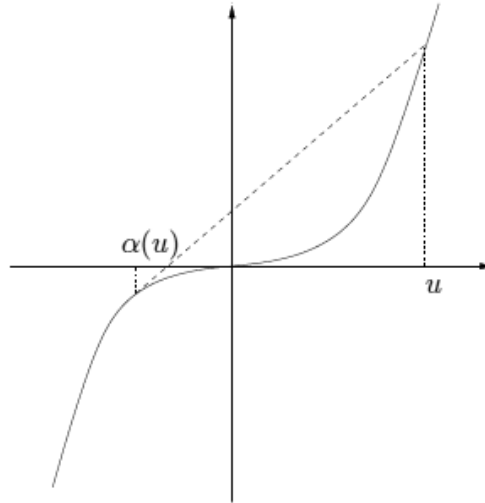
Figure 1.12 Definition of α.

of rarefactions and shocks. For simplicity, only a special case is illustrated.

Fix the scalar conservation law:

$$u_t + (u^3)_x = 0,$$

and $u^- > 0$.

If $u^+ > u^-$, then $\tilde{f}$ coincides with f and the solution to the corresponding Riemann problem is given by a single rarefaction wave. If $u^+ < u^-$, then it is necessary to distinguish two cases. First, for every u define $\alpha(u) \leqslant u$ to be the point such that the secant from $(\alpha(u), f(\alpha(u)))$ to $(u, f(u))$ is tangent to the graph of $f(u) = u^3$ at $\alpha(u)$; see Figure 1.12.

In formulas:

$$\frac{f(u) - f(\alpha(u))}{u - \alpha(u)} = f'(\alpha(u)),$$

then

$$\frac{u^3 - \alpha^3(u)}{u - \alpha(u)} = 3\alpha^2(u),$$
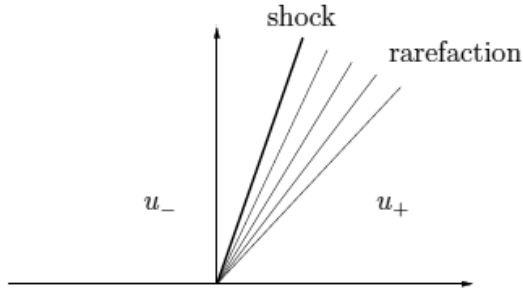
Figure 1.13 Solution to the Riemann problem with $u^- > 0$ and $u^+ < \alpha(u^-)$.

and one can easily get two solutions. The trivial one $\alpha(u) = u$ and

$$\alpha(u) = -\frac{u}{2}.$$

Now if $u^+ \geqslant \alpha(u^-)$ then again $\tilde{f}$ coincides with f and the solution is given by a single shock. If, on the contrary $u^+ < \alpha(u^-)$, the solution to the Riemann problem is given by the function:

$$u(t, x) = \begin{cases} u^-, & \text{if } x < \frac{3}{4}u^- t, \\ -\sqrt{\frac{x}{3t}}, & \text{if } \frac{3}{4}u^- t \leqslant x \leqslant 3(u^+)^2 t, \\ u^+, & \text{if } x > 3(u^+)^2 t, \end{cases}$$

which is formed by a shock followed by a rarefaction attached to it; see Figure 1.13.

In the case $u^- < 0$ the construction is symmetric with respect to the case $u^- > 0$, while for $u^- = 0$ the solution is always given by a rarefaction.

1.4 Functions with Bounded Variation

In this section some basic notions about functions with bounded variation are given.

Consider an interval $J \subseteq \mathbb{R}$ and a function $w : J \to \mathbb{R}$. The total

variation of w is defined by

$$\text{Tot.Var.}\, w = \sup \left\{ \sum_{j=1}^{N} |w(x_j) - w(x_{j-1})| \right\}, \qquad (1.4.40)$$

where $N \geqslant 1$, the points x_j belong to J for every $j \in \{0, \dots, N\}$ and satisfy $x_0 < x_1 < \cdots < x_N$.

Definition 27. *The function $w : J \to \mathbb{R}$ has bounded total variation if $\text{Tot.Var.}\, w < +\infty$. $BV(J)$ denotes the set of all real functions $w : J \to \mathbb{R}$ with bounded total variation.*

Notice that the total variation of a function w is a positive number. If w is a function with bounded total variation, then it is clear that w is a bounded function. The converse is false. In fact every non constant periodic and bounded function on $\mathbb{R}$ has total variation equal to $+\infty$. An important property of functions with bounded total variation is the existence of left and right limits for every x of the interior of J.

Lemma 28. *Let $w : J \to \mathbb{R}$ be a function with bounded total variation and $\bar{x}$ be a point in the interior of J. Then the limits*

$$\lim_{x \to \bar{x}^-} w(x), \qquad \lim_{x \to \bar{x}^+} w(x)$$

exist. Moreover the function w has at most countably many points of discontinuity.

The next theorem shows that subsets of $BV(J)$, with uniform bound in total variation, have some compactness properties.

Theorem 29. *(Helly)* *Consider a sequence of functions $w_n : J \to \mathbb{R}^m$. Assume that there exist positive constant C and M such that:*

1. *$\text{Tot.Var.}\, w_n \leqslant C$ for every $n \in \mathbb{N}$;*

2. *$|w_n(x)| \leqslant M$ for every $n \in \mathbb{N}$ and $x \in J$.*

Then there exist a function $w : J \to \mathbb{R}^m$ and a subsequence w_{n_k} such that

1. *$\lim_{k \to +\infty} w_{n_k}(x) = w(x)$ for every $x \in J$;*

2. *Tot. Var. $w \leqslant C$;*

3. *$|w(x)| \leqslant M$ for every $x \in J$.*

Proof. For every $n \in \mathbb{N}$ and $x \in J$, define the function

$$W_n(x) = \sup \left\{ \sum_{j=1}^{N} |w_n(x_j) - w_n(x_{j-1})| \right\}.$$

where the supremum is taken in $N \geqslant 1$, $x_0 \in J$ and $x_0 < x_1 < \cdots < x_N = x$. The value of the function W_n at a certain point $x \in J$ is the total variation of the function w_n until the point x. Moreover there is

$$0 \leqslant W_n(x) \leqslant C, \tag{1.4.41}$$

for every $n \in \mathbb{N}$ and $x \in J$ and

$$|w_n(y) - w_n(x)| \leqslant W_n(y_2) - W_n(y_1), \tag{1.4.42}$$

for every $n \in \mathbb{N}$, $x, y, y_1, y_2 \in J$ and $y_1 \leqslant x \leqslant y \leqslant y_2$. By (1.4.41) and a diagonal procedure, there exist a subsequence W_{n_h} of W_n and a function W such that

$$\lim_{h \to +\infty} W_{n_h}(x) = W(x)$$

for every $x \in J \cap \mathbb{Q}$. Define, for every $n \in \mathbb{N}$,

$$B_n = \left\{ x \in \text{Int } J : \lim_{y \to x^+} W(x) - \lim_{y \to x^-} W(x) \geqslant \frac{1}{n} \right\}.$$

The set B_n is finite and it can contain at most Cn points; hence the set

$$B = \bigcup_{n \in \mathbb{N}} B_n$$

is at most countable. It implies that the function W has at most a countable number of discontinuities.

By hypotheses it is also possible to choose a subsequence n_{h_k} of n_h, which, for simplicity, is called n_k, such that

$$\lim_{k \to +\infty} w_k(x) = w(x)$$

for every $x \in J \cap (\mathbb{Q} \cup B)$. Indeed there is that the previous limit exists for every $x \in J$. Assume that $\bar{x} \in J \setminus B$. This implies that $\bar{x} \notin B_n$ for every $n \in \mathbb{N}$ and so, for every $n \in \mathbb{N}$, there exist $y_1 < \bar{x} < y_2$, $y_1, y_2 \in \mathbb{Q}$ such that $W(y_2) - W(y_1) < \frac{1}{n}$. There is

$$
\begin{aligned}
\limsup_{k, \tilde{k} \to +\infty} |w_k(\bar{x}) - w_{\tilde{k}}(\bar{x})| &\leqslant 2 \limsup_{k \to +\infty} |w_k(\bar{x}) - w_k(y_1)| \\
&\leqslant 2 \left(W(y_2) - W(y_1) \right) < \frac{2}{n}.
\end{aligned}
$$

Finally consider points $x_0 < x_1 < \cdots < x_N$ in the set J. It is possible to deduce that

$$\sum_{j=1}^{N} |w(x_j) - w(x_{j-1})| = \lim_{k \to +\infty} \left(\sum_{j=1}^{N} |w_{n_k}(x_j) - w_{n_k}(x_{j-1})| \right) \leqslant C,$$

and this concludes the proof. $\qquad \square$

Theorem 30. *Consider a sequence of functions $w_n : [0, +\infty[\times J \to \mathbb{R}^n$. Assume that there exist positive constants C, L and M such that:*

1. *Tot.Var. $w_n(t, \cdot) \leqslant C$ for every $n \in \mathbb{N}$ and $t \geqslant 0$;*

2. *$|w_n(t, x)| \leqslant M$ for every $n \in \mathbb{N}$, $x \in J$ and $t \geqslant 0$;*

3. *$\int_J |w_n(t, x) - w_n(s, x)| \, dx \leqslant L \, |t - s|$ for every $n \in \mathbb{N}$ and $t, s \geqslant 0$.*

Then there exist a function $w \in L^1_{loc}([0, +\infty \times J; \mathbb{R}^n)$ and a subsequence w_{n_k} such that

1. *$w_{n_k} \to w$ in $L^1_{loc}([0, +\infty \times J; \mathbb{R}^n)$ as $k \to +\infty$;*

2. $\int_J |w(t,x) - w(s,x)|\, dx \leqslant L\, |t - s|$ *for every* $t, s \geqslant 0$.

Moreover the values of w can be uniquely determined by setting

$$w(t,x) = \lim_{y \to x^+} w(t,y)$$

for every $t \geqslant 0$ and $x \in \operatorname{Int} J$. In this case there is

1. *Tot.Var.* $w(t,\cdot) \leqslant C$ *for every* $t \geqslant 0$;

2. $|w(t,x)| \leqslant M$ *for every* $t \geqslant 0$ *and* $x \in J$.

Proof. By Helly's theorem, it is possible to find a subsequence w_{n_k} such that, for every $t \geqslant 0$, $t \in \mathbb{Q}$, $w_{n_k}(t,\cdot) \to w(t,\cdot)$ pointwise and hence in $L^1_{loc}(\mathbb{R}; \mathbb{R}^n)$. Thus there is

$$\int_J |w(t,x) - w(s,x)|\, dx \leqslant L\, |t - s|, \quad \text{Tot.Var.}\, w(t,\cdot) \leqslant C,$$

and

$$|w(t,x)| \leqslant M$$

for every $t, s \in \mathbb{Q} \cap [0, +\infty[$, $x \in J$. Fix now $t \geqslant 0$ and consider a sequence $t_m \to t$. Define

$$u(t,\cdot) = \lim_{m \to +\infty} w(t_m, \cdot).$$

By the previous estimates, this limit exists and is independent from the sequence t_m. It is possible to deduce

$$\int_J |u(t,x) - u(s,x)|\, dx \leqslant L\, |t - s|, \quad \text{Tot.Var.}\, u(t,\cdot) \leqslant C,$$

and

$$|u(t,x)| \leqslant M$$

for every $t, s \in [0, +\infty[$, $x \in J$, eventually by modifying the function u on a set of measure zero.
Consider now, for $\varepsilon > 0$ sufficiently small,

$$w_\varepsilon(t,x) = \frac{1}{\varepsilon} \int_x^{x+\varepsilon} u(t,s)\, ds$$

and

$$\tilde{w}(t, x) = \lim_{\varepsilon \to 0^+} w^{\varepsilon}(t, x).$$

This function satisfies

$$w(t, x) = \lim_{y \to x^+} w(t, y).$$

This concludes the proof. □

1.4.1 BV Functions in $\mathbb{R}^n$

In this section the L^1 theory for BV functions (see [11]) is briefly described. Let Ω be an open subset of $\mathbb{R}^n$ and consider $w : \Omega \to \mathbb{R}$. $\mathcal{B}(\Omega)$ denotes the σ-algebra of Borel sets of Ω and with $\mathcal{B}_c(\Omega)$ the set

$$\{B \in \mathcal{B}(\Omega) : B \text{ compactly embedded in } \Omega\}. \qquad (1.4.43)$$

Definition 31. *$\mu : \mathcal{B}_c(\Omega) \to \mathbb{R}$ is a Radon measure if it is count-able additive and $\mu(\emptyset) = 0$. $\mathfrak{M}(\Omega)$ denotes the set of all Radon measures on Ω.*

The following theorem holds.

Theorem 32. *Fix a Radon measure $\mu \in \mathfrak{M}(\Omega)$. There exist two positive and unique Borel measures $\mu^+, \mu^- : \mathcal{B}(\Omega) \to [0, +\infty]$ such that*

$$\mu(E) = \mu^+(E) - \mu^-(E) \qquad (1.4.44)$$

for every $E \in \mathcal{B}_c(\Omega)$.

It is now possible to give the definitions of bounded Radon measures and of bounded total variation functions.

Definition 33. *Fix a Radon measure $\mu \in \mathfrak{M}(\Omega)$ and consider the total variation of μ defined by $|\mu| := \mu^+ + \mu^-$. μ has bounded total variation if $|\mu|(\Omega) < +\infty$ and $\mathfrak{M}_b(\Omega)$ denotes the set of all Radon measures with bounded total variation.*

Remark 34. *Notice that $\mathfrak{M}_b(\Omega)$ is a Banach space with respect to the norm*

$$\|\mu\|_{\mathfrak{M}_b(\Omega)} = |\mu|(\Omega).$$

Definition 35. *$w : \Omega \to \mathbb{R}$ has bounded total variation if*

1. *$w \in L^1(\Omega)$;*

2. *the i-th partial derivative $D_i w$ exists in the sense of distributions and belongs to $\mathfrak{M}_b(\Omega)$, for every $i = 1, \ldots, n$.*

The total variation of w is given by

$$\sum_{i=1}^{n} |D_i w|(\Omega).$$

$BV(\Omega)$ denotes the set of all functions defined on Ω with bounded total variation.

Remark 36. *The space $BV(\Omega)$ is a Banach space with respect to the norm*

$$\|w\|_{L^1(\Omega)} + \sum_{i=1}^{n} |D_i w|(\Omega).$$

Remark 37. *Let $w \in L^1(\Omega)$. Then $w \in BV(\Omega)$ if and only if there exists $c \in (0, +\infty)$ such that*

$$\left| \int_\Omega w \operatorname{div} \varphi \, dx \right| \leqslant c \sup_{x \in \Omega} |\varphi(x)|$$

for every $\varphi \in C_c^\infty(\Omega; \mathbb{R}^n)$. In this case one can choose the constant c equal to the total variation of w.

Remark 38. *If Ω is an interval of $\mathbb{R}$, then the two descriptions of BV functions are not completely equivalent. The most important difference is that if the values of a BV function w is changed in a finite set, then the total variation of w changes but remain finite if the first description is considered, while it does not vary in the second case. Therefore, if we are interested only in the L^1 equivalence class, then it is possible to assume that a BV function w is right continuous or left continuous.*

1.5 Wave-Front Tracking and Existence of Solutions

This section deals with the existence of an entropy admissible solution to the Cauchy problem

$$\begin{cases} u_t + [f(u)]_x = 0, \\ u(0, \cdot) = \bar{u}(\cdot), \end{cases} \tag{1.5.45}$$

where $f : \mathbb{R}^n \to \mathbb{R}^n$ is a smooth flux and $\bar{u} \in L^1(\mathbb{R}^n)$ is bounded in total variation. In order to prove existence, a sequence of approximate solutions using the method called wave-front tracking algorithm is created.

Firstly the scalar case is considered, while the system case, much more delicate, will be only sketched.

1.5.1 The Scalar Case

The following conditions are assumed:

(C1) $f : \mathbb{R} \to \mathbb{R}$ is a scalar smooth function;

(C2) the characteristic field is either genuinely nonlinear or linearly degenerate.

The construction starts at time $t = 0$ by choosing a sequence of piecewise constant approximations $(\bar{u}_\nu)_\nu$ of $\bar{u}$ such that

$$\text{Tot.Var.}\{\bar{u}_\nu\} \leqslant \text{Tot.Var.}\{\bar{u}\}, \tag{1.5.46}$$

$$\|\bar{u}_\nu\|_{L^\infty} \leqslant \|\bar{u}\|_{L^\infty} \tag{1.5.47}$$

and

$$\|\bar{u}_\nu - \bar{u}\|_{L^1} < \frac{1}{\nu}, \tag{1.5.48}$$

for every $\nu \in \mathbb{N}$; see Figure 1.14.

Fix $\nu \in \mathbb{N}$. By (1.5.46), $\bar{u}_\nu$ has a finite number of discontinuities, say $x_1 < \cdots < x_N$. For each $i = 1, \ldots, N$, the Riemann problem generated by the jump $(\bar{u}_\nu(x_i-), \bar{u}_\nu(x_i+))$ with piecewise
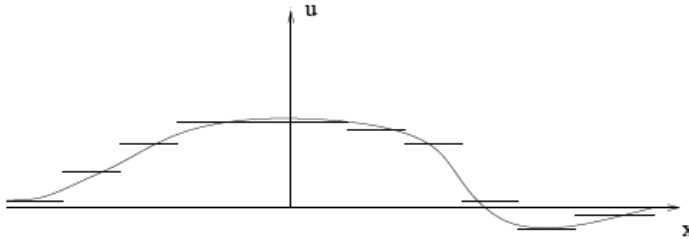
Figure 1.14 A piecewise constant approximation of the initial datum satisfying (1.5.47) and (1.5.48).
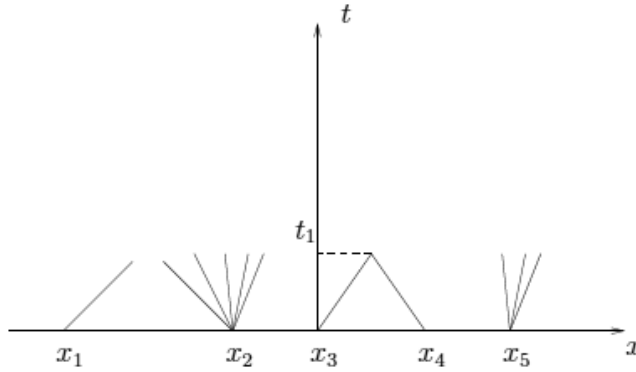
Figure 1.15 The wave front tracking construction until the first time of interaction.

constant functions of the type $\varphi(\frac{x-x_i}{t})$ are approximately solved, where $\varphi : \mathbb{R} \to \mathbb{R}$. More precisely, if the Riemann problem generated by $(\bar{u}_\nu(x_i-), \bar{u}_\nu(x_i+))$ admits an exact solution containing just shocks or contact discontinuities, then $\varphi(\frac{x-x_i}{t})$ is the exact solution, while if a rarefaction wave appears, then it is split in a centered rarefaction fan, containing a sequence of jumps of size at most $\frac{1}{\nu}$, travelling with a speed between the characteristic speeds of the states connected. In this way, it is possible able to construct an approximate solution $u_\nu(t, x)$ until a time t_1, where at least two wave fronts interact together; see Figure 1.15.

Remark 39. *In the scalar case, if the characteristic field is lin-*

early degenerate, then all the waves are contact discontinuities and travel at the same speed. Therefore the previous construction can be done for every positive time.

Remark 40. *Notice that it is possible to avoid that three of more wave fronts interact together at the same time slightly changing the speed of some wave fronts. This may introduce a small error of the approximate solution with respect to the exact one.*

At time $t = t_1$, $u_\nu(t_1, \cdot)$ is clearly a piecewise constant function. So it is possible repeat the previous construction until a second interaction time $t = t_2$ and so on. In order to prove that a wave-front tracking approximate solution exists for every $t \in [0, T]$, where T may be also $+\infty$, it is necessary to estimate

1. the number of waves;

2. the number of interactions between waves;

3. the total variation of the approximate solution.

The first two estimates are concerned with the possibility to construct a piecewise constant approximate solution. The third estimate, instead, is concerned with the convergence of the approximate solutions towards an exact solution.

Remark 41. *The two first bounds are nontrivial for the vector case and it is necessary to introduce simplified solutions to Riemann problems and/or non-physical waves.*

The next lemma shows that the number of interactions is finite.

Lemma 42. *The number of wave fronts for the approximate solution u_ν is not increasing with respect to the time and so u_ν is defined for every $t \geqslant 0$. Moreover the number of interactions between waves is bounded by the number of wave fronts.*

Proof. Consider two wave fronts interacting together. The wave fronts can be:
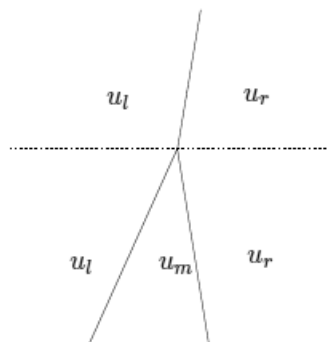
Figure 1.16 Interaction between two wave fronts.

1. two shocks,

2. two rarefaction shocks,

3. a shock and a rarefaction shock,

4. two contact discontinuities.

By Remark 39, the case of two contact discontinuities can not happen. Moreover, the speeds of waves imply that also the case of two rarefaction shocks can not happen. In fact, suppose that two rarefaction shocks interact together at a certain time. Denote with u_l, u_m and u_r respectively the states as in Figure 1.16. Since these waves are rarefactions shocks, there is

$$\lambda(u_l) < \lambda(u_m) < \lambda(u_r),$$

where λ denotes the characteristic speeds of the states. Therefore the wave connecting u_l to u_m has a speed less than or equal to the speed of the wave connecting u_m to u_r and the wave fronts can not interact together.
So the remaining possibilities are the followings.

1. Two shocks. In this case it is clear that after the interaction, a single shock wave is created. So the number of waves decreases by 1.

2. A shock and a rarefaction shock. In this case either a single shock wave is produced as in the previous possibility, or a single rarefaction shock is created. In fact, if the exact solution to the Riemann problem at the interaction time is given by a rarefaction wave, then the size of the rarefaction wave is less than or equal to the size of the rarefaction shock, which is less than or equal to $1/\nu$. This implies that the wave is split in a single rarefaction shock. Thus the number of waves decreases by 1.

Therefore it is possible to conclude that at each interaction the number of wave fronts decreases at least by 1 and so the lemma is proved. □

Lemma 43. *The total variation of $u_\nu(t, \cdot)$ is not increasing with respect the time. Therefore for each $t \geqslant 0$*

$$Tot.Var. u_\nu(t, \cdot) \leqslant Tot.Var. \bar{u}. \qquad (1.5.49)$$

Proof. It is clear that the total variation may vary only at interaction times.

Consider an interaction of two wave fronts at time $\bar{t}$. It is possible to call by u_l, u_m and u_r respectively the left, the middle and the right state of the wave fronts; see Figure 1.16.

The interaction between the two waves produces a single wave connecting u_l with u_r. The variation before $t = \bar{t}$ due to the interacting waves is given by $|u_l - u_m| + |u_m - u_r|$, while the variation after $t = \bar{t}$ due to the wave produced is given by $|u_l - u_r|$. Triangular inequality implies that

$$|u_l - u_r| \leqslant |u_l - u_m| + |u_m - u_r|$$

and so the proof is finished. □

The following theorem holds.

Theorem 44. *Let $f : \mathbb{R} \to \mathbb{R}$ be smooth and $\bar{u} \in L^1(\mathbb{R})$ with bounded variation. Then there exists an entropy-admissible solution $u(t, x)$ to the Cauchy problem (1.5.45), defined for every $t \geqslant 0$. Moreover*

$$\|u(t, \cdot)\|_{L^\infty} \leqslant \|\bar{u}(\cdot)\|_{L^\infty} \qquad (1.5.50)$$

for every $t \geqslant 0$.

Proof. For every $\nu \in \mathbb{N}$, construct a wave-front tracking approximate solution u_ν as before in this section.
Clearly there is

$$|u_\nu(t, x)| \leqslant |u_\nu(0, x)| \leqslant \|\bar{u}\|_{L^\infty} \tag{1.5.51}$$

for every $\nu \in \mathbb{N}$, $t \geqslant 0$ and $x \in \mathbb{R}$. By Lemma 43,

$$\text{Tot.Var.} \, u_\nu(t, \cdot) \leqslant \text{Tot.Var.} \, \bar{u}, \tag{1.5.52}$$

for every $t \geqslant 0$ and $\nu \in \mathbb{N}$. Finally the maps $t \mapsto u_\nu(t, \cdot)$ are uniformly Lipschitz continuous with values in $L^1(\mathbb{R}; \mathbb{R})$. Therefore, by Theorem 30, it is possible to extract a subsequence, denoted again by $u_\nu(t, x)$, converging to some function $u(t, x)$ in $L^1([0, +\infty[\times \mathbb{R}; \mathbb{R})$. Since $\|u_\nu(0, \cdot) - \bar{u}(\cdot)\|_{L^1} \to 0$, then the initial condition clearly holds.
It remains to prove that $u(t, x)$ is a weak solution to the Cauchy problem (1.5.45) and that it is entropy admissible. To prove the first claim, fix $T > 0$ and an arbitrary C^1 function ψ with compact support in $] - \infty, T[\times \mathbb{R}$. It is necessary to prove that

$$\int_0^T \int_{\mathbb{R}} \{u \cdot \psi_t + f(u) \cdot \psi_x\} dx dt + \int_{\mathbb{R}} \bar{u}(x) \cdot \psi(0, x) dx = 0.$$

It is sufficient to prove that

$$\lim_{\nu \to +\infty} \left\{ \begin{array}{l} \int_0^T \int_{\mathbb{R}} \{u_\nu \cdot \psi_t + f(u_\nu) \cdot \psi_x\} dx dt + \\ \int_{\mathbb{R}} u_\nu(0, x) \cdot \psi(0, x) dx \end{array} \right\} = 0. \tag{1.5.53}$$

Fix $\nu \in \mathbb{N}$. At every $t \in [0, T]$, call $x_1(t) < \cdots < x_N(t)$ the points where $u_\nu(t, \cdot)$ has a jump and set

$$\Delta u_\nu(t, x_\alpha) := u_\nu(t, x_\alpha+) - u_\nu(t, x_\alpha-),$$
$$\Delta f(u_\nu(t, x_\alpha)) := f(u_\nu(t, x_\alpha+)) - f(u_\nu(t, x_\alpha-)).$$

The lines $x_\alpha(t)$ divide $[0, T] \times \mathbb{R}$ into a finite number of regions, say Γ_j, where u_ν is constant. Applying the divergence theorem to

$(\psi \cdot u_\nu, \psi \cdot f(u_\nu))$ and splitting the integral (1.5.53) over the regions Γ_j, the integral (1.5.53) can be rewritten in the form

$$\int_0^T \sum_\alpha \left[\dot{x}_\alpha(t) \cdot \Delta u_\nu(t, x_\alpha) - \Delta f(u_\nu(t, x_\alpha)) \right] \psi(t, x_\alpha(t)) dt.$$

$$(1.5.54)$$

If x_α is a shock wave or a contact discontinuity, then

$$\dot{x}_\alpha(t) \cdot \Delta u_\nu(t, x_\alpha) - \Delta f(u_\nu(t, x_\alpha)) = 0,$$

while if x_α is a rarefaction wave, then

$$\dot{x}_\alpha(t) \cdot \Delta u_\nu(t, x_\alpha) - \Delta f(u_\nu(t, x_\alpha)),$$

depends linearly on the L^∞ distance between u_ν and $\bar{u}$. Splitting the summation in (1.5.54) over waves of the same type, it is possible to deduce that the previous integral tends to 0 as $\nu \to +\infty$, concluding that $u(t, x)$ is a weak solution to the Cauchy problem. Fix now η a convex entropy with a corresponding entropy flux q. It remains to prove that

$$\liminf_{\nu \to +\infty} \int_0^T \int_\mathbb{R} \left[\eta(u_\nu)\psi_t + q(u_\nu)\psi_x \right] dx dt \geqslant 0$$

for every C^1 positive function φ with compact support. Using again the divergence theorem as before, it is necessary to prove that

$$\liminf_{\nu \to +\infty} \int_0^T \sum_\alpha \left[\dot{x}_\alpha(t) \cdot \Delta \eta(u_\nu(t, x_\alpha)) - \Delta q(u_\nu(t, x_\alpha)) \right] \varphi(t, x_\alpha) dt \geqslant 0$$

where

$$\Delta \eta(u_\nu(t, x_\alpha)) := \eta(u_\nu(t, x_\alpha+)) - \eta(u_\nu(t, x_\alpha-)),$$
$$\Delta q(u_\nu(t, x_\alpha)) := q(u_\nu(t, x_\alpha+)) - q(u_\nu(t, x_\alpha-)).$$

Using the same estimates as in the previous case, it is possible to conclude. $\qquad\square$

1.5.2   The System Case

For systems, the construction of wave-front tracking approxima-
tions is more complex, because more types of interactions may
happen. In particular the bounds on number of waves, interac-
tions and BV norms are no more directly obtained.

It is possible to start giving some total variation estimates for
interaction of waves along a wave-front tracking approximation.
These permit to illustrate the ideas for obtaining the needed bounds
in system case. The constants in the estimates depend on the to-
tal variation of the initial data, which is assumed to be sufficiently
small.

Consider a wave of the i–th family of strength σ_i interacting with
a wave of the j–th family of strength σ_j, $i \neq j$, and indicate by σ'_k
($k \in \{1, \ldots, n\}$) the strengths of the new waves produced by the
interaction. Then it holds

$$|\sigma_i - \sigma'_i| + |\sigma_j - \sigma'_j| + \sum_{k \neq i,j} |\sigma'_k| \leq C|\sigma_i||\sigma_j|, \qquad (1.5.55)$$

For the case $i = j$, it is possible to indicate by $\sigma_{i,1}$ and $\sigma_{i,2}$ the
strengths of the interacting waves, then it holds

$$|\sigma_{i,1} + \sigma_{i,2} - \sigma'_i| + \sum_{k \neq i} |\sigma'_k| \leq C|\sigma_{i,1}||\sigma_{i,2}|. \qquad (1.5.56)$$

One can now fix a parameter δ_ν and split rarefactions in rarefac-
tion fans with shocks of strength at most δ_ν. Also, at each interac-
tion time, one solves exactly the new Riemann problem, eventually
splitting the rarefaction waves in rarefaction fans, only if the prod-
uct of interacting waves is bigger than δ_ν. Otherwise, one solves
the Riemann problem only with waves of the same families of the
interacting ones, the error being transported along a *non-physical
wave*, travelling at a speed bigger than all waves. In this way, it is
possible to control the number of waves and interactions and then
let δ_ν go to zero (for details see [3]).

Consider now a wave-front tracking approximate solution u_ν and
let $x_\alpha(t)$, of family i_α and strength σ_α, indicate the discontinuities

of $u_\nu(t)$. Two discontinuities are interacting if $x_\alpha < x_\beta$ and either $i_\alpha > i_\beta$ or $i_\alpha = i_\beta$ and at least one of the two waves is a shock. The Glimm functional computed at $u_\nu(t)$ is defined as:

$$Y(u_\nu(t)) = TV(u_\nu(t)) + C_1 \, Q(u_\nu(t)),$$

where C_1 is a constant to be chosen suitably and

$$Q(u_\nu(t)) = \sum |\sigma_\alpha||\sigma_\beta|$$

where the sum is over interacting waves. One can easily prove that the functional Y is equivalent to the functional measuring the total variation. Clearly such functional changes only at interaction times. Using the interaction estimates (1.5.55) and (1.5.56), at an interaction time $\bar{t}$,

$$|TV(u_\nu(\bar{t}+)) - TV(u_\nu(\bar{t}-))| \leqslant C|\sigma_i||\sigma_j|,$$

$$Q(u_\nu(\bar{t}+)) - Q(u_\nu(\bar{t}-)) \leqslant -C_1|\sigma_i||\sigma_j| + C|\sigma_i||\sigma_j| \, TV(u_\nu(\bar{t}-)),$$

is get. Therefore

$$Y(u_\nu(\bar{t}+)) - Y(u_\nu(\bar{t}-)) \leqslant |\sigma_i||\sigma_j|\big[C - C_1 + C \, TV(u_\nu(\bar{t}-))\big].$$

On the other side, for every t:

$$TV(u_\nu(t)) \leq Y(u_\nu(t)).$$

Then choosing $C_1 > C$ and assuming that $TV(u_\nu(0))$ is sufficiently small, one has that Y is decreasing along a wave-front tracking approximate solution and so the total variation is controlled.

1.6 Uniqueness and Continuous Dependence

The aim of this section is to illustrate a method to prove uniqueness and Lipschitz continuous dependence by initial data for solutions to the Cauchy problem, controlling for any two approximate

solutions u, u' how their distance varies in time. For simplicity the scalar case is considered. The method is based on a Riemannian type distance on L^1. In [4], the approach was applied to systems case. Various alternative methods were recently introduced to treat uniqueness, but the one presented here is the more suitable to be used for networks.

The basic idea is to estimate the L^1-distance viewing L^1 as a Riemannian manifold. It is considered the subspace of piecewise constant functions and "generalized tangent vectors" consisting of two components (v, ξ), where $v \in L^1$ describes the L^1 infinitesimal displacement, while $\xi \in \mathbb{R}^n$ describes the infinitesimal displacement of discontinuities. For example, take a family of piecewise constant functions $\theta \to u^\theta$, $\theta \in [0,1]$, each of which has the same number of jumps, say at the points $x_1^\theta < ... < x_N^\theta$. Assume that the following functions are well defined (see Figure 1.17)

$$L^1 \ni v^\theta(x) \doteq \lim_{h \to 0} \frac{u^{\theta+h}(x) - u^\theta(x)}{h},$$

and also the numbers

$$\xi_\beta^\theta \doteq \lim_{h \to 0} \frac{x_\beta^{\theta+h} - x_\beta^\theta}{h}, \qquad \beta = 1, ..., N.$$

Then it is said that γ admits tangent vectors

$$(v^\theta, \xi^\theta) \in T_{u^\theta} \doteq^1(\mathbb{R}; \mathbb{R}^n) \times \mathbb{R}^n.$$

In general such path $\theta \to u^\theta$ is not differentiable w.r.t. the usual differential structure of L^1, in fact if $\xi_\beta^\theta \neq 0$, as $h \to 0$ the ratio $\left[u^{\theta+h}(x) - u^\theta(x)\right]/h$ does not converge to any limit in L^1.

One can compute the L^1-length of the path $\gamma : \theta \to u^\theta$ in the following way:

$$\|\gamma\|_{L^1} = \int_0^1 \left\|v^\theta\right\|_{L^1} d\theta + \sum_{\beta=1}^N \int_0^1 \left|u^\theta(x_\beta+) - u^\theta(x_\beta-)\right| \left|\xi_\beta^\theta\right| d\theta.$$

$$(1.6.57)$$
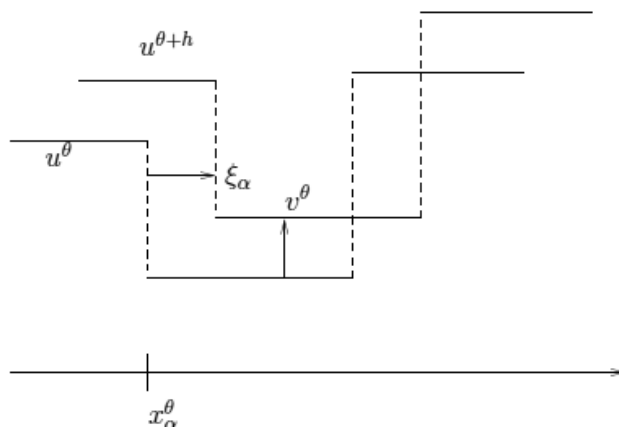
Figure 1.17 Construction of "generalized tangent vectors".

According to (1.6.57), in order to compute the L^1-length of a path γ, the norm of its tangent vector is integrated, which is defined as follows:

$$\|(v,\xi)\| \doteq \|v\|_{L^1} + \sum_{\beta=1}^{N} |\Delta u_\beta|\, |\xi_\beta|\,,$$

where $\Delta u_\beta = u(x_\beta+) - u(x_\beta-)$ is the jump across the discontinuity x_β.

It is possible to introduce the following definition.

Definition 45. *A continuous map $\gamma : \theta \to u^\theta \doteq \gamma(\theta)$ from $[0,1]$ into L^1_{loc} is a regular path if the following holds. All functions u^θ are piecewise constant, with the same number of jumps, say at $x_1^\theta < ... < x_N^\theta$ and coincide outside some fixed interval $]-M, M[$. Moreover, γ admits a generalized tangent vector $D\gamma(\theta) = (v^\theta, \xi^\theta) \in T_{\gamma(\theta)} = L^1(\mathbb{R};\mathbb{R}^n) \times \mathbb{R}^N$, continuously depending on θ .*

Given two piecewise constant functions u and u', call $\Omega(u, u')$ the family of all regular paths $\gamma : [0,1] \to \gamma(t)$ with $\gamma(0) = u$, $\gamma(1) = u'$. The Riemannian distance between u and u' is given by

$$d(u, u') \doteq \inf\left\{\|\gamma\|_{L^1}, \gamma \in \Omega(u, u')\right\}.$$

To define d on all L^1, for given $u, u' \in L^1$,

$$d(u, u') \doteq \inf \left\{ \|\gamma\|_{L^1} + \|u - \tilde{u}\|_{L^1} + \|u' - \tilde{u}'\|_{L^1} : \right.$$
$$\left. \tilde{u}, \tilde{u}' \text{ piecewise constant functions, } \gamma \in \Omega(u, u') \right\},$$

is set. It is easy to check that this distance coincides with the distance of L^1. (For the systems case, one has to introduce weights, see [4], obtaining an equivalent distance.)

Now it is possible to estimate the L^1 distance among solutions, studying the evolution of norms of tangent vectors along wave-front tracking approximations. Take u, u' piecewise constant functions and let $\gamma_0(\vartheta) = u^\vartheta$ be a regular path joining $u = u^0$ with $u' = u^1$. Define $u^\vartheta(t, x)$ to be a wave-front tracking approximate solution with initial data u^ϑ and let $\gamma_t(\vartheta) = u^\vartheta(t, \cdot)$.

One can easily check that, for every γ_0 (regular path) and every $t \geq 0$, γ_t is a regular path. If it is possible prove

$$\|\gamma_t\|_{L^1} \leq \|\gamma_0\|_{L^1}, \tag{1.6.58}$$

then for every $t \geq 0$

$$\|u(t, \cdot) - u'(t, \cdot)\|_{L^1} \leq \inf_{\gamma_t} \|\gamma_t\|_{L^1} \leq \tag{1.6.59}$$
$$\inf_{\gamma_0} \|\gamma_0\|_{L^1} = \|u(0, \cdot) - u'(0, \cdot)\|_{L^1}.$$

To obtain (1.6.58), hence (1.6.59), it is enough to prove that, for every tangent vector $(v, \xi)(t)$ to any regular path γ_t, one has:

$$\|(v, \xi)(t)\| \leq \|(v, \xi)(0)\|, \tag{1.6.60}$$

i.e the norm of a tangent vector does not increase in time. Moreover, if (1.6.59) is established, then uniqueness and Lipschitz continuous dependence of solutions to Cauchy problems is straightforwardly achieved passing to the limit on the wave-front tracking approximate solutions.

It is possible now to estimate the increase of the norm of a tangent vector. In order to achieve (1.6.60), a time $\bar{t}$ is fixed and the following cases are treated:

Case 1. no interaction of waves takes place at $\bar{t}$;

Case 2. two waves interact at $\bar{t}$;

In Case 1, denote by x_β, σ_β, and ξ_β, respectively, the positions, sizes and shifts of the discontinuities of a wave-front tracking approximate solution. Following [4]:

$$\frac{d}{dt} \left\{ \int |v(t,x)| \, dx + \sum_\beta |\xi_\beta| \, |\sigma_\beta| \right\} =$$

$$- \left\{ \sum_\beta \left(\lambda(\rho^-) - \dot{x}_\beta \right) |v^-| + \sum_\beta \left(\dot{x}_\beta - \lambda(\rho^+) \right) |v^+| \right\} +$$

$$+ \sum_\beta D\lambda(\rho^-, \rho^+) \cdot (v^-, v^+) \, (\text{sign}\xi_\beta) \, |\sigma_\beta| \, ,$$

is get, with $\sigma_\beta = \rho^+ - \rho^-$, $\rho^\pm \doteq \rho(x_\beta \pm)$ and similarly for $v^\pm$. If the waves respect the Rankine-Hugoniot conditions, then

$$D\lambda(\rho^-, \rho^+)(v^-, v^+) = \left(\lambda(\rho^-) - \dot{x}_\beta \right) \frac{v^-}{|\sigma_\beta|} + \left(\dot{x}_\beta - \lambda(\rho^+) \right) \frac{v^+}{|\sigma_\beta|}$$

and

$$\frac{d}{dt} \left\{ \int |v(t,x)| \, dx + \sum_\beta |\xi_\beta| \, |\sigma_\beta| \right\} \leq 0. \qquad (1.6.61)$$

In the wave front tracking algorithm the Rankine-Hugoniot condition may be violated for rarefaction fans. However, this results in an increase of the distance which is controlled in terms of $1/\nu$ (the size of a rarefaction shock) and tends to zero with $\nu \to \infty$. It is possible now to pass to Case 2. First, there is the following:

Lemma 46. *Consider two waves, with speeds λ_1 and λ_2 respectively, that interact together at $\bar{t}$ producing a wave with speed λ_3. If the first wave is shifted by ξ_1 and the second wave by ξ_2, then the shift of the resulting wave is given by*

$$\xi_3 = \frac{\lambda_3 - \lambda_2}{\lambda_1 - \lambda_2} \xi_1 + \frac{\lambda_1 - \lambda_3}{\lambda_1 - \lambda_2} \xi_2. \qquad (1.6.62)$$

Moreover there is that

$$\Delta\rho_3\,\xi_3 = \Delta\rho_1\,\xi_1 + \Delta\rho_2\,\xi_2, \qquad (1.6.63)$$

where $\Delta\rho_i$ are the signed strengths of the corresponding waves.

From (1.6.63) it follows

$$|\Delta\rho_3\xi_3| \le |\Delta\rho_1|\,|\xi_1| + |\Delta\rho_2|\,|\xi_2|\,,$$

from which

$$\|(v,\xi)(\bar{t}+)\| \le \|(v,\xi)(\bar{t}-)\|\,. \qquad (1.6.64)$$

Chapter 2

Cardiovascular system: description and mathematical models

2.1 Description

The cardiovascular or circulatory system transports oxygen and nutrients to all the tissues of the body, from where it removes carbon dioxide and other harmful waste products of cell metabolism. From a physical point of view, the system consists of two synchronized pumps in parallel that propel a viscous liquid (the blood) through a network of flexible tubes. The heart provides energy to move blood through the circulatory system. It consists of four cavities: two ventricles and two atria (see Figure 2.1), whose size varies during the cardiac cycle due to the activity of the heart muscle. The right heart pumps deoxygenated blood through the *pulmonary circulation* and the left heart pumps oxygen-rich blood through the *systemic circulation*. There are four valves, one at the exit of each heart cavity, which regulate blood flow in the heart and ensure bulk unidirectional motion through both pulmonary and systemic circulations.

Figure 2.1 Human heart.

The systemic circulation consists of a network of curved and branching vessels whose size decreases in the arteries, arterioles and capillaries and increases in the venules and veins. In particular, arteries distribute blood throughout the body and maintain blood pressure between heartbeats, arterioles transport blood to capillary beds, capillaries diffuse oxygen and nutrients to cells, and venules collect deoxygenated blood from capillaries and return it to the heart through veins. The topological pattern of the large systemic arteries is mainly a binary tree structure, with the exception of some arterial anastomoses, such as the palmar arch in the hand, the plantar arch in the foot, and the circle of Willis in the cerebral circulation, and some arteriovenous anastomoses in the skin and in the gut.

Blood consists of an aqueous solution (*plasma*) and platelets that is circulated by the heart through the vertebrate vascular system, carrying oxygen and nutrients to and waste materials away from all body tissues. It has a density similar to the water but its viscosity is more than twice the viscosity of water.

2.2 Classification of models

Cardiovascular system physiology has been object of study in the past. For example, Aristotele (384-322 a.C.) has identified the rule of blood vessels in the propagation of the "animal heat" from the heart to the rest of the body. Later, a lot of scientists, like Prassagora, Galeno, Sir William Harvey, Leonard Euler and Daniel Bernoulli have focused their work on this matter. In XIX century, J.P. Poiseuille, physic and physician, has identified the first simplified mathematical model of the flux in a cylindrical tube. Then, in XX century, O. Frank has proposed a model of the circulatory system using the electrical analogy. In recent years there was a strong improvement of these models, in order to obtain more accuracy in simulations.
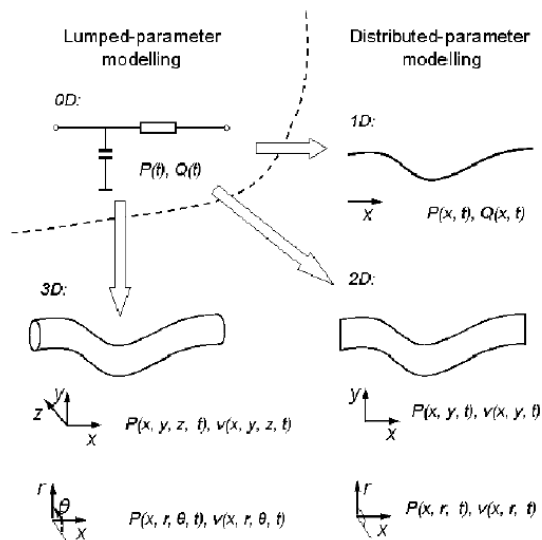
Figure 2.2 Different models.

The cardiovascular system can be classified in time domain and frequency domain. Usually representations on frequency domains are based on the linearisation of governing equations. These simplified equations are solved using Laplace or Fourier transform. If

non-linear terms are considered, the time domains must be used. Representation models can have a dimension from 0-D to 3-D, depending on the accuracy (see [32], [39]). Usually models with lumped parameters are used for 0-D models, in which parameters are spatial distributed in discrete way, that is all the elastic, inertial and resistive effect is concentrate in one point and it represents globally the behavior of a particular district (organ, vessels, portions of vessels), while higher dimensions models allow the variation of this parameters with continuity in the space, so they use distributed parameters models. These models are illustrated in Figure 2.2, where Q, P and v are, respectively, flux, pressure and velocity.

Zero-dimensional models are usually described by two ordinary differential equations for each partition, which represent mass and momentum conservation, with an algebraic relation of equilibrium which connects volume of the partition and pressure. One, two and three dimensional models consist in partial differential equations, which describe mass and momentum conservation (Navier-Stokes equations), with the addition of equilibrium equations. It is possible to observe that when Navier-Stokes equations are discretized and the convective term is excluded, a 0-D model is obtained. In cardiovascular dynamics, 1-D models represent easily wave transmission effects, 2-D models describe radial velocity variation in an axisymmetric canal, while 3-D models give solutions for complex flux models. A classification about dimensions and applications of these models is in table 2.1.

2.2.1   0-D models

0-D models are used in order to simulate blood flow dynamics in the entire circulatory system. In the definition of the 0-D model, usually the hydraulic-electric analogy is used. In fact, in general, blood flow in the circulatory system and electric conduction in a circuit are very similar: blood pressure permits that the blood circulates against hydraulic impedance; similarly, voltage in a circuit permits the flux against electric impedance.

Table 2.1 Comparing models for studies of cardiovascular dynamics.

Method of study			Suitable research target
Time	0D (lumped parameter) model		Global cardiovascular dynamics in the whole circulation system; General pressure and flow-rate changes in a local circulation loop; possibly to provide boundary conditions for local 3D models
domain	Distributed	1D	Pulse wave transmission; improved boundary conditions for 3D local models, capable of capturing systemic wave reflections effects
study	parameter	2D	Local flow field study in axisymmetric domains; further improvement of boundary conditions for local 3D models, but limited applicability
	model	3D	Local flow field study in full 3D domains
Frequency domain study			Frequency response analysis of cardiovascular system after linearization

Blood flow is described by the continuity equation for mass conservation, Poiseuille law for steady state equilibrium and Navier-Stokes equations for non-steady state equilibrium; electrical flux is governed by Kirchhoff law, Ohm law for voltage-power relation and transmission equation for high frequency voltage-power relation. So, representing blood pressure and flow using voltage and power, describing effects of inertia and friction force in the blood flow with resistance R, inductance L and compliance C in the circuit, it is possible to use and apply in the study of cardiovascular dynamics known methods, already well defined for the analysis of electrical circuits. However these models are not able to describe non linear problems typical of cardiovascular mechanism.

There are a lot of 0-D models. The most simple is Windkessel model, which describes the vascular system from aorta to capillaries with a capacity C connected in parallel to a resistance R, while the most complete one is Guyton model, where the most of the branches from the arteries to veins are represented as effects of autonomic and hormonal regulation. These models can be divided in two classes: *mono-compartment models* and *multi-compartment models*.

Mono-compartment models

In these models, the whole vessel network is described by a single combination of resistance-compliance-inductance (RLC).
In the following figure there are some examples of models.
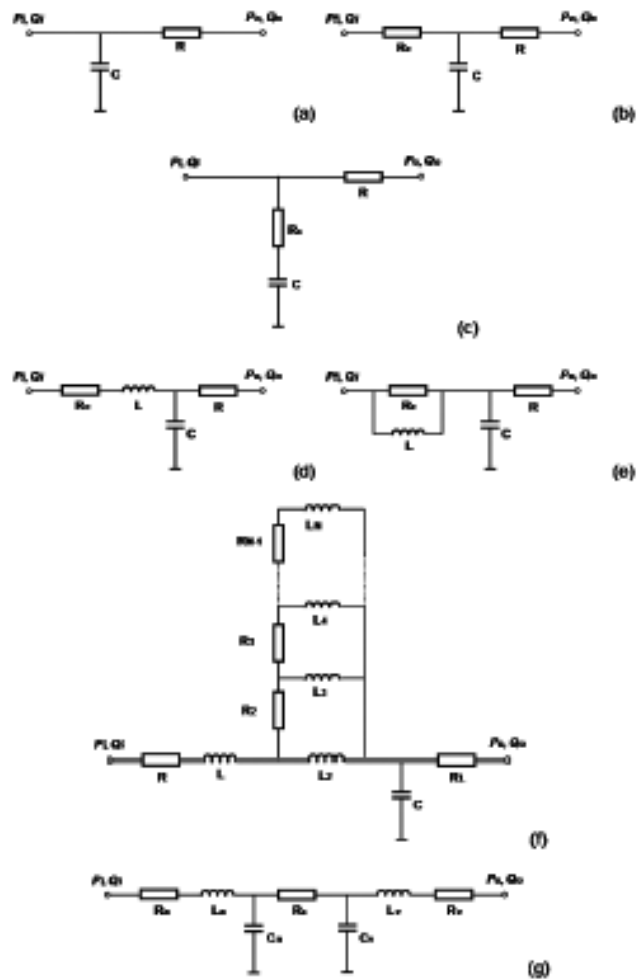
Figure 2.3 Mono-compartment models for vessel networks.

The simplest mono-compartment model is two-elements Windkessel model, proposed by Stephen Hales in 1733 and then formulated mathematically by Otto Frank in 1899. This model consists of two elements connected in parallel, a capacitor C and a resistance R. It describes only the arteries, non considering vessels and capillaries. This model was extended by Landes, introducing an other resistance element R_c (*characteristic resistance*), which is connected in series with Windkessel RC model (Figure 2.3, (*b*)), so to obtain the RCR model. This one was studied by Westerhof and it is often called Westkessel. The second resistance represents the impedance of the network of arteries, defined as the ratio between pressure and capacity without reflective waves. The total resistance R_c+R has the same value of the resistance in the previous RC model, and the capacity C represents the elasticity effect of the arteries network. Experiments and numerical studies have shown that RCR models provide a good representation in the prevision contest of the systolic volume and systolic and diastolic aortic pressure, even if it underestimates significantly the peak of the aortic flow, the mean arterial pressure and it does not provide a realistic aortic pressure. At the same time, Burattini e Natalucci have developed a different RCR model, in which there is a small resistance R_c connected in series with the condenser C, instead of RC combination (see Figure 2.3, (*c*)). In this configuration, the small resistance R_c is conceptually connected with the condenser C in order to describe viscoelastic proprieties of the vascular wall, in contrast with the rule that it had in the model previously described, in which it captures the wave's reflection. Landes and Westerhof have extended the RCR model considering the inertial effect of the blood flow, and they have obtained, respectively, the RLCR1 model (Figure 2.3, (*d*)) and the RLCR2 model (Figure 2.3, (*e*)). The use of the inertial term L helps to improve the accuracy of the model. From several experimental studies on these models, it has been proved that the RLRC1 is the best one in order to model the vascular impedance. However, with the addition of more elements, the identification of model's parameters is more difficult. To improve the arteries' model, Westerhof has
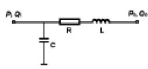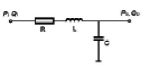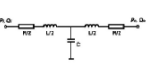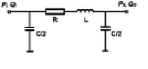
extended the RCR model including more R and L components
(Figure 2.3, (f)), in order to simulate the *sleeve effect*, which is
the impedance of the laminar oscillatory flow. These models are
not very appropriate for complex vascular networks, so new mod-
els have been introduced with the addition of further R, C and
L elements. The RLCRCLR model (Figure 2.3, (g)) permits to
describe all the characteristics of the vascular system, but it can
be interpreted like a connection in series of a RLC model for the
arterial subsystem, a resistance model for capillaries and another
RLC model for the venous subsystem. In this case it can also be
considered as a multi-compartment model.

Multi-compartment models

In the mono-compartment models, the entire vascular system is
considered like one block, so the internal distribution of pres-
sure and capacity in the different segments of the vascular net-
work is not computed. In order to improve these lacks, multi-
compartment models have been developed. In these model the
vascular system is divided in a certain number of segments and
each segment is described by a resistance R, a capacity C and an
inductance L. The number of segments is decided in connection
with the level of accuracy required. In the construction of multi-
compartment models for vascular network, it is necessary to find
the RLC models appropriate for each segment of the blood ves-
sel. However these models are developed in order to describe units
of the vascular system and are not the most suitable to describe
its components, in fact characteristics of vascular segments are,
in general, very different from the ones of the system. Formaggia
and Veneziani [16], Milisic and Quarteroni [22], after having ex-
amined already existent models, have provided detailed results on
the typical four-compartment model appropriate for the study of
a vascular segment. In these results, the blood flow in a vascular
segment is considered through a mono-dimensional formulation,
and the mean capacity and pressure inside the vascular segment
are assumed to be equal to input or output values (it depends on

the specific formulation). The four network elements have been labeled as shown in the following table.

Table 2.2 Four typical models of vascular segments as blocks of a model with more compartments in the vascular network.

Network element	Circuit model	Corresponding boundary condition
Inverted L element		Upstream flow-rate Q_i and downstream pressure P_0
L element		Upstream pressure P_i and downstream flow-rate
T element		Upstream and downstream pressure P_i and P_0
⊓ element		Upstream and downstream flow-rate Q_i and Q_0

Each one is used with suitable combinations of boundary conditions. Among these configurations, the inverted L element uses inflow and outcoming pressure like boundary conditions, and provides as result incoming pressure and outflow, which is common in fluid dynamic. The most common approach used is to divide the vascular system in segments that represent aorta, arteries, arterioles, capillaries and vessels, characterizing the network element with respect to the properties of local flux. Blood vessels are quite elastic in aorta and main arteries, so the blood flow is variable and the effects of resistance, capacity and inductance (RLC combination) must be considered. In arterioles and capillaries, the wall of the vessel is more rigid, so the flux is constant and there is a drop in friction force, so the dynamics of local flux are completely described by one resistance element. Vessels and the caval vein have a constant blood flux, so the inertial effect can be ignored and a RC combination can be considered in order to describe the characteristics of the capacity. This is showed in the following fig-

ure:
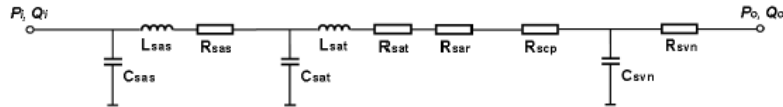
Figure 2.4 Multiple compartimental model for the vascular system, proposed by Shi. (sas: root of the aorta; sat: artery; sar: arteriola; scp: capillary; svn: vein)

Parameters configuration for 0-D models

Generally it is hard to estimate the correct values for the parameters of the model. Theoretically the initial values of the parameters of 0-D models can be obtained by pressure/capacity data, measured in some positions of the cardiovascular system. However some difficulties make this work very hard. In particular the accuracy of the parameters of the model is influenced by the invasive nature of many measurements, the limited access in some parts of the system due to the anatomic configuration, practical difficulties connected with the orientation of the probe of the flux and with the synchronization of pressure and flux data, the limited precision of the sensor of pressure/capacity. In addition, since the 0-D model is an abstraction of the vascular system and not a punctual mapping of the anatomy of the circulatory system, it is difficult to find other positions of the system, in order to make more measurements of pressure/capacity and provide useful information for the improvement of the structure and the parameters of the model. So, if there is a set of possible values for the parameters it is hard to understand which one is the most appropriate for the model. The derivation of the parameters of the model is based on the multivariate linear/non linear regression analysis. When the structure of the model is simple and the number of the elements (such as the number of R, L, C components) is small, the regression analysis is

easy and sometimes it could be linearized. If the model becomes more sophisticate, this is not true, so it is difficult to find the right combination of the parameters for the model and the regression analysis leads to poor results. In this case the only solution is to find appropriate intervals for each parameter and then to assign different combinations for the parameters of the model and to observe if the obtained output corresponds with the measured data of pressure/capacity. This procedure is repeated until it is obtained an acceptable combination of the values of the parameters, but it results very much expensive in time, and the obtained results are right only from a mathematical point of view, without having any informations about the correctness of the physical interpretation.

0-D models applications

The research about 0-D models for the cardiovascular system has been active for more than 200 years, since the Windkessel model was introduced. 0-D model are widely used in several area of the cardiovascular studies, from the basic research of cardiovascular physiology to astronautical medicine and the analysis for the design of cardiovascular artificial organs. Figures 2.5, (a)-(c) show some examples of simulation results, including pressure, capacity and volume changes in the systemic circulation of a healthy human person.
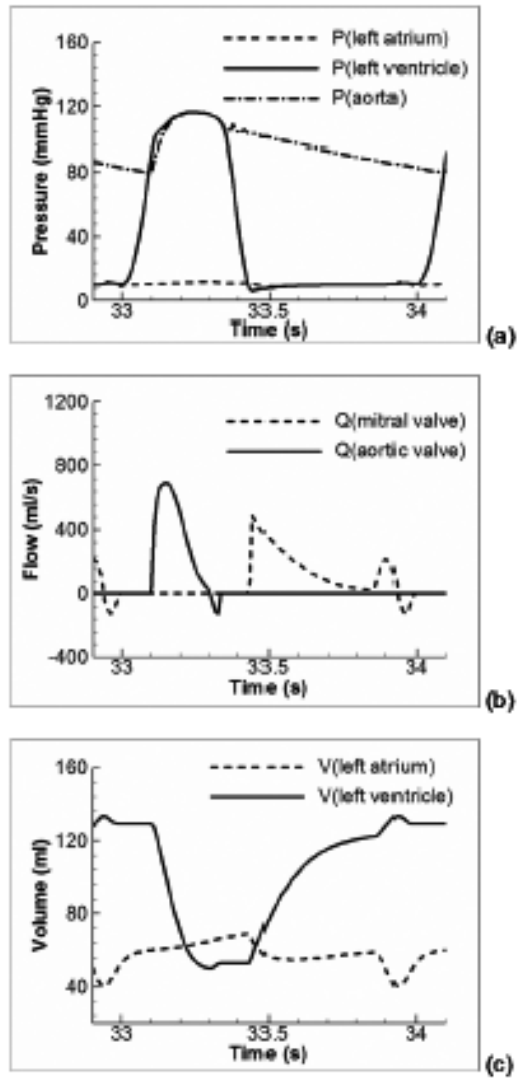
Figure 2.5 (a) Pressure variation; (b) Variations in the flux of cardiac valves; (c) Volume variations in the two left cavities of the heart.

2.2.2   1-D cardiovascular models

The propagation of waves of pressure and capacity of the blood flow in the vascular system is one of the most interesting problems in the study of cardiovascular physiology. It is believed that the main information about the cardiac functionality, elastic properties of blood vessels, physiological conditions about important organs (brain, liver, kidney, etc.) are contained in these two waves and their relations. So, the research about cardiovascular problems has given much attention to the study of these waves.

It is possible to assure that a model composed by a sequence of 0-D components is, to the limit, a representation of a 1-D system. In fact, Milisc and Quarteroni [22] have proved that it is possible to consider 0-D models for the vascular network as a first order discretization of one-dimensional linear systems, which are easily interpreted in terms of electrical models. The biggest difference between multiple-linear 0-D models and 1-D models is in the fact that the last ones can include the convective term (non linear).

2-D and 3-D models of fluid dynamics can reveal the exact pressure and the distribution of the velocity in a specific segment of the vascular network, but there are limits due to the computational power. So, a 1-D model can offer more advantages in revealing pressure and flow variations for the entire length of the considered vessel. Canic and Kim [7] have studied in details the characteristics of the Navier-Stokes equations and they have proved that, if the radius of the vessel is small with respect to a length of the characteristic wave, the equation of the radial momentum imposes that the pressure is constant for each section. Being this hypothesis valid for vascular fluxes, the deriving 1-D models, usually formulated with flow, pressure and area as main variables, are appropriate for these systems.

There are several complications (some non linear) in the study of the propagation of the pulse waves in 1-D models, like the thinning of blood vessels (which causes other variations of the convective acceleration), the bifurcation of vessels, the non linear relations between pressure/cross area for the vascular wall, the axial ten-

sion, the collapse of veins and pulmonary vessels, etc. The non linear relation between pressure and cross area section and constitutive relations have permitted to derive the governing equations of the model. Brook and Pedly [6], Porenta [31], Formaggia [13], Rooz [34], Sherwin [37], [38] have included also the effect of the tapering of the vessels, considering the cross section variable at the beginning of the vessel.

Solution Methods

The governing equations of the 1-D pulse wave propagation are hyperbolic equations and the dynamic of such wave are determined by two Riemann invariants of the system (also called characteristic quantities, equals to the blood pressure plus/minus the product between characteristic flux and impedance, where the characteristic impedance has the same meaning of the characteristic resistance introduced previously for 0-D models). In order to solve the governing equations, Streeter [42], Bodley [2], Parker and Joans and Wang [28], [47], [48] apply the characteristic method, where the partial differential equation for continuity and momentum are replaced by ordinary differential equations on the characteristic lines corresponding at the two Riemann invariants. The governing equations have also been solved using finite differences methods, but, in recent years, the finite volume method and the finite elements method have been applied too. Brook and Pedley [5], [6] have used a Godunov scheme to discretize the equations in a finite volume formulation; Sherwin [38] has solved these equations using a discontinuous Galerkin scheme and a Taylor-Galerkin one. A small number of researchers has also used the spectral method for the solution of the pulse wave equations, like Bessem that, for example, has applied the residue method in order to transform the equations in a spectral space. Sherwin has applied the spectral/hp method.

Boundary conditions

The equations for the transmission of the 1-D pulse waves are hyperbolic and in the majority of the physiologic conditions the blood flow is *sub-critical*, and it must be assigned a boundary condition to each extremity of the vessel. At the upper extremity it is possible to prescribe boundary conditions on pressure or capacity of the flux, using theoretic derivations or experimental results. At the lower extremity, the boundary condition requires more observations, in fact, in physiological conditions, arteries are branched and connected with smaller arterioles and these ramifications can be very deep, so it is impossible to track all these ramifications in one simulation, and it is necessary to decide the section to model, concerning with the scope of the specific study.

A large number of researchers have adopted a more simple approach that consists into specify directly the admissible combinations for the pressure and the capacity of the incoming and exiting flux. In order to have more realistic conditions, some researchers have used a constant or variable resistance or a three elements Windkessel model (RCR) to specify the relation between exiting pressure and capacity. To improve the accuracy of the boundary condition, Olufsen [25] has proposed the structured tree model in which the impedance of the small arteries is estimated using linearized Navier-Stokes equations. It seems to be that this model has improved the simulation results, but no validation has been published yet. A special type of boundary condition internal to a segment of the vessel is the vascular ramification, where a parent vessel is ramified in several daughters vessels. Many researchers have applied directly the same static pressure and capacity conservation to the ramifications points. A better description (which satisfies the Bernoulli equation for the steady state) has been adopted by Sherwin [38], who has applied the continuity of the total pressure instead of the static pressure. To explain the wave reflection in the branch point, Reymond [33], Wang and Parker [47] have used wave reflection coefficients to compute pressure and capacity variations. Smith [40] has considered momentum conservation in

the bifurcations of the vessels, computing the equilibrium between the differences of pressure and inertia.

1-D models applications

Traditionally 1-D models for the transmission of the pulse waves are mostly been applied to study the dynamics of the transmission of pulse waves in arteries segments (see Bodley [2], Streeter [42], Parker and Joans [28] works). Wang and Parker [47], [48] have extended the study in order to investigate the dynamic of propagation waves in the vascular segments in a complete arterial network of the human body; Li and Cheng [19] have studied the characteristics of the pulse waves in the arterial pulmonary network; Porenta [31] and Rooz [34] have analyzed the characteristics of the pulse waves in arteries with stenosis; Wan [44] and Steele [41] have determined the dynamic of the pulse wave in sick vessels with grafts of by-pass; Surovtsova [43], Sherwin [38], Pontrelli and Rossoni [29] have studied the transmission of the pulse wave in arteries with stents; Reymond [33] has modelled the propagation of the pulse wave in an arterial systemic tree.

Many researchers have considered the transmission of the impulse waves in collapsible vessels: Elad [10] has studied the instable flux of the fluid through collapsible tubes; Brook [5], [6] has modeled blood flux in the jugular vein of a giraffe.

Another development in 1-D modeling of the pulse wave transmission consists in the analysis of the intensity of the wave, proposed by Park and Joans, where the product of the variations of pressure and velocity on a small interval is defined as estimation of the rate of the flux of energy per unit of area in a segment of the vessel. Such index describes, precisely, the intensity of the wave and it can be used to distinguish forward transmission wave from backward transmission wave. The analysis of the intensity of the wave has been severely applied to the study of the transmission of the pulse wave in the left ventricle, in coronary arteries, in systemic and pulmonary arteries. However, it is necessary to observe that 1-D models are valid in such applications only if the flux has an

axial domain and the secondary flux in radial and circumferential directions is negligible.

2.2.3 Multi-scale models

The cardiovascular system is a closed network with strong interactions among its components. Underlining only global dynamics of circulation or only local topics of the flux can provide only partial information on the entire cardiovascular analysis. In latest years multi-scale modeling techniques have been developed, where 0-D models are coupled to 1-D, 2-D or 3-D models, in order to provide complete representations of the cardiovascular system. Typically, local hemodynamic is determined through a detailed and realistic 3-D anatomic model of an organ or a region of interest, and boundary conditions for this model are given by 0-D or 1-D models. Quarteroni has introduced a first multi-scale model in which the different models' scale have different mathematical characteristics: 0-D models with lumped parameters are governed by ordinary differential equations, 1-D models with distributed parameters can be described by hyperbolic partial differential equations; 2-D and 3-D models are based on Navier-Stokes equations, which are strongly non linear and its behavior can be parabolic, hyperbolic or elliptic, according to the specific problem. An accurate treatment at the interfaces, that are the connection points between different models, is necessary to guarantee that the problem is mathematically well posed. Due to the fact that the blood flow, in most of the physiological/pathological conditions, is subcritical, a boundary condition must be assigned for every considered part of each multi-scale mode. In 0-D models, boundary conditions for pressure and capacity are directly applied; on 1-D, 2-D or 3-D models with distributed parameters, boundary conditions can be prescribed values for the variables in governing equations or for the derivatives of the variables or for a linear combination of variables and their derivatives. 0-D and 1-D models use pressure and velocity (or capacity of the flux) as variables, integrated on a transversal plane (the unvarying pressure on a transversal plane

is due to the radial momentum equation, while the distribution of the velocity in the convective non linear term can be represented by a corrective coefficient). 2-D and 3-D models often use pressure and velocity as primary variables.

A multi-scale model will include a strategy for the coupling of the components in single scale. Pontrelli [30] has associated a 1-D model for the transmission of the arterial pulse wave to two 0-D models, which represent the components previous and next the 1-D section. The previous 0-D model provides the capacity at the inlet and the next 0-D model provides the outcoming pressure and boundary conditions for the 1-D model, while the 1-D model computes pressure and capacity as boundary conditions for previous and next 0-D model, respectively. In a similar model, Formaggia [12] has incorporated a 1-D model for the aorta in a 0-D systemic cycle. It has been applied an inverse strategy respect to the previous one. Another problem that is verified when 2-D or 3-D models are associated, is due to the treatment of insufficient boundary conditions: the lack of information makes insufficient the description of the capacity in 0-D/1-D models, so they can not be applied as boundary conditions for 2-D/3-D models. Watanabe [49] has done a multi-scale simulation of the dynamics of fulfilling on the left ventricle, in which a 3-D model for the ventricular blood flow has been integrated with a 0-D model for the other parts of the circulatory system. The 0-D model provides the pressure as boundary condition for the 3-D model, and the 3-D model specifies the variation of the capacity for the 0-D model. Vigono-Clementel [46] has applied a 0-D model, which provides values of resistance/impedance as boundary conditions for the 3-D arterial model, for which there is the pressure-capacity relation at the interfaces of the model. In this case, the profile of the outcoming velocity for the 3-D model has been represented as Poiseuille flux for the boundary condition on the resistance and as a linear wave solution of Womersley for the boundary condition of the impedance. In the analysis of blood flow in conform vessels, Formaggia [13] has coupled a 1-D model and a 3-D one to reduce the computational complexity and to delete the effect

of outcoming pressure waves. To obtain the missing information at the interfaces of the model, he has proposed two approaches to find the admissible pressure and the distribution of the velocity: a variational approach and another one which uses Lagrange multipliers. In other studies Formaggia [16], [17] has also elaborated the two approaches and he has verified that, for problems of transitory flux, the Womersley profile is an admissible flow distribution.

Chapter 3

1-D model for the cardiovascular system

In this chapter a 1-D model for defining the evolution of the blood pressure and the velocity of the propagation wave in the circulatory system is introduced. After justifying the choice of a 1-D model for the system, the governing equations are presented and manipulated in order to obtain the velocity of the propagation wave and the characteristic variables of the system, and to separate backward and forward waves. The formulation is solved using the discontinuous Galerkin scheme, with appropriate boundary conditions, considering inflow conditions, outflow conditions and junctions. The described equations are also linearized in order to study the effect of non linear terms on the wave propagation.

3.1 Assumptions for the 1-D formulation

The cardiovascular system consists of a large number of vessels, so it is very hard to use a 3-D model to study the whole system. In order to reduce the complexity it is possible to use a 1-D model, considering only the large arteries.
Each artery is approximated by an impenetrable 1-D tube of length

l, axis s, circular cross section $A(s, t)$, perpendicular to s, and thickness $h(s)$, with uniform properties along the circumference. A can vary during the time (it depends on t), in fact the arterial wall is deformable. Assuming that the curvature s is small enough, it can be approximated by the coordinate x and the problem can be described in one spatial dimension. This assumption is correct in large arteries because the curvature is very small respect to the diameter.
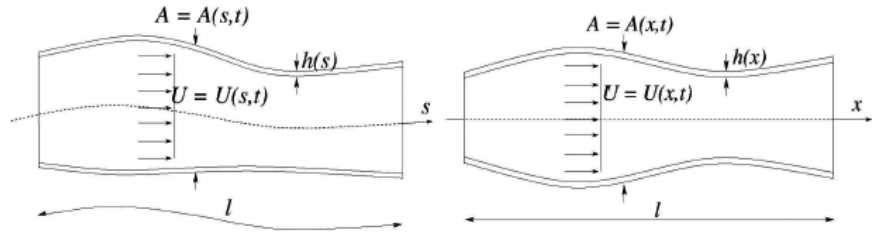
Figure 3.1 Layout of a blood vessel: natural layout (left) and layout with 1-D approximations (right).

The 1-D formulation permits an efficient simulation of the problem, because the lengths of the pulse waves in the arteries are big if compared with their diameters, and this implicates that the propagation of the waves holds principally in the axial direction. However, some simplifications about the blood flow and a mechanic description of the arterial wall are introduced. The blood flow is described only along the axial direction with $U(x, t)$, defined as the average velocity across the cross section $A(x, t)$,

$$U = \frac{1}{R^2} \int_0^R 2ru \ dr,$$

where r is the radial coordinate, $R(x, t)$ is the lumen radius and $u(x, r, t)$ is the axial velocity of each fluid particle (assumed to be axialsymmetric) in the cross section $A(x, t)$. During the movement of the wall, it is assumed that the arterial wall can be deformed only in the radial direction. This deformity is due to the internal

pressure $p(x, t)$, considered constant on the cross section of the lumen. The external pressure beyond the arterial wall can be considered constant in time and space or it can be taken variable.

The fluid resistance, compliance and inertia of the arteries, arterioles and capillaries non simulated in the 1-D model, are included considering linear models with lumped parameters (or 0-D models), in which pressure and capacity of the flux are only time dependent. These are connected with the 1-D formulation through boundary conditions.

The blood can be considered as a homogeneous, incompressible and Newtonian fluid in a normal arterial flux. So, both the viscosity μ and the density ρ are considered constant or dependent only by the temperature that can be treated as a parameter, without the necessity of introducing a thermodynamic state equation or an energy equation. In addition, the blood is supposed to be laminar[1], because the Reynolds' numbers[2] in the all system are well below 2000 in normal conditions.

3.2 Governing equations

Blood pressure and velocity pulse wave propagation in each artery are simulated putting together the blood flux problem with the moving of the arterial wall.

The governing equations are given by the mass and momentum conservation equations, applied to a 1-D tubolar and straight control volume (see Figure 3.1) of incompressible and Newtonian fluid.

---

[1]The fluid particles move following coaxial cylindric foils, of infinitesimal thickness, which slides one on the other without any type of reshuffling of the fluid, with increasing velocity form the periphery to the center. It is in contrast with the turbolent regime, which is typical of vessels with stenosis and it is generated close to them. It causes noises, so it can be found thorough auscultations. In addition it can originate an increase in the resistance of the fluid.

[2]Reynolds' numbers are adimensional numbers, used in fluiddynamic which are proportional to the ratio between inertial and viscous forces. They permit to evaluate if the flow of a fluid is laminar (if the number is smaller) or turbolent (when the number is higher).

The conservation of the mass requires that the variation of the mass inside plus the external net flux of the mass is equal to zero. Denoting the blood density with ρ, the volume with

$$V(t) = \int_0^l A \ dx,$$

where l is the length of the vessel, and assuming that there are not infiltrations across the walls, the mass conservation can be written as it follows:

$$\rho \frac{dV(t)}{dt} + \rho Q(l, t) - \rho Q(0, t) = 0.$$

Replacing $V(t)$, a mono-dimensional equation is obtained. Also, observing that

$$Q(l, t) - Q(0, t) = \int_0^l \frac{\partial Q}{\partial x} dx,$$

there is

$$\rho \frac{d}{dt} \int_0^l A(x, t) \ dx + \rho \int_0^l \frac{\partial Q}{\partial x} dx = 0.$$

If l is assumed to be not dependent from the time, the derivative with respect to t can be taken over under the integral, and there is

$$\rho \int_0^l \left\{ \frac{\partial A}{\partial t} + \frac{\partial Q}{\partial x} \right\} dx = 0.$$

Since the length l is not specified, the control volume is arbitrary and so the previous equation is valid for each value of l. So, in general, the integral is zero if the function in the integral is null:

$$\frac{\partial A}{\partial t} + \frac{\partial Q}{\partial x} = \frac{\partial A}{\partial t} + \frac{\partial(Au)}{\partial x} = 0.$$

Under the same hypothesis, the momentum equation requires that the variation of the momentum in the control volume plus the momentum of the external net flux corresponds to the forces applied, and this holds for an arbitrary length l:

$$\frac{d}{dt} \int_0^l \rho Q \ dx + (\alpha \rho Q u)_l - (\alpha \rho Q u)_0 = F,$$

where $Q = Au$ and F represents the forces applied in the direction of the axis x, operating on the volume control. Since

$$\rho Q = \rho u A = \rho \int_S \widehat{u} \; d\sigma,$$

represents the momentum integrated on the section S, the left member of this equation is similar to the left member of the mass conservation equation. However in the balance of the momentum, an adimensional correction factor α has been introduced, which considers the non linearity of the integration on the section, in terms of the local velocity $\widehat{u}$, that is

$$\int_S \rho \left(\widehat{u}\right)^2 d\sigma \equiv \alpha \rho u^2 A = \alpha \rho Q U \implies \alpha(x,t) = \frac{\int_S \widehat{u}^2 d\sigma}{a u^2}.$$

When the profile of the flux is uniform on a section, $\alpha = 1$. To complete the formulation it is necessary to define the force, indicated by F, which usually includes a contribute of the pressure and viscosity:

$$F = (pA)_0 - (pA)_l + \int_0^l \int_{\partial S} \widehat{p} n_x ds dx + \int_0^l f \; dx,$$

where ∂S is the border of the section S, n_x is the component with respect to the axis x of the normal at the surface and f represents the friction force per unit length. The pressure force, expressed by the double integral, can be simplified assuming constant the pressure on the section and treating the tube as axialsymmetric. So

$$\int_0^l \int_{\partial S} \widehat{p} n_x ds dx = \int_0^l p \frac{\partial A}{\partial x} dx.$$

By combining the last equations, the momentum conservation equation is obtained:

$$\frac{d}{dt} \int_0^l \rho Q \; dx + (\alpha \rho Q u)_l - (\alpha \rho Q u)_0 = (pA)_0 - (pA)_l +$$

$$+ \int_0^l p \frac{\partial A}{\partial x} dx + \int_0^l f \; dx.$$

The mono-dimensional equation is derived observing that

$$(\alpha \rho Q u)_l - (\alpha \rho Q u)_0 = \int_0^l \frac{\partial (\alpha \rho Q u)}{\partial x} dx,$$

$$(pA)_0 - (pA)_l = - \int_0^l \frac{\partial (pA)}{\partial x} dx.$$

Replacing this inside the latest equation and assuming l non depending from the time and ρ constant, there is

$$\rho \int_0^l \left\{ \rho \frac{\partial Q}{\partial t} + \rho \frac{\partial (\alpha Q u)}{\partial x} \right\} dx = \int_0^l \left\{ -\frac{\partial (pA)}{\partial x} + p \frac{\partial A}{\partial x} + f \right\} dx.$$

This relation is satisfied for each arbitrary length l and so it is verified only when the function in the integrals are the same. So the momentum equation becomes:

$$\frac{\partial Q}{\partial t} + \frac{\partial (\alpha Q u)}{\partial x} = -\frac{A}{\rho} \frac{\partial p}{\partial x} + \frac{f}{\rho}.$$

Manipulating this equation again and remembering that $Q = AU$ e $\alpha U = \frac{Q}{A}$, the following system with hyperbolic partial differential equations is obtained:

$$\frac{\partial A}{\partial t} + \frac{\partial (AU)}{\partial x} = 0, \qquad (3.2.1)$$

$$\frac{\partial U}{\partial t} + (2\alpha - 1)U \frac{\partial U}{\partial x} + (\alpha - 1)\frac{U^2}{A} \frac{\partial A}{\partial x} + \frac{1}{\rho} \frac{\partial \rho}{\partial x} = \frac{f}{\rho A}. \qquad (3.2.2)$$

In the following, α is assumed constant (this means that the profile of the velocity is constant in shape) and defined as

$$\alpha = \frac{1}{U^2 R^2} \int_0^R 2r u^2 \, dr. \qquad (3.2.3)$$

The equations (3.2.1) and (3.2.2) can be also derived by integrating the 3-D incompressible Navier Stokes equations on a cross section.

In both cases, it is necessary to provide the shape of the radial velocity. In the following it will be used a velocity profile as the one proposed by Smith [40]

$$ u = U \, \frac{\gamma + 2}{\gamma} \, \left[1 - \left(\frac{r}{R} \right)^{\gamma} \right], \qquad (3.2.4) $$

where γ is constant. This profile satisfies the no-slipping condition $(u|_{r=R} = 0)$, it assumes axialsymmetric flux $(\partial u / \partial r|_{r=0} = 0)$ and it satisfies

$$ U = \frac{1}{R^2} \int_0^R 2ru \; dr. $$

Replacing (3.2.4) in (3.2.3),

$$ \gamma = \frac{2 - \alpha}{\alpha - 1}, $$

is obtained and, so, the velocity profile (3.2.4) can be expressed in terms of α as

$$ u = U \, \frac{\alpha}{2 - \alpha} \, \left[1 - \left(\frac{r}{R} \right)^{\frac{2-\alpha}{\alpha-1}} \right]. \qquad (3.2.5) $$

In the following $\gamma = 9$ ($\alpha = 1.1$) will be considered, which is the value chosen by Smith [40] in order to mimic the experimental data obtained in different point of the cardiac cycle. The Figure 3.2 shows the shape of the profile of this velocity, compared with a parabolic profile ($\gamma = 2$).
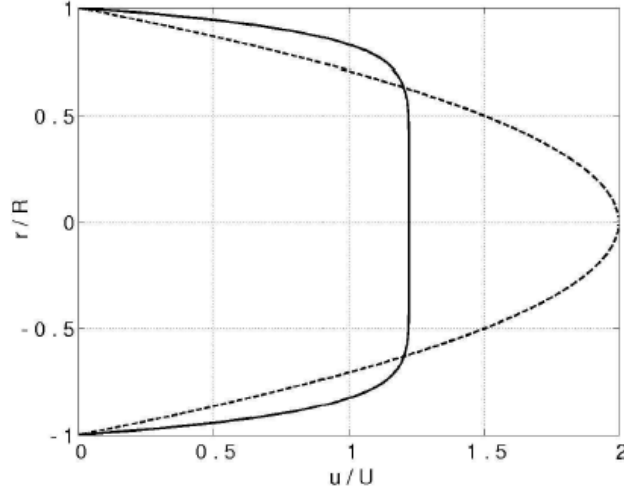
Figure 3.2 Shape of the velocity profile used by Smith [40] ($\gamma = 9$) (solid line) compared to a parabolic profile ($\gamma = 2$) (dashed line).

According to Brook [5], inertia terms $2(\alpha - 1)\,U\frac{\partial U}{\partial x}$ e $(\alpha - 1)\frac{U^2}{A}\frac{\partial A}{\partial x}$ of the momentum equation (3.2.2) are ignored. These terms take into account the fact that the profile of the velocity is not flat and they are very much smaller than the remaining ones in the momentum equation, which is reduced to

$$\frac{\partial U}{\partial t} + U\frac{\partial U}{\partial x} + \frac{1}{\rho}\frac{\partial p}{\partial x} = \frac{f}{\rho A}. \tag{3.2.6}$$

The integration of the incompressible 3-D equations of Navier Stokes, provides the following expression for $f(x, t)$:

$$f = 2\mu\frac{A}{R}\left[\frac{\partial u}{\partial r}\right]_R. \tag{3.2.7}$$

Replacing (3.2.5) in (3.2.7)

$$f = -2\mu\pi\,\frac{\alpha}{\alpha - 1}U = -22\mu\pi. \tag{3.2.8}$$

The equations (3.2.1) and (3.2.6) are completed with a pressure-area relationship or tube law: $p = p(A; x, t)$. This law considers

the lumen to be circular at any internal pressure and the arterial wall to be a linear, elastic and isotropic material with a small thickness compared to the vessel radius ($h << R$), so that the external forces applied at the arterial wall are reduced to stresses acting in peripheral directions. So, applying the Laplace law, by which the circumferential tensile stress, σ, depends on the pressure on the wall and the radius of the vessel

$$\sigma = \frac{R_0(p - p_0)}{h}, \tag{3.2.9}$$

is obtained, with p_0 and R_0, representing the pressure and the radius of the artery at the state $(A, p, U) = (A, p_0, U_0)$. The corresponding deformation on the circumference is

$$\epsilon = \frac{1}{1 - \nu^2} \frac{R - R_0}{R_0}, \tag{3.2.10}$$

where ν is the Poisson ratio (the ratio between cross and longitudinal deformations with respect to the direction of the flux), which it is assumed to be $1/2$ because the biological tissue is almost incompressible. The equations (3.2.9) and (3.2.10) are connected by $\sigma = E\epsilon$ (reformulation of the Hook's law), where $E(x)$ is the Young modulus (or elasticity modulus) along the circumference, which leads to the *tube law* used in the mono-dimensional model, also called algebraic model:

$$p = p_{ext} + \frac{\beta}{A_0}(\sqrt{A} - \sqrt{A_0}), \qquad \beta = \frac{\sqrt{\pi}hE}{1 - \nu^2}, \tag{3.2.11}$$

with p_{ext} the external pressure and $\beta(x)$ a parameter depending on the space and related to the mechanical proprieties of the arterial wall. Although the arterial wall behaves like a non elastic material, in this contest a linear elasticity will be assumed, so that the curves of pressure and the Young modulus can be approximated by straight lines in the physiological range of values (see Figure 3.3).
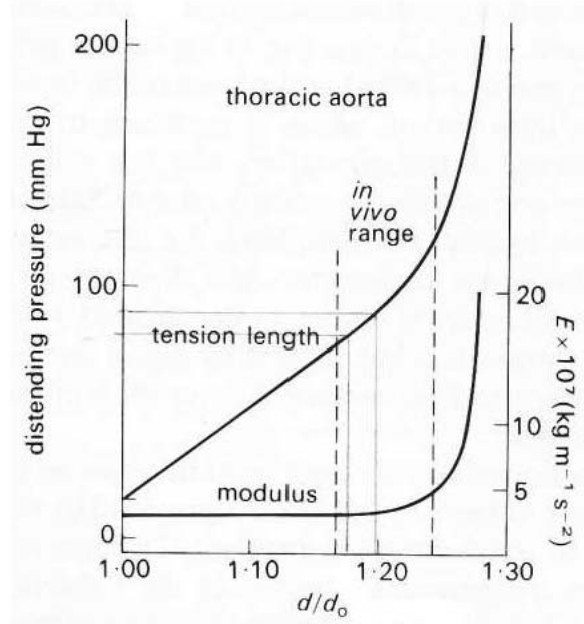
Figure 3.3 Graphic diameter-pressure for a piece of artery of fixed length (d_0 is the length not outstretched). This picture shows a typical no-linear behavior of a systemic artery. The studied range of value *in-vivo* is outlined by the two vertical dashed lines. The Young modulus (E) is also showed, which connects the circumferential tension and the circumferential deformation and it drastically increases when the pressure caused by the fluid on the walls exceeds the physiological range [21].

It is possible to observe that $\partial p/\partial A$ decreases when A increases in the tube law (3.2.11), contrary to the physiological behavior showed in Figure 3.3, in which the arterial wall becomes more rigid when p increases. In the same figure it is possible to observe that E grows in correspondence of an increasing in pressure. In the following, E will be supposed constant in a given section, but it can vary in each artery. Others fluid-structure interactions have been considered in the literature:
Visco-Elastic Model:

$$p = p_{ext} + \frac{\beta}{A_0}(\sqrt{A} - \sqrt{A_0}) + \frac{\Gamma}{A_0\sqrt{A}}\frac{\partial A}{\partial t},$$

Wall-Inertia Model:

$$p = p_{ext} + \frac{\beta}{A_0}(\sqrt{A} - \sqrt{A_0}) + \frac{\Gamma}{A_0\sqrt{A}}\frac{\partial A}{\partial t} + m\frac{\partial^2 A}{\partial t^2},$$

where $\Gamma = \frac{2}{3}\sqrt{\pi}\phi h_w$ is related to the visco-elastic properties of the arterial wall, while $m = \frac{\rho h_w}{2\sqrt{\pi A_0}}$ (see [14]).

3.3 Characteristic analysis

From the tube law (3.2.11), the term which defines the gradient of the pressure in the momentum equation (3.2.6) is

$$\frac{1}{\rho}\frac{\partial p}{\partial x} = \frac{1}{\rho}\left(\frac{\partial p}{\partial A}\frac{\partial A}{\partial x} + \frac{\partial p}{\partial \beta}\frac{d\beta}{dx} + \frac{\partial p}{\partial A_0}\frac{dA_0}{dx}\right),$$

and the equations (3.2.1) and (3.2.6) can be rewritten in the non-conservative form:

$$\frac{\partial \mathbf{U}}{\partial t} + \mathbf{H}\frac{\partial \mathbf{U}}{\partial x} = \mathbf{S}, \qquad (3.3.12)$$

where

$$\mathbf{U} = \begin{bmatrix} A \\ U \end{bmatrix}, \qquad \mathbf{H} = \begin{bmatrix} U & A \\ \frac{1}{\rho}\frac{\partial p}{\partial A} & U \end{bmatrix},$$

$$\mathbf{S} = \begin{bmatrix} 0 \\ \frac{1}{\rho}\left(\frac{f}{A} - \frac{\partial p}{\partial \beta}\frac{d\beta}{dx} - \frac{\partial p}{\partial A_0}\frac{dA_0}{dx}\right) \end{bmatrix}.$$

Since $A > 0$ and $\frac{1}{\rho}\frac{\partial p}{\partial A} > 0$, $\mathbf{H}$ has two real eigenvalues, $\lambda_{f,b} = U \pm c$, where

$$c = \sqrt{\frac{A}{\rho}\frac{\partial p}{\partial A}} \qquad (3.3.13)$$

is the velocity of the pulse wave of the system. Under physiological flow conditions, c is around one order of magnitude higher than U. So, there is $\lambda_f > 0$ and $\lambda_b < 0$. It is possible to rewrite the matrix $\mathbf{H}$ in the following way:

$$\mathbf{H} = \mathbf{L}^{-1}\mathbf{\Lambda}\mathbf{L}, \qquad (3.3.14)$$

where

$$\mathbf{L} = \varsigma \left[\begin{array}{cc} \frac{c}{A} & 1 \\ -\frac{c}{A} & 1 \end{array} \right], \qquad \mathbf{\Lambda} = \left[\begin{array}{cc} \lambda_f & 0 \\ 0 & \lambda_b \end{array} \right],$$

and ς is an arbitrary scale factor. Replacing (3.3.14) in (3.3.12) and premultiplicating (3.3.12) for $\mathbf{L}$, it is obtained

$$\mathbf{L}\frac{\partial \mathbf{U}}{\partial t} + \mathbf{\Lambda}\mathbf{L}\frac{\partial \mathbf{U}}{\partial x} = \mathbf{L}\mathbf{S}. \qquad (3.3.15)$$

With the change of variables

$$\frac{\partial \mathbf{W}}{\partial \mathbf{U}} = \mathbf{L}, \qquad (3.3.16)$$

where $\mathbf{W} = [W_f, W_b]^T$ is the vector of the characteristic or Riemann variables, the system (3.3.15) is reduced to

$$\frac{\partial \mathbf{W}}{\partial t} + \mathbf{\Lambda}\frac{\partial \mathbf{W}}{\partial x} = \mathbf{L}\mathbf{S}. \qquad (3.3.17)$$

If $\widehat{x}(t)$ is defined as a parametric function $\widehat{x} = \widehat{x}(t)$ in the space (x, t), then the variation of $\mathbf{W}$ along the curve $\widehat{x}(t)$ is given by

$$\frac{d\mathbf{W}(\widehat{x}(t), t)}{dt} = \frac{\partial \mathbf{W}}{\partial t} + \frac{d\widehat{x}}{dt}\mathbf{I}\frac{\partial \mathbf{W}}{\partial \widehat{x}}. \qquad (3.3.18)$$

A comparison between (3.3.17) and (3.3.18) shows that, if $\frac{d\widehat{x}}{dt}\mathbf{I} = \mathbf{\Lambda}$, then

$$\frac{d\mathbf{W}}{dt} = \mathbf{L}\mathbf{S}, \qquad (3.3.19)$$

along the path $\widehat{x}(t)$, that is $\mathbf{W}(\widehat{x}(t), t)$ depends only from its initial value and from the integration of $\frac{d\mathbf{W}}{dt}$ along $\widehat{x}(t)$. So, $\widehat{x}(t)$ defines the characteristic curves along which the information contained in $\mathbf{W}$ propagates in the space (x, t). Being $\frac{d\widehat{x}}{dt}\mathbf{I} = \mathbf{\Lambda}$, there are two characteristic paths, C_f e C_b, defined by

$$C_{f,b} \equiv \frac{d\widehat{x}_{f,b}}{dt} = \lambda_{f,b} = U \pm c. \qquad (3.3.20)$$
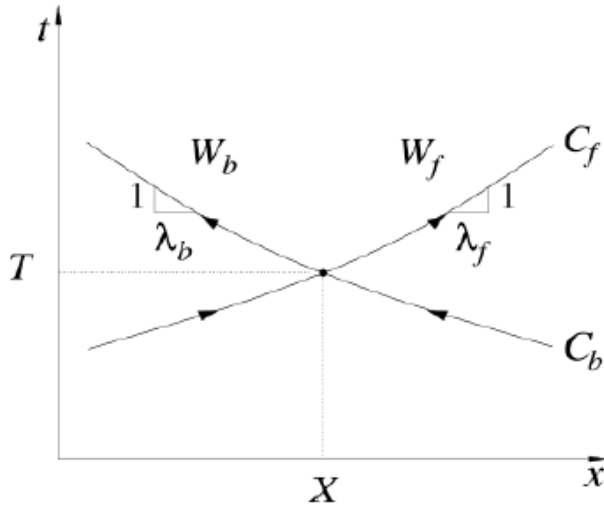
Figure 3.4 In the space (x, t), each point (X, T) of the domain is individuated by the intersection of one couple of characteristic paths C_f and C_b. W_f moves along C_f and transports information on pressure and velocity in the positive direction of the axis x. Similarly, W_b travels along C_b transporting th same information in the negative direction of the axis x

The characteristic analysis shows that the equations (3.2.1) and (3.2.6), combined with the tube law (3.2.11), create a non-linear system of hyperbolic differential equations.

In the space (x, t), W_f and W_b propagates along the paths C_f and C_b, respectively at the velocities λ_f and λ_b (Figure 3.4), changing their value because of viscous dissipation and geometrical variations, according to (3.3.19). Since $U << c$, W_f propagates the variations in pressure and velocity from proximal to distal parts of the arterial system (forward direction), while W_b transports information about pressure and velocity from distal to proximal parts (backward direction). It is possible to observe that, if $f = 0$ and β and A_0 are constant along x, then $\mathbf{S} = 0$, and this implies that the system (3.3.17) is decoupled and W_f and W_b are constant along C_f and C_b, for (3.3.19).

To satisfy Cauchy Riemann conditions,

$$\frac{\partial^2 W_{f,b}}{\partial A \partial U} = \frac{\partial^2 W_{f,b}}{\partial U \partial A},$$

the value of ς in $\mathbf{L}$ in (3.3.14) must be constant ($\varsigma = 1$ is considered in the following). The variables W_f and W_b are determined by the integration of (3.3.16),

$$W_{f,b} = U - U_0 \pm \int_{A_0}^{A} \frac{c}{A} \, dA. \tag{3.3.21}$$

Considering the tube law (3.2.11) and the expression (3.3.13) for the velocity,

$$W_f = U - U_0 + 4(c - c_0), \tag{3.3.22}$$

$$W_b = U - U_0 - 4(c - c_0), \tag{3.3.23}$$

is obtained, with

$$c = \sqrt{\frac{\beta}{2\rho A_0}} A^{1/4}, \tag{3.3.24}$$

and

$$c_0 = \sqrt{\frac{\beta}{2\rho}} A_0^{1/4}. \tag{3.3.25}$$

3.4 Wave separation

It is possible to obtain a better interpretation of the temporal evolution of pressure and flow measured at each point of the arterial system by separating backward and forward contributions that produce them. The technique proposed here is based on the work of Parker and Jones [28] which considers non-linear effects due to the convective acceleration and the non-linear dependence of p to A. Using the variable change (3.3.16), the variation of the Riemann functions, $d\mathbf{W}$, is connected to the variation of area and velocity, $d\mathbf{U}$, through the relation:

$$d\mathbf{W} = \mathbf{L}d\mathbf{U}. \tag{3.4.26}$$

If β and A_0 can be considered to be constant in a neighbourhood of the measurement site, the equation (3.3.13) provides $c = \frac{A}{\rho c}\frac{dp}{dA}$, so that the equation (3.4.26) gives

$$dW_f = dU + \frac{dp}{\rho c}, \tag{3.4.27}$$

$$dW_b = dU - \frac{dp}{\rho c}. \tag{3.4.28}$$

Solving it with respect to dp and dU,

$$dp = \rho c \frac{dW_f - dW_b}{2}, \tag{3.4.29}$$

$$dU = \frac{dW_f + dW_b}{2}, \tag{3.4.30}$$

are obtained. Since in the previous paragraph has been observed that W_f propagates changes in area (or pressure) and velocity forwards and W_b backwards, contributions of dp forwards, dp_f, and backwards, dp_b, are defined as:

$$dp_f = \rho c \frac{dW_f}{2}, \tag{3.4.31}$$

$$dp_b = -\rho c \frac{dW_b}{2}, \tag{3.4.32}$$

and contributions of dU forwards, dU_f and backwards, dU_b, as:

$$dU_f = \frac{dW_f}{2}, \tag{3.4.33}$$

$$dU_b = \frac{dW_b}{2}. \tag{3.4.34}$$

Replacing (3.4.27) and (3.4.28) in the equations from (3.4.31) to (3.4.34) holds to

$$dp_{f,b} = \frac{1}{2}(dp \pm \rho c dU), \tag{3.4.35}$$

$$dU_{f,b} = \frac{1}{2}\left(dU \pm \frac{dp}{\rho c}\right). \tag{3.4.36}$$

Finally, forwards and backwards contributions of pressure, $p_{f,b}$, and velocity, $U_{f,b}$, can be defined at each point by integrating with respect to the time, the variations of pressure $dp_{f,b}$ and velocity $dU_{f,b}$:

$$p_f = \int_{p_f(0)}^{p_f(t')} dp_f \ , \qquad p_b = \int_{p_b(0)}^{p_b(t')} dp_b, \qquad (3.4.37)$$

$$U_f = \int_{U_f(0)}^{U_f(t')} dU_f \ , \qquad U_b = \int_{U_b(0)}^{U_b(t')} dU_b. \qquad (3.4.38)$$

3.5 Linearisation of the governing equations

The system

$$\frac{\partial \mathbf{U}}{\partial t} + \mathbf{H} \frac{\partial \mathbf{U}}{\partial x} = \mathbf{S} \qquad (3.5.39)$$

is non-linear because of the convective term $U \frac{\partial u}{\partial x}$ in the momentum equation, the non-linear dependence of p by A through tube law (3.2.11), and the non-linear viscous term $\frac{f}{\rho A}$. If a perturbation is introduced at an initial state $(A, p, u) = (A_0, 0, 0)$ with small increments Δa, Δp, Δu, and quadratic terms are ignored, the system is reduced to

$$\frac{\partial \Delta \mathbf{U}}{\partial t} + \mathbf{H}_0 \frac{\partial \Delta \mathbf{U}}{\partial x} = \mathbf{S}_0, \qquad (3.5.40)$$

where

$$\Delta \mathbf{U} = \begin{bmatrix} \Delta a \\ \Delta u \end{bmatrix}, \qquad \mathbf{H}_0 = \begin{bmatrix} 0 & A_0 \\ \frac{\beta}{2\rho A_0^{3/2}} & 0 \end{bmatrix},$$

$$\mathbf{S}_0 = \begin{bmatrix} 0 \\ \frac{1}{\rho} \left(\frac{f_0}{A_0} - \frac{\partial \Delta p}{\partial \beta} \frac{d\beta}{dx} - \frac{\partial \Delta p}{\partial A_0} \frac{dA_0}{dx} \right) \end{bmatrix},$$

and $f_0 = -22\mu\pi\Delta u$. $\frac{\partial\Delta p}{\partial a}$ has been approximated by $\frac{\partial\Delta p}{\partial a}|_{a=0} = \frac{\beta}{2A_0^{3/2}}$, so

$$\Delta p = \frac{\beta}{2A_0^{3/2}}\,\Delta a = \frac{\rho(c_0)^2}{A_0}\Delta a, \qquad (3.5.41)$$

with c_0 defined in (3.3.25).

The characteristic analysis of the system (3.5.40) provides the following linear functions:

$$\Delta W_f = \Delta u + \frac{c_0}{A_0}\Delta a, \qquad (3.5.42)$$

$$\Delta W_b = \Delta u - \frac{c_0}{A_0}\Delta a, \qquad (3.5.43)$$

which propagate in the space (x, t) at constant velocities, respectively $+c_0$ and $-c_0$. The characteristic curves are straight lines defined by

$$C_{f,b} \equiv \frac{d\widehat{x}_{f,b}}{dt} = \pm c_0. \qquad (3.5.44)$$

3.6 Numerical solution: the discontinuous Galerkin formulation

The non linear system (3.3.12) of mono-dimensional equations can be solved using a discontinuous Galerkin scheme, with a spatial discretization *spectral/hp*. This method is appropriate for a 1-D formulation since it permits the propagation of waves of different frequencies without having big dispersion and propagations of errors.

First of all, the domain $\Omega = [0, l]$ of each artery is discretized in a mesh of N_{el} non overlapping elemental regions, $\Omega_e = [x_e^L, x_e^R]$, $e = 1, ..., N_{el}$, such that $x_e^R = x_{e+1}^L$ for $e = 1, ..., N_{el} - 1$ and $\cup_{e=1}^{N_{el}}\Omega_e = \Omega$. The superscripts L and R refer to the left and right boundaries of each elemental region Ω_e. In addition, the system (3.3.12) can be written in conservative form:

$$\frac{\partial\mathbf{U}}{\partial t} + \frac{\partial\mathbf{F}}{\partial x} = \mathbf{S}, \qquad (3.6.45)$$

where

$$\mathbf{U} = \begin{bmatrix} U_1 \\ U_2 \end{bmatrix} = \begin{bmatrix} A \\ U \end{bmatrix}, \qquad \mathbf{F}(\mathbf{U}) = \begin{bmatrix} F_1 \\ F_2 \end{bmatrix} = \begin{bmatrix} AU \\ \frac{U^2}{2} + \frac{p}{\rho} \end{bmatrix},$$

$$\mathbf{S}(\mathbf{U}) = \begin{bmatrix} S_1 \\ S_2 \end{bmatrix} = \begin{bmatrix} 0 \\ \frac{1}{\rho}\left(\frac{f}{A} - \frac{\partial p}{\partial \beta}\frac{d\beta}{dx} - \frac{\partial p}{\partial A_0}\frac{dA_0}{dx}\right) \end{bmatrix}.$$

The weak form of the system is obtained by multiplying the equation (3.6.45) by a vector of test functions $\mathbf{\Phi}$ and integrating over Ω:

$$\left(\frac{\partial \mathbf{U}}{\partial t}, \mathbf{\Phi}\right)_\Omega + \left(\frac{\partial \mathbf{F}}{\partial x}, \mathbf{\Phi}\right)_\Omega = (\mathbf{S}, \mathbf{\Phi})_\Omega, \qquad (3.6.46)$$

where

$$(\mathbf{w}, \mathbf{v})_\Omega = \int_\Omega \mathbf{w}\mathbf{v}\, dx. \qquad (3.6.47)$$

The integrals are decomposed into elemental regions as follows:

$$\sum_{e=1}^{N_{el}} \left(\left(\frac{\partial \mathbf{U}}{\partial t}, \mathbf{\Phi}\right)_{\Omega_e} + \left(\frac{\partial \mathbf{F}}{\partial x}, \mathbf{\Phi}\right)_{\Omega_e}\right) = \sum_{e=1}^{N_{el}} (\mathbf{S}, \mathbf{\Phi})_{\Omega_e}, \qquad (3.6.48)$$

and the second member of (3.6.48) is integrated by parts:

$$\sum_{e=1}^{N_{el}} \left(\left(\frac{\partial \mathbf{U}}{\partial t}, \mathbf{\Phi}\right)_{\Omega_e} - \left(\mathbf{F}, \frac{d\mathbf{\Phi}}{dx}\right)_{\Omega_e} + [\mathbf{F}\cdot\mathbf{\Phi}]_{x_e^L}^{x_e^R}\right) = \sum_{e=1}^{N_{el}} (\mathbf{S}, \mathbf{\Phi})_{\Omega_e}. \qquad (3.6.49)$$

The solution $\mathbf{U}(x,t)$ is approximated by a discretized expansion denoted by $\mathbf{U}^\delta(x,t)$ and, in the same way, $\mathbf{\Phi}(x)$ is approximated by $\mathbf{\Phi}^\delta(x)$. As basis for the expansion, polynomials of degree K have been chosen on each elemental region Ω_e. In addition, to obtain a global solution in the domain Ω, information must propagate between elemental regions Ω_e and this is achieved by upwinding the boundary flux, which is denoted as $\mathbf{F}^u$. In this way,

$$\sum_{e=1}^{N_{el}} \left(\left(\frac{\partial \mathbf{U}_e^\delta}{\partial t}, \mathbf{\Phi}_e^\delta\right)_{\Omega_e} - \left(\mathbf{F}(\mathbf{U_e^\delta}), \frac{d\mathbf{\Phi}_e^\delta}{dx}\right)_{\Omega_e} + [\mathbf{F}^u\cdot\mathbf{\Phi}_e^\delta]_{x_e^L}^{x_e^R}\right) =$$

$$= \sum_{e=1}^{N_{el}} (\mathbf{S}(\mathbf{U_e^\delta}), \mathbf{\Phi}_e^\delta)_{\Omega_e}, \qquad (3.6.50)$$

is obtained. Integrating again the second term by parts:

$$\sum_{e=1}^{N_{el}} \left(\left(\frac{\partial \mathbf{U}_e^{\delta}}{\partial t}, \mathbf{\Phi}_e^{\delta} \right)_{\Omega_e} + \left(\frac{\partial \mathbf{F}(\mathbf{U_e^{\delta}})}{\partial x}, \mathbf{\Phi}_e^{\delta} \right)_{\Omega_e} + \right.$$

$$\left. + [(\mathbf{F}^u - \mathbf{F}(\mathbf{U_e^{\delta}})) \cdot \mathbf{\Phi}_e^{\delta}]_{x_e^L}^{x_e^R} \right) = \sum_{e=1}^{N_{el}} (\mathbf{S}(\mathbf{U_e^{\delta}}), \mathbf{\Phi}_e^{\delta})_{\Omega_e}. \qquad (3.6.51)$$

To simplify the method, each elemental region is mapped onto the standard element $\Omega_{st} = \{\xi \in \mathbb{R} : -1 \le \xi \le 1\}$. This mapping is defined as

$$\chi_e(\xi) = x_e^L \frac{1-\xi}{2} + x_e^R \frac{1+\xi}{2}, \qquad \xi \in \Omega_{st}, \qquad (3.6.52)$$

and its inverse is given by

$$\xi = \chi_e^{-1}(x) = 2\frac{x_e - x_e^L}{x_e^R - x_e^L} - 1, \qquad x_e \in \Omega_e. \qquad (3.6.53)$$

As expansion basis, the Legendre polynomials $L_k(\xi)$ have been chosen, with k the polynomial order, because they are orthogonal with respect to the product (3.6.47). In this way, the solution is expanded on each elemental region Ω_e as

$$\mathbf{U}_e^{\delta}(\chi_e(\xi), t) = \sum_{k=0}^{K} L_k(\xi) \widehat{\mathbf{U}}_e^k(t), \qquad (3.6.54)$$

with $\widehat{\mathbf{U}}_e^k(t)$ the time-varying coefficients of the expansion.
Replacing (3.6.54) in (3.6.51) and letting $\mathbf{\Phi}_e^{\delta} = \mathbf{U}_e^{\delta}$, $2K$ differential equations have been chosen to be solved for each $\Omega_e, e = 1, ..., N_{el}$:

$$\frac{d\widehat{U_{i,e}^k}}{dt} = \mathcal{F}(\mathbf{U}_e^{\delta}), \quad k = 0, ..., K, \ i = 1, 2, \qquad (3.6.55)$$

where $\widehat{U_{i,e}^k}, i = 1, 2$, are each of the two components of $\widehat{\mathbf{U}}_e^k(t)$ and

$$\mathcal{F}(\mathbf{U}_e^{\delta}) = -\left(\frac{\partial F_i}{\partial x}, L_k \right)_{\Omega_e} - \frac{2}{x_e^R - x_e^L} [L_k * (F_i^u - F_i(\mathbf{U}_e^{\delta}))]_{x_e^L}^{x_e^R} +$$

$$+ (S_i(\mathbf{U}_e^{\delta}), L_k)_{\Omega_e}.$$

The method is completed with a second-order Adams-Bashforth time-integration scheme[3]

$$\left(\widehat{U_{i,e}^k}\right)^{n+1} = \left(\widehat{U_{i,e}^k}\right)^n + \frac{3\Delta t}{2}\mathcal{F}\left((\mathbf{U}_e^\delta)^n\right) - \frac{\Delta t}{2}\mathcal{F}\left((\mathbf{U}_e^\delta)^{n-1}\right),$$
$$k = 0, ..., K, \quad i = 1, 2, \quad e = 1, ..., N_{el}, \tag{3.6.56}$$

in which Δt is the time step and n the number of every time step. To calculate the integrals a Gauss quadrature formula[4] of order $q \geq K + 1$ is used.

3.6.1   The Riemann problem

The upwinded fluxes $\mathbf{F}^u$, required in the equation (3.6.56) at the interfaces of each elemental region Ω_e, are calculate through the solution of a Riemann problem which considers the characteristic information arriving at both sides of interfaces and ignores the characteristic information moving away. At time t, each interface separates two states, (A_L, U_L) and (A_R, U_R) (Figure 3.5), with corresponding β and A_0. These states are identified at the final point of the elemental region on the left and at the initial point of the elemental region on the right.

---

[3]The Adam-Bashforth method is a multistep method for the solution of ordinary differential equations $y'(x) = f(x, y)$. In this case a two-step method is considered which permits to compute the n-th approximation of the solution, y_n, through

$$y_n = y_{n-1} + \frac{h}{2}\left[3f_{n-1} - f_{n-2}\right].$$

[4]In numerical analysis the Gauss quadrature formulas are quadrature formulas with the highest degree of precision, using to approximate integrals like $\int_a^b f(x)dx$, knowing $n + 1$ values of the function f in the interval $[a, b]$.
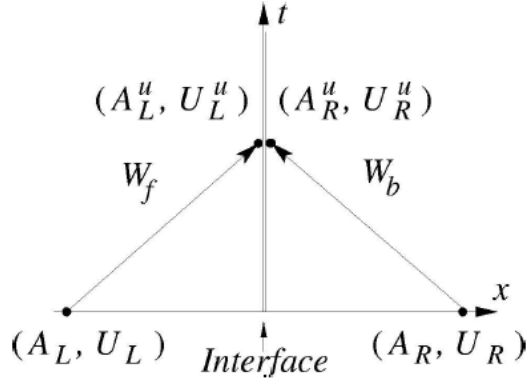
Figure 3.5 Layout of the Riemann problem, which calculates the upwinded states (A_L^u, U_L^u) and (A_R^u, U_R^u), which are originated by the discontinuities between the two initial states (A_L, U_L) and (A_R, U_R).

If there are discontinuities in β and A_0 through the interface, the equation (3.3.19) can not be applied, since there is a discontinuity in the characteristic information which propagates across the interface. So, the two forward state (A_L^u, U_L^u) and (A_R^u, U_R^u) have origin on each side of the interface at the time $t + \Delta t$. Two of the four equations required to determinate these states connect the characteristic information which arrives at the interface from two constant states at the time t. Assuming that the flow is not viscous between the two initial states, in Figure 3.5, there is $\frac{d\mathbf{W}}{dt} = 0$ between each initial constant state and its corresponding upwinded state, according to (3.3.19), and so,

$$W_f\left(A_L, U_L\right) = W_f\left(A_L^u, U_L^u\right), \qquad (3.6.57)$$

$$W_b\left(A_R, U_R\right) = W_b\left(A_R^u, U_R^u\right), \qquad (3.6.58)$$

with W_f and W_b determined by (3.3.22) and (3.3.23).
The remaining equations follow the mass conservation and continuity of the total pressure on the interface,

$$A_L^u U_L^u = A_R^u U_R^u, \qquad (3.6.59)$$

$$\rho\frac{(U_L^u)^2}{2} + p\left(A_L^u\right) = \rho\frac{(U_R^u)^2}{2} + p\left(A_R^u\right), \qquad (3.6.60)$$

with $p(A)$ expressed by the pressure-area relation (3.2.11).

The equations from (3.6.57) to (3.6.60) are solved using the iterative method of Newton-Raphson[5], in order to obtain (A_L^u, U_L^u) and (A_R^u, U_R^u).

The upwinded fluxes at each side of the interface, $\mathbf{F}_L^u$ and $\mathbf{F}_R^u$, are computed as $\mathbf{F}_L^u = \mathbf{F}\left(A_L^u, U_L^u\right)$ and $\mathbf{F}_R^u = \mathbf{F}\left(A_R^u, U_R^u\right)$.

The characteristic information, which moves away from both sides of the interface, does not change the solution, especially if this information has not enough time to interact with the characteristic one which propagates from the neighbourhood quadrature points. So, Δt must be limited by

$$\Delta t \max\left(|U \pm c|\right) \leq \frac{1}{2}\Delta x, \qquad (3.6.61)$$

where Δx is the distance between two consecutive quadrature points.

If β and A_0 have the same value on both sides of the interface, then $\frac{d\mathbf{W}}{dt} = 0$ is applied through the interface, according to (3.3.19). So

$$W_f\left(A_L, U_L\right) = W_f\left(A_R^u, U_R^u\right), \quad W_b\left(A_R, U_R\right) = W_b\left(A_L^u, U_L^u\right),$$

---

[5]The Newton-Raphson method is one of the methods for finding the approximate solution of an equation of the type $f(x) = 0$. It can be applied after having determined an interval $[a, b]$ which contains one root of the equation, and it consists in substituting the curve $y = f(x)$ with the tangent at the curve, starting from any point (for simplicity it is possible to start from one of the two points which have as abscissa the extremes of the interval $[a, b]$ and it assumes, as approximated value of the root, the abscissa x_t given by the intersection of the axis x with the tangent, inside the interval $[a, b]$).

For hypothesis the function and its first and second derivative exist in the interval $[a, b]$, are continuous and not null. The following iterative and recursive relation :

$$x_{n+1} = x_n - \frac{f(x_n)}{f'(x_n)},$$

permits to find consecutive approximations of the root of the equation $y = f(x) = 0$. With the given hypothesis it is proved that the sequence of x_n converges to the root quite rapidly.

which combined with (3.6.57) and (3.6.58) leads to

$$A_L^u = A_R^u, \quad U_L^u = U_R^u,$$

that is the status is the same (A^u, U^u) on both sides of the interface. A combination of the equations (3.6.57) and (3.6.58) provides

$$A^u = \left[\frac{W_f\left(A_L, U_L\right) - W_b\left(A_R, U_R\right)}{8} \sqrt{\frac{2\rho A_0}{\beta}} + A_0^{1/4} \right]^4, \quad (3.6.62)$$

$$U^u = \frac{W_f\left(A_L, U_L\right) + W_b\left(A_R, U_R\right)}{2}. \quad (3.6.63)$$

The fluxes $\mathbf{F}^u$ of the elemental region at the inlet (Ω_1) and the outlet $(\Omega_{N_{el}})$ of each arterial domain Ω are computed by solving the Riemann problem which includes appropriate boundary conditions that will be discussed in the following.

3.6.2 Application to the linear formulation

The algorithm described in the paragraph 3.6.1 can be applied to solve the linear system of the governing equations (3.5.40), considering:

$$\mathbf{U} = \mathbf{\Delta U} = \left[\begin{array}{c} \Delta a \\ \Delta u \end{array} \right], \qquad \mathbf{F} = \mathbf{F}_0\left(\mathbf{\Delta U}\right) = \left[\begin{array}{c} A_0 \Delta u \\ \frac{\beta}{2\rho A_0^{3/2}} \Delta a \end{array} \right],$$

$$\mathbf{S} = \mathbf{S}_0\left(\mathbf{\Delta U}\right) = \left[\begin{array}{c} 0 \\ \frac{1}{\rho}\left(\frac{f_0}{A_0} - \frac{\partial \Delta p}{\partial \beta}\frac{d\beta}{dx} - \frac{\partial \Delta p}{\partial A_0}\frac{dA_0}{dx} \right) \end{array} \right].$$

In the linear version of the Riemann problem just presented, the state on the left elemental region is denoted as $(\Delta a_L, \Delta u_L)$, while the one on the right elemental region as $(\Delta a_R, \Delta u_R)$, and the corresponding updated states as $(\delta a_L, \delta u_L)$ and $(\delta a_R, \delta u_R)$, respectively. As it has been shown for the non-linear formulation, if β and A_0 are the same on both sides of the interface, the flow between the two initial states is not viscous, so $\delta a_L = \delta a_R$ and $\delta u_L = \delta u_R$.

So, a single state is obtained, denoted by $(\delta a, \delta u)$. Combining the linear characteristic information which arrives at the interface as

$$\Delta W_f\left(\Delta a_L, \Delta u_L\right) = \Delta W_f\left(\delta a, \delta u\right), \qquad (3.6.64)$$

$$\Delta W_b\left(\Delta a_R, \Delta u_R\right) = \Delta W_b\left(\delta a, \delta u\right), \qquad (3.6.65)$$

with ΔW_f and ΔW_b determined by (3.5.42) and (3.5.43),

$$\delta a = \frac{A_0\left(\Delta W_f\left(\Delta a_L, \Delta u_L\right) - \Delta W_b\left(\Delta a_R, \Delta u_R\right)\right)}{2c_0}, \qquad (3.6.66)$$

$$\delta u = \frac{\Delta W_f\left(\Delta a_L, \Delta u_L\right) + \Delta W_b\left(\Delta a_R, \Delta u_R\right)}{2}, \qquad (3.6.67)$$

are get. In the paragraph 3.7.2 how obtain an analytical solution to the Riemann problem when β and A_0 are different on both sides of the interface will be shown.

3.7 Boundary conditions

Boundary conditions inside and outside an arterial domain can be classified in three types, depending on the location in the network of arteries. There is an inflow condition (paragraph 3.7.1) if the artery receives an inflow from the outside of the network, a junction boundary condition (paragraph 3.7.2) if the artery is part of a bifurcation with other vascular segments, and a terminal boundary condition (paragraph 3.7.3) if it is coupled with lumped parameters. Each case is analyzed in the following for both linear and non-linear formulation.

3.7.1 Inflow boundary conditions

The 1-D model permits to prescribe a time-dependent section $A_{bc}(t)$, velocity $U_{bc}(t)$, or flow rate $Q_{bc}(t)$. The other variables which define the flow are computed through the Riemann problem previously described.

One of the two states separated by the interface $((A_L, U_L)$ or

(A_R, U_R) in Figure 3.5) belongs to the inlet (Ω_1) or to the outlet $(\Omega_{N_{el}})$ of the arterial domain, and the other to a virtual region outside the arterial domain. It is assumed that the virtual region has the same β and A_0 of the adjacent states in Ω_1 or $\Omega_{N_{el}}$, so that a single forward state (A^u, U^u) is obtained by the solution of the equations (3.6.62) and (3.6.63). To define the desired inflow boundary condition, it is necessary to determine the state in the virtual region which provides $A^u = A_{bc}$, $U^u = U_{bc}$ or $A^u U^u = Q_{bc}$ when it is combined with the state at the inlet or the outlet of the arterial domain.

To prescribe $A_{bc}(t)$ at the inlet of the arterial domain, $U_L = U_R$ is assumed. Then, the equation (3.6.62) becomes

$$2\left(A^u\right)^{1/4} = \left(A_L\right)^{1/4} + \left(A_R\right)^{1/4},$$

by which the value of A_L is found, which satisfies $A^u = A_{bc}$ at the next time step,

$$A_L = \left(2\left(A_{bc}\right)^{1/4} - \left(A_R\right)^{1/4}\right)^4. \tag{3.7.68}$$

To prescribe $U_{bc}(t)$ at the inlet of the arterial domain, $A_L = A_R$ is assumed, which leads to $2U^u = U_L + U_R$, according to (3.6.63). So, to obtain the desired U^u at the next time step,

$$U_L = 2U_{bc} - U_R, \tag{3.7.69}$$

is enforced. To describe $Q_{bc}(t)$, the equation (3.7.69) is rewritten in this way:

$$U_L = 2\frac{Q_{bc}}{A_R} - U_R. \tag{3.7.70}$$

Following the same procedure, to define inflow conditions at the outlet of the arterial domain,

$$A_R = \left(2\left(A_{bc}\right)^{1/4} - \left(A_L\right)^{1/4}\right)^4, \tag{3.7.71}$$

$$U_R = 2U_{bc} - U_L, \tag{3.7.72}$$

$$U_R = 2\frac{Q_{bc}}{A_L} - U_L, \tag{3.7.73}$$

are enforced.

As inflow conditions it is also possible to use a valve model, which mimics the real behavior of the physiological system. The aortic valve is one of the two semilunar valves of the heart and lies between the left ventricle and the aorta. It permits the flow of the blood from the left ventricle of the heart to the aorta. During ventricular systole, pressure rises in the left ventricle. When the pressure in the left ventricle rises above the pressure in the aorta, the aortic valve opens, allowing blood to exit the left ventricle into the aorta. When ventricular systole ends, pressure in the left ventricle rapidly drops. When the pressure in the left ventricle decreases below the aortic pressure, the aortic valve closes, and remains closed until the next heart beat. The opening and closing of valve is determined by the pressure difference between the left ventricle (p_{LV}) and the aortic pressure. More specifically, the valve opens when

$$p(0,t) \leq p_{LV}(t),$$

in which case the pressure at the inflow gets prescribed

$$p(0,t) = p_{LV}(t),$$

and it closes when the velocity becomes negative, in which case the velocity at the inflow is prescribed to be zero:

$$u(0,t) = 0.$$

$$u(0,t) = 0, \quad \text{if } p_{LV}(t) < p(0,t)$$

$$p(0,t) = p_{LV}(t), \quad \text{if } u(0,t) > 0.$$
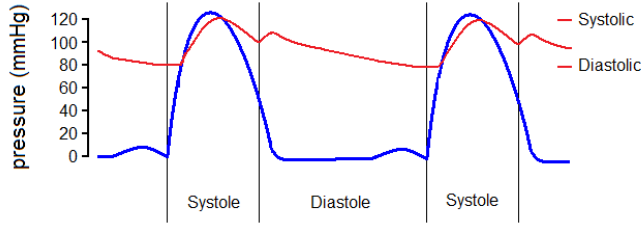
Figure 3.6 Aortic pressure (red) and left ventricular pressure (blue) during systole and diastole.

Since the equation (3.6.67) has the same shape of the equation (3.6.63), the equations (3.7.69), (3.7.70), (3.7.72) and (3.7.73) are valid for the linear formulation too, with $(A_L, U_L) = (\Delta a_L + A_{0_L}, \Delta u_L)$ and $(A_R, U_R) = (\Delta a_R + A_{0_R}, \Delta u_R)$. However, to prescribe $A_{bc}(t)$ in the linear theory it is necessary to use the equation (3.6.66) with $\Delta u_L = \Delta u_R$, which holds to $2\delta a = \Delta a_L + \Delta a_R$. So, at the inlet of the arterial domain it is necessary to define

$$\Delta a_L = 2\left(A_{bc} - A_{0_R}\right) - \Delta a_R, \qquad (3.7.74)$$

and at the outlet

$$\Delta a_R = 2\left(A_{bc} - A_{0_L}\right) - \Delta a_L. \qquad (3.7.75)$$

3.7.2 Boundary conditions at junctions

In this paragraph how to determine the upwinded states at the boundary of the arterial domain that is connected to another arterial domain or it is a part of a junction, will be detailed. Both the problems will be analyzed analytically for linear and non-linear formulation.

Connection of two arteries

To calculate the upwinded states in the two involved elemental regions, in the connection of two arterial domains, it is necessary to solve the Riemann problem described previously, whose layout is showed in figure 3.5. The initial state at the final point of the

elemental region at the outlet of an arterial domain is (A_L, U_L), while (A_R, U_R) is the initial state at the initial point of the initial elemental region at the inlet of the arterial domain. The corresponding upwinded states, (A_L^u, U_L^u) and (A_R^u, U_R^u), are determined through the numerical solution of the equations (3.6.57)-(3.6.60).

Linear analysis of a connection of two arteries

For the linear formulation the upwinded states involved in the connection of two arterial domains, or in two adjacent elemental regions in the same arterial domain, can be computed, but with different values of β and A_0. Since $\Delta u \ll c_0$ in physiological conditions, each perturbation $(\Delta a, \Delta p, \Delta u)$ at the initial state $(A, p, U) = (A_0, 0, 0)$ at the point (of each elemental region) close to the connection, produces an upwinded state on the left of the connection, denoted by $(A_{0_L} + \delta a_L, \delta p_L, \delta u_L)$, and an upwinded state on the right, denoted by $(A_{0_R} + \delta a_R, \delta p_R, \delta u_R)$. Following the same procedure of the non-linear version of the problem, the first two equations to satisfy connect the linear characteristic variables (3.5.42) and (3.5.43), which leads to the connection as

$$\delta u_L + \frac{c_{0_L}}{A_{0_L}} \delta a_L = \Delta u_L + \frac{c_{0_L}}{A_{0_L}} \Delta a_L, \qquad (3.7.76)$$

$$\delta u_R + \frac{c_{0_R}}{A_{0_R}} \delta a_R = \Delta u_R + \frac{c_{0_R}}{A_{0_R}} \Delta a_R. \qquad (3.7.77)$$

The mass conservation and the continuity of the pressure provide other two equations to satisfy. Ignoring second order terms, they are like

$$A_{0_L} \delta u_L = A_{0_R} \delta u_R, \qquad (3.7.78)$$

$$\delta p_L = \delta p_R. \qquad (3.7.79)$$

If the state on the left elemental region is perturbed with $(\Delta a_L, \Delta p_L, \Delta u_L)$ and $\Delta a_R = \Delta p_R = \Delta u_R = 0$ in the right elemental region, the relations (3.7.76) and (3.7.77) are reduced to

$$\delta u_L = \Delta u_L + \frac{c_{0_L}}{A_{0_L}} \left(\Delta a_L - \delta a_L \right), \qquad (3.7.80)$$

$$\delta u_R = \frac{c_{0_R}}{A_{0_R}} \delta a_R. \tag{3.7.81}$$

Replacing (3.7.80) and (3.7.81) in (3.7.78), and expressing area variations in terms of pressure variations through (3.5.41),

$$A_{0_L} \left(\Delta u_L + \frac{1}{\rho c_{0_L}} \left(\Delta p_L - \delta p_L \right) \right) = \frac{A_{0_R}}{\rho c_{0_R}} \delta p_R, \tag{3.7.82}$$

is obtained, putting (3.7.79) inside (3.7.82) and reordering the terms

$$\delta p_L = \delta p_R \equiv \delta p = R_L \left(\Delta p_L + \rho c_{0_L} \Delta u_L \right), \tag{3.7.83}$$

with

$$R_L = \frac{\frac{A_{0_L}}{c_{0_L}}}{\frac{A_{0_L}}{c_{0_L}} + \frac{A_{0_R}}{c_{0_R}}}.$$

Similarly, if the state on the right elemental region is perturbed with $(\Delta a_R, \Delta p_R, \Delta u_R)$ and $\Delta a_L = \Delta p_L = \Delta u_L = 0$ on the left elemental region,

$$\delta p_L = \delta p_R \equiv \delta p = R_R \left(\Delta p_R - \rho c_{0_R} \Delta u_R \right), \tag{3.7.84}$$

is obtained, with

$$R_R = \frac{\frac{A_{0_R}}{c_{0_R}}}{\frac{A_{0_L}}{c_{0_L}} + \frac{A_{0_R}}{c_{0_R}}}.$$

Because of the linearity of the problem, if both perturbations happen in the same time interval $(\Delta a_L, \Delta p_L, \Delta u_L)$ and $(\Delta a_R, \Delta p_R, \Delta u_R)$, the results (3.7.83) and (3.7.84) are combined, obtaining

$$\delta p_L = \delta p_R \equiv \delta p = R_L \left(\Delta p_L + \rho c_{0_L} \Delta u_L \right) + R_R \left(\Delta p_R + \rho c_{0_R} \Delta u_R \right). \tag{3.7.85}$$

The final perturbed areas δa_L and δa_R are determined through (3.5.41) as

$$\delta a_L = \frac{A_{0_L}}{\rho \left(c_{0_L} \right)^2} \delta p, \qquad \delta a_R = \frac{A_{0_R}}{\rho \left(c_{0_R} \right)^2} \delta p, \tag{3.7.86}$$

and the final perturbed velocities δu_L and δu_R are given by (3.7.76) and (3.7.77), once that δa_L and δa_R have been determined.

From the equations (3.7.86) it is possible to observe that, if $c_{0_L} = c_{0_R}$ and $A_{0_L} = A_{0_R}$, then $\delta a_L = \delta a_R$, and so, for (3.7.78) results $\delta u_L = \delta u_R$.

Junctions

Two type of junctions have been considered:

- junctions of type 1×2 (Figure 3.7, left), where the outlet of the parent vessel is connected to the inlet of two daughter vessels;

- junctions of type 2×1 (Figure 3.7, right), where the inlet of the parent vessel is connected to the outlet of two daughter vessels.

The first ones are the most common arrangement in big human systemic arteries. The second ones are more rare in big arteries, but occur more frequently in peripheral systemic arteries (such as the circle of Willis and the palmar arch), in arterioles and capillaries, are the most common type of junctions in the venous system and are very important for simulations of surgical interventions such as an arterial bypass.
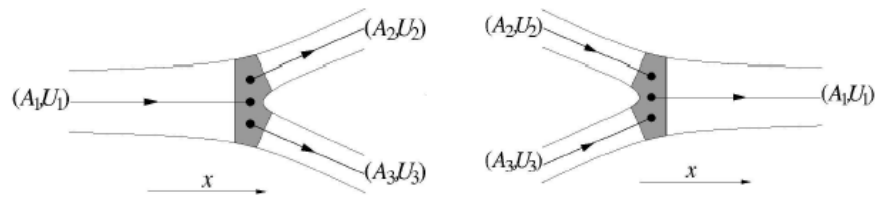
Figure 3.7 Types of junctions: 1×2 (left) e 2×1 (right). The arrows indicates the pisitive direction of the blood flow.

If (A_1, p_1, U_1), (A_2, p_2, U_2) and (A_3, p_3, U_3) are the initial states at the points adjacent to the junctions of each elemental region

1×2 (Figure 3.7, left), then their corresponding upwinded states (A_i^u, p_i^u, U_i^u) $(i = 1, 2, 3)$ are determined by the resolution of the non-linear system of six algebraic equations, using the Newton-Raphson method. Assuming the flow to be constant in the points close to the junction, there is

$$W_f\left(A_1^u, U_1^u\right) = W_f\left(A_1, U_1\right), \tag{3.7.87}$$

$$W_b\left(A_2^u, U_2^u\right) = W_b\left(A_2, U_2\right), \tag{3.7.88}$$

$$W_b\left(A_3^u, U_3^u\right) = W_b\left(A_3, U_3\right), \tag{3.7.89}$$

with W_f and W_b determined by (3.3.22) and by (3.3.23). The mass conservation applied to the upwinded variables provides

$$A_1^u U_1^u = A_2^u U_2^u + A_3^u U_3^u. \tag{3.7.90}$$

The Bernoulli's law [6] provides the last two equations

$$p\left(A_1^u\right) + \frac{1}{2}\rho\left(U_1^u\right)^2 = p\left(A_2^u\right) + \frac{1}{2}\rho\left(U_2^u\right)^2, \tag{3.7.91}$$

$$p\left(A_1^u\right) + \frac{1}{2}\rho\left(U_1^u\right)^2 = p\left(A_3^u\right) + \frac{1}{2}\rho\left(U_3^u\right)^2, \tag{3.7.92}$$

with $p(A)$ expressed by the tube law (3.2.11). It is possible to observe that the Bernoulli's law is just an approximation of the balance of the energy inside the junction, since the separation of the flow and the formation of a vortex are possible only in the neighbourhood of the junction, because of the discontinuous variations of the area in it.

In the case of a 2×1 junction, with initial states (A_1, p_1, U_1), (A_2, p_2, U_2) and (A_3, p_3, U_3) (Figure 3.7, right), their corresponding upwinded states (A_i^u, p_i^u, U_i^u) $(i = 1, 2, 3)$ are determined by

---

[6]The Bernoulli's law is $p + \rho\frac{v^2}{2} + \rho g h = cost$ in which:
v is the velocity of the fluid along the flow line,
g is the acceleration of gravity,
h is the altrimetrical quota (that is the high with respect to an horizontal reference, of any point inside the pipe),
p represents the static pressure along a line of flow,
ρ is the density of the fluid.

the solution of the following six non-linear equations. The conservation of the characteristic variables, moving toward the junction, leads to

$$W_b\left(A_1^u, U_1^u\right) = W_b\left(A_1, U_1\right),\qquad(3.7.93)$$

$$W_f\left(A_2^u, U_2^u\right) = W_f\left(A_2, U_2\right),\qquad(3.7.94)$$

$$W_f\left(A_3^u, U_3^u\right) = W_f\left(A_3, U_3\right).\qquad(3.7.95)$$

Mass conservation and Bernoulli's law are imposed too, using the equations from (3.7.90) to (3.7.92).

Linear analysis of junctions

In this paragraph the upwinded states of the three elemental regions involved in a junction 1×2 or 2×1 are determined. Following the same procedure of the linear study of a connection of two arteries, each perturbation $(\Delta a, \Delta p, \Delta u)$ in the initial state $(A, p, u) = (A_0, 0, 0)$, in each of the three points adjacent to the junction, provides two upwinded stated denoted by $(A_{0_i} + \delta a_i, \delta p_i, \delta u_i)$ $(i = 1, 2, 3)$. In the case of a flow junction 1×2, the following relation between the linear characteristic variables (3.5.42) and (3.5.43) moving through the junction is verified:

$$\delta u_1 + \frac{c_{0_1}}{A_{0_1}}\delta a_1 = \Delta u_1 + \frac{c_{0_1}}{A_{0_1}}\Delta a_1,\qquad(3.7.96)$$

$$\delta u_2 + \frac{c_{0_2}}{A_{0_2}}\delta a_2 = \Delta u_2 + \frac{c_{0_2}}{A_{0_2}}\Delta a_2,\qquad(3.7.97)$$

$$\delta u_3 + \frac{c_{0_3}}{A_{0_3}}\delta a_3 = \Delta u_3 + \frac{c_{0_3}}{A_{0_3}}\Delta a_3.\qquad(3.7.98)$$

Mass conservation and the continuity of the total pressure are applied, ignoring the second order terms. They are like

$$A_{0_1}\delta u_1 = A_{0_2}\delta u_2 + A_{0_3}\delta u_3,\qquad(3.7.99)$$

$$\delta p_1 = \delta p_2,\qquad(3.7.100)$$

$$\delta p_1 = \delta p_3.\qquad(3.7.101)$$

If the state $(A_{0_1}, 0, 0)$ is perturbed with $(\Delta a_1, \Delta p_1, \Delta u_1)$ at the final point of the parent vessel and $\Delta a_j = \Delta p_j = \Delta u_j = 0$ $(j = 2, 3)$, the relations (3.7.96)-(3.7.98) are reduced to

$$\delta u_1 = \Delta u_1 + \frac{c_{0_1}}{A_{0_1}} \left(\Delta a_1 - \delta a_1 \right), \tag{3.7.102}$$

$$\delta u_2 = \frac{c_{0_2}}{A_{0_2}} \delta a_2, \tag{3.7.103}$$

$$\delta u_3 = \frac{c_{0_3}}{A_{0_3}} \delta a_3. \tag{3.7.104}$$

Replacing (3.7.102)-(3.7.104) in (3.7.99), and expressing area variations in terms of pressure variations through (3.5.41), there is

$$A_{0_1} \left(\Delta u_1 + \frac{1}{\rho c_{0_1}} \left(\Delta p_1 - \delta p_1 \right) \right) = \frac{A_{0_2}}{\rho c_{0_2}} \delta p_2 + \frac{A_{0_3}}{\rho c_{0_3}} \delta p_3. \tag{3.7.105}$$

Taking into account (3.7.100) and (3.7.101) and reordering the terms, the equation (3.7.105) provides

$$\delta p_1 = \delta p_2 = \delta p_3 \equiv \delta p = R_1 \left(\Delta p_1 + \rho c_{0_1} \Delta u_1 \right), \tag{3.7.106}$$

where

$$R_1 = \frac{\frac{A_{0_1}}{c_{0_1}}}{\frac{A_{0_1}}{c_{0_1}} + \frac{A_{0_2}}{c_{0_2}} + \frac{A_{0_3}}{c_{0_3}}}.$$

Similarly, if the state $\left(A_{0_j}, 0, 0 \right)$ is perturbed with $(\Delta a_j, \Delta p_j, \Delta u_j)$ $(j = 2, 3)$ at the initial point of both daughter vessels and $\Delta a_i = \Delta p_i = \Delta u_i = 0$ for each $i \neq j$,

$$\delta p_1 = \delta p_2 = \delta p_3 \equiv \delta p = R_j \left(\Delta p_j - \rho c_{0_j} \Delta u_j \right), \tag{3.7.107}$$

is obtained, with

$$R_2 = \frac{\frac{A_{0_2}}{c_{0_2}}}{\frac{A_{0_1}}{c_{0_1}} + \frac{A_{0_2}}{c_{0_2}} + \frac{A_{0_3}}{c_{0_3}}}, \qquad R_3 = \frac{\frac{A_{0_3}}{c_{0_3}}}{\frac{A_{0_1}}{c_{0_1}} + \frac{A_{0_2}}{c_{0_2}} + \frac{A_{0_3}}{c_{0_3}}}.$$

Because of the linearity of the problem, when three perturbations in the same time interval are considered, combining the equations (3.7.106) and (3.7.107),

$$\delta p_1 = \delta p_2 = \delta p_3 \equiv \delta p = R_1 \left(\Delta p_1 + \rho c_{0_1} \Delta u_1 \right) +$$
$$+ R_2 \left(\Delta p_2 - \rho c_{0_2} \Delta u_2 \right) + R_3 \left(\Delta p_3 - \rho c_{0_3} \Delta u_3 \right), \qquad (3.7.108)$$

is obtained. The perturbed area follow from (3.5.41), and they assume the following form

$$\delta a_1 = \frac{A_{0_1}}{\rho \left(c_{0_1} \right)^2} \delta p, \qquad \delta a_2 = \frac{A_{0_2}}{\rho \left(c_{0_2} \right)^2} \delta p, \qquad \delta a_3 = \frac{A_{0_3}}{\rho \left(c_{0_3} \right)^2} \delta p,$$
$$(3.7.109)$$

while the final perturbed velocity came from the relations (3.7.96)-(3.7.98), once that δa_1, δa_2 and δa_3 are determined.

When a 2×1 junction is perturbed with $(\Delta a_i, \Delta p_i, \Delta u_i)$ $(i = 1, 2, 3)$ in the same time interval,

$$\delta p_1 = \delta p_2 = \delta p_3 \equiv \delta p = R_1 \left(\Delta p_1 - \rho c_{0_1} \Delta u_1 \right) +$$
$$R_2 \left(\Delta p_2 + \rho c_{0_2} \Delta u_2 \right) + R_3 \left(\Delta p_3 + \rho c_{0_3} \Delta u_3 \right), \qquad (3.7.110)$$

are get. The relations (3.7.109) provide perturbed area, while perturbed velocities are given by the analogous equations (3.7.96)-(3.7.98).

If a perturbation $(\Delta a_1, \Delta p_1, \Delta u_1)$ at the final point of a parent artery of a junction 1×2 consists only in a forward wave, then W_b has the same value assumed at the initial state $(A_1, p_1, U_1) = (A_{0_1}, 0, 0)$ along the backward characteristic line. Therefore $\Delta W_b = 0$, and so $\Delta u_1 = \frac{c_{0_1}}{A_{0_1}} \Delta a_1 = \frac{1}{\rho c_{0_1}} \Delta p_1$, according to the equations (3.5.41) and (3.5.43). Consequently, the equation (3.7.106) is reduced to $\delta p_1 = 2 R_1 \Delta p_1$. If the reflection coefficient

$$R_{f_1} \equiv \frac{\delta p_1 - \Delta p_1}{\Delta p_1},$$

is defined, as suggested by Sherwin [37] (inspired by problems of acoustics and waves of surface),

$$R_{f_1} = \frac{\frac{A_{0_1}}{c_{0_1}} - \frac{A_{0_2}}{c_{0_2}} - \frac{A_{0_3}}{c_{0_3}}}{\frac{A_{0_1}}{c_{0_1}} + \frac{A_{0_2}}{c_{0_2}} + \frac{A_{0_3}}{c_{0_3}}}, \qquad (3.7.111)$$

is obtained. At the same way, if the perturbation $(\Delta a_j, \Delta p_j, \Delta u_j)$ $(j = 2, 3)$ acts at the state of both daughter vessels, at the point adjacent to the junction 1×2, and it consists of only one backward wave, then W_f has the same value assumed by the initial state $(A_j, p_j, U_j) = (A_{0_j}, 0, 0)$ along the forward characteristic line. Therefore $\Delta W_f = 0$, and so $\Delta u_j = -\frac{c_{0_j}}{A_{0_j}} \Delta a_j = -\frac{1}{\rho c_{0_j}} \Delta p_j$, according to the equations (3.5.41) and (3.5.42). Consequently, the equation (3.7.107) is reduced to $\delta p_j = 2R_j \Delta p_j$, and, defining the reflection coefficient $R_{f_j} \equiv \frac{\delta p_j - \Delta p_j}{\Delta p_j}$,

$$R_{f_2} = \frac{-\frac{A_{0_1}}{c_{0_1}} + \frac{A_{0_2}}{c_{0_2}} - \frac{A_{0_3}}{c_{0_3}}}{\frac{A_{0_1}}{c_{0_1}} + \frac{A_{0_2}}{c_{0_2}} + \frac{A_{0_3}}{c_{0_3}}}, \qquad R_{f_3} = \frac{-\frac{A_{0_1}}{c_{0_1}} - \frac{A_{0_2}}{c_{0_2}} + \frac{A_{0_3}}{c_{0_3}}}{\frac{A_{0_1}}{c_{0_1}} + \frac{A_{0_2}}{c_{0_2}} + \frac{A_{0_3}}{c_{0_3}}},$$
$$(3.7.112)$$

are obtained. Combining the three perturbations which satisfy $\Delta u_1 = \frac{c_{0_1}}{A_{0_1}} \Delta a_1$, $\Delta u_2 = -\frac{c_{0_2}}{A_{0_2}} \Delta a_2$ and $\Delta u_3 = -\frac{c_{0_3}}{A_{0_3}} \Delta a_3$ in a splitting flow bifurcation

$$\delta p_1 = \delta p_2 = \delta p_3 \equiv \delta p = (1 + R_{f_1}) \Delta p_1 +$$
$$+ (1 + R_{f_2}) \Delta p_2 + (1 + R_{f_3}) \Delta p_3, \qquad (3.7.113)$$

is get. This latest equation can be applied to a 2×1 junction too, in which the three perturbations satisfy $\Delta u_1 = -\frac{c_{0_1}}{A_{0_1}} \Delta a_1$, $\Delta u_2 = \frac{c_{0_2}}{A_{0_2}} \Delta a_2$ and $\Delta u_3 = \frac{c_{0_3}}{A_{0_3}} \Delta a_3$.

3.7.3 Boundary terminal conditions

In the next paragraph, the 0-D equations, which govern models with lumped parameters, will be described and used to study the effect of pulse wave propagation on the wall compliance and the fluid resistance and inertia of the small arteries, arterioles and capillaries. These are applied to solve the classic windkessel model with two elements (proposed by Hales and Franck). How to couple different types of models with lumped parameters with 1-D and non-linear formulation will be described, using the Riemann problem already presented. The initial state (A_L, U_L) is put at

the final point of the 1-D arterial domain, while the initial state (A_R, U_R) is chosen to produce an upwinded state (A^u, U^u), which satisfies the relation between A^u and U^u defined by the used model with lumped parameters. The values of β and A_0 in (A_R, U_R) are assumed to be equal to their homologous in (A_L, U_L).

Zero-dimensional equations

The linear 1-D system of governing equations (3.5.40) can be reduced to

$$\begin{cases} \frac{\partial \Delta a}{\partial t} + A_0 \frac{\partial \Delta u}{\partial x} = 0, \\ \frac{\partial \Delta u}{\partial t} + \frac{1}{\rho} \frac{\partial \Delta p}{\partial x} = -\frac{8\pi\mu\Delta u}{\rho A_0}, \end{cases} \qquad (3.7.114)$$

assuming β and A_0 constant along the arterial domain and the friction term is given by the Poiseuille's flow ($\gamma = 2$ in the generic velocity profile (3.2.4), that in small arteries gives a better approximation respect to the more flat velocity profile in larger arteries). The system (3.7.114) can be written in terms of the increment in flow rate, $\Delta q = A_0 \Delta u$, and of the pressure, Δp, as

$$\begin{cases} \frac{A_0}{\rho(c_0)^2} \frac{\partial \Delta p}{\partial t} + \frac{\partial \Delta q}{\partial x} = 0, \\ \frac{\partial \Delta q}{\partial t} + \frac{A_0}{\rho} \frac{\partial \Delta p}{\partial x} = -\frac{c\Delta q}{\rho A_0}, \end{cases} \qquad (3.7.115)$$

using the equation (3.5.41). An integration of this last system on the length l of the arterial domain leads to

$$\begin{cases} C\frac{d\widehat{p}}{dt} + Q_{out} - Q_{in} = 0, \\ L\frac{d\widehat{Q}}{dt} + R_\mu\widehat{Q} + p_{out} - p_{in} = 0, \end{cases} \qquad (3.7.116)$$

where $\widehat{p}(t) \equiv \frac{1}{l}\int_0^l \Delta p \; dx$ and $\widehat{Q}(t) \equiv \frac{1}{l}\int_0^l \Delta q \; dx$ are the mean pressure and flow rate on the whole arterial domain,

$$Q_{in} \equiv \Delta q(0, t),$$

$$Q_{out} \equiv \Delta q(l,t),$$

$$p_{in} \equiv \Delta p(0,t),$$

$$p_{out} \equiv \Delta p(l,t),$$

and

$$R_\mu \equiv \frac{8\pi\mu l}{(A_0)^2}, \qquad (3.7.117)$$

$$L \equiv \frac{\rho l}{A_0}, \qquad (3.7.118)$$

$$C \equiv \frac{A_0 l}{\rho (c_0)^2}, \qquad (3.7.119)$$

are, respectively, the resistance to the flow, the inertia in the blood and the compliance of the wall. The value of Q_{in} is given by the 1-D formulation, and p_{out} is a constant parameter in the simulation which represents the venous pressure. Therefore, the system (3.7.116) has four unknowns $(\widehat{p}, \widehat{Q}, Q_{out}$ and $p_{in})$. To delete two of them, $\widehat{p} = p_{in}$ and $\widehat{Q} = Q_{out}$ are assumed, and this leads to a

$$\begin{cases} C\frac{dp_{in}}{dt} + Q_{out} - Q_{in} = 0, \\ L\frac{dQ_{out}}{dt} + R_\mu Q_{out} + p_{out} - p_{in} = 0. \end{cases} \qquad (3.7.120)$$

The just obtained equations are analogous to the electric transmission line equations, in which the role of the flow rate is played by the electric power and the blood pressure corresponds to the electric potential. So, the obtained system can be visualized as the electric circuit showed in Figure 3.8, in which R_μ is the resistance, L the inductance and C the capacitance.
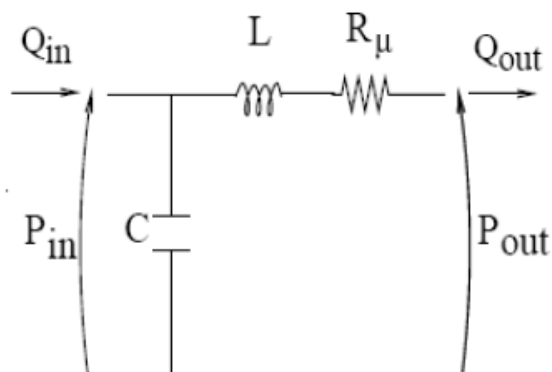
Figure 3.8 Representation of the electric circuit governed by 0-D equations (3.7.120).

The windkessel model

If $L = 0$, the system (3.7.120) becomes

$$\begin{cases} C\frac{dp_{in}}{dt} + Q_{out} - Q_{in} = 0, \\ \quad Q_{out} = \frac{p_{out} - p_{in}}{R_\mu}, \end{cases} \qquad (3.7.121)$$

which leads to the differential equation

$$\frac{dp_{in}}{dt} + \frac{p_{in}}{R_\mu C} = \frac{Q_{in}}{C} + \frac{p_{out}}{R_\mu C}, \qquad (3.7.122)$$

which governs the classic windkessel model described by Hales (Figure 3.9). This model can be used to simulate the all tree of the systemic arteries, if it is considered that $C = C_T$ and $R_\mu = R_{\mu_T}$ are the total compliance and resistance of the system, Q_{in} is the outflow from the left ventricle, Q_{out} is the outflow from the venous system, p_{out} is the pressure at which flow from the arteries to the veins ceases and $p_{in} = p_{wk}$ is an appropriate mean pressure in all the systemic arteries, called *windkessel pressure*.
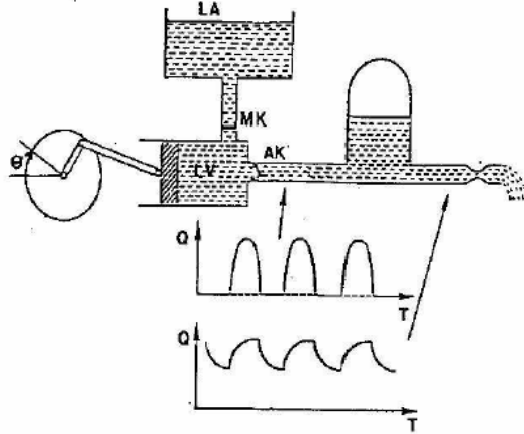
Figure 3.9 Diagram of the *windkessel effect* described by Hales in 1733. The pulse inflow at the aortic valve (AK), caused by the contraction of the left ventricle (LV) while the mitral valve (MK) is close, in transformed into a more regular outflow from the compliance of the arterial system represented by an air chamber. The left atrium (LA) is represented by a water tank. (From the notes published by IBITECH [36]).

The general solution of the equation (3.7.122) with this new notation is

$$p_{wk} - p_{out} = (p_{wk_0} - p_{out}) \, e^{\frac{-t}{R_{\mu T} C_T}} + \frac{1}{C_T} e^{\frac{-t}{R_{\mu T} C_T}} \int_0^t Q_{in}(t') e^{\frac{t'}{R_{\mu T} C_T}} \, dt',$$
(3.7.123)

where p_{wk_0} is the pressure at the moment of the appearance of the ventricular ejection, that is the windkessel pressure once that the aortic valve is close.

During the diastole there is $Q_{in} = 0$ and (3.7.123) is reduced to

$$p_{wk} - p_{out} = (p_{wk_0} - p_{out}) \, e^{\frac{-t}{R_{\mu T} C_T}},$$
(3.7.124)

and Q_{out} becomes

$$Q_{out} = \frac{(p_{wk_0} - p_{out})}{R_{\mu T}} e^{\frac{-t}{R_{\mu T} C_T}}.$$
(3.7.125)

According to Wang [48], the pulse waves are quite minimal during the last two thirds of the diastole. So, during this time, the pressure in the systemic arteries must be approximated with p_{wk}. The compliance of the system has a bigger flow rate during the diastole with the increase of the pressure p_{wk_0}.

An integration of the equation (3.7.122) (using the new notation) on a time interval $[t', t' + T]$

$$\int_{t'}^{t'+T} \frac{dp_{wk}}{dt} dt + \int_{t'}^{t'+T} \frac{p_{wk}}{R_{\mu_T} C_T} dt = \int_{t'}^{t'+T} \frac{Q_{in}}{C_T} dt + \int_{t'}^{t'+T} \frac{p_{out}}{R_{\mu_T} C_T} dt,$$

leads to

$$p_{wk}(t' + T) - p_{wk}(t') = \frac{T}{C_T} \left(\overline{Q}_{in} - \frac{\overline{p}_{wk} - p_{out}}{R_{\mu_T}} \right) =$$

$$= \frac{T}{C_T} \left(\overline{Q}_{in} - \overline{Q}_{out} \right), \qquad (3.7.126)$$

where

$$\overline{p}_{in} \equiv \frac{1}{T} \int_{t'}^{t'+T} p_{wk} dt, \qquad \overline{Q}_{in} \equiv \frac{1}{T} \int_{t'}^{t'+T} Q_{in} dt,$$

and

$$\overline{Q}_{out} \equiv \frac{1}{T} \int_{t'}^{t'+T} Q_{out} dt,$$

are, respectively, the mean pressure and the inflow and outflow rates in the interval $[t', t' + T]$. If p_{wk} is periodic of period T, then $p_{wk}(t' + T) = p_{wk}(t')$ and (3.7.126) is reduced to

$$\overline{Q} = \frac{\overline{p}_{wk} - p_{out}}{R_{\mu_T}}, \qquad (3.7.127)$$

with $\overline{Q} \equiv \overline{Q}_{in} = \overline{Q}_{out}$.

Terminal reflection coefficient

The boundary terminal condition refers to the forward characteristic information, W_f, leaving the outlet of an arterial domain,

with the backward characteristic information W_b, that is reflected by the terminal model through

$$W_b = -R_t W_f,$$

where $-1 \leq R_t \leq 1$ is the *terminal reflection coefficient*. So, the solution of the Riemann problem for the velocity at the terminal outlet, given by the equation (3.6.63), can be written as

$$U^u = \frac{W_f(A_L, U_L)}{2}(1 - R_t). \qquad (3.7.128)$$

Using the equation (3.7.72) with $U_{bc} = U^u$ ($A_R = A_L$ should be assumed), the inlet specific velocity is obtained as

$$U_R = W_f(1 - R_t) - U_L. \qquad (3.7.129)$$

In the linear formulation, this boundary terminal condition is applied through $\Delta u_R = \Delta W_f(1 - R_t) - \Delta u_L$, and, in addition, the following physic interpretation can be given: if the pulse wave which travels toward the terminal model, is a forward wave with pressure Δp_L and velocity Δu_L, then

$$\Delta u_L = \frac{1}{\rho c_{0_L}} \Delta p_L, \qquad (3.7.130)$$

as previously explained (c_{0_L} is the velocity of the pulse wave at the final point of the artery). If the reflected pressure is δp_L and the reflected velocity is δu_L, then

$$\delta u_L - \frac{1}{\rho c_{0_L}} \delta p_L = \Delta W_b = -R_t \Delta W_f = -R_t \left(\Delta u_L + \frac{1}{\rho c_{0_L}} \Delta p_L\right). \qquad (3.7.131)$$

Along the forward characteristic curve, there is

$$\delta u_L - \frac{1}{\rho c_{0_L}} \delta p_L = \Delta u_L + \frac{1}{\rho c_{0_L}} \Delta p_L. \qquad (3.7.132)$$

A combination of the relations (3.7.130)-(3.7.132) provides

$$\delta p_L = \Delta p_L(1 + R_t), \qquad (3.7.133)$$

$$\delta u_L = \Delta u_L \left(1 - R_t\right). \tag{3.7.134}$$

These latest two equations show that $R_t = 1$ represent a blockage or a full reflection of the incoming wave ($\delta p_L = 2\Delta p_L$ and $\delta u_L = 0$), $R_t = 0$ represents a non-reflecting or absorbing inflow ($\delta p_L = \Delta p_L$ and $\delta u_L = \Delta u_L$), and $R_t = -1$ represents an inflow with an open extremity ($\delta p_L = 0$ and $\delta u_L = 2\Delta u_L$).

Terminal resistance

A terminal reflection coefficient can also be considered as a model with lumped parameters composed by a resistance R_μ, as shown in Figure 3.10, (a).
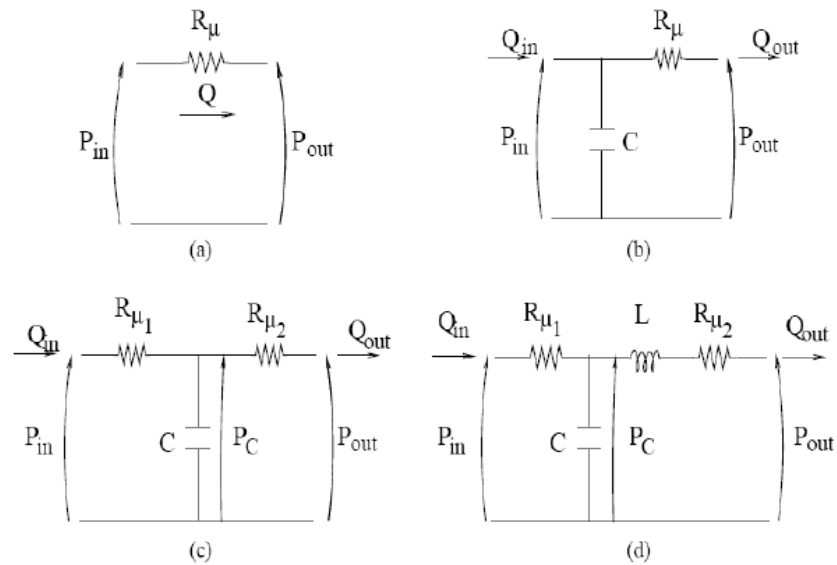
Figure 3.10 Representation of electrical circuits similar to the considered terminal models with lumped parameters: (a) trminal resistance, (b) windkessel model with two elements (RC), (c) windkessel model with three elements (RCR), (d) windkessel model with four elements (RCLR).

Assuming $C = L = 0$, the system (3.7.120) is reduced to

$$\begin{cases} Q_{out} = Q_{in} = Q, \\ R_\mu Q_{out} + p_{out} - p_{in} = 0, \end{cases} \qquad (3.7.135)$$

which leads to

$$Q = \frac{p_{in} - p_{out}}{R_\mu}. \qquad (3.7.136)$$

The terminal resistance R_μ is connected to the 1-D formulation, imposing that (A^u, U^u) satisfies the equation (3.7.136), so that

$$Q^u = A^u U^u = \frac{p(A^u) - p_{out}}{R_\mu}, \qquad (3.7.137)$$

with $p(A^u)$ expressed by the *tube law* (3.2.11). The invariance of W_f is also assumed at the final point of the terminal artery,

$$W_f(A_L, U_L) = W_f(A^u, U^u), \qquad (3.7.138)$$

which is combined with (3.7.137) to obtain a non-linear equation in A^u, given by

$$F(A^u) = R_\mu \widetilde{W}_f A^u - 4 R_\mu \sqrt{\frac{\beta_L}{2\rho A_{0_L}}} (A^u)^{\frac{5}{4}} +$$

$$-p_0 - \frac{\beta_L}{A_{0_L}} \left(\sqrt{A^u} - \sqrt{A_{0_L}} \right) + p_{out} = 0, \qquad (3.7.139)$$

with $\widetilde{W}_f = U_L + 4\sqrt{\frac{\beta_L}{2\rho A_{0_L}}} (A_L)^{\frac{1}{4}}$. The equation (3.7.139) can be solved with respect to A^u using the Newton method (with $A^u = A_L$ has initial hypothesis), and U^u is computed by (3.7.137) as

$$U^u = \frac{p(A^u) - p_{out}}{R_\mu A^u}. \qquad (3.7.140)$$

The terminal boundary condition is defined through (3.7.72) with $U_{bc} = U^u$ and assuming $A_R = A_L$.

In the linear formulation R_μ is connected to R_t. A substitution of (3.5.42) and (3.5.43) in $R_t = -\Delta W_b / \Delta W_f$ leads to

$$R_t = \frac{-\Delta u + \frac{c_{0_L}}{A_{0_L}} \Delta a}{\Delta u + \frac{c_{0_L}}{A_{0_L}} \Delta a}.$$

Expressing Δa in terms of Δp using (3.5.41), and multiplying numerator and denominator for $\frac{\rho c_{0_L}}{A_{0_L} \Delta u}$,

$$R_t = \frac{R_\mu - \frac{\rho c_{0_L}}{A_{0_L}}}{R_\mu + \frac{\rho c_{0_L}}{A_{0_L}}}, \qquad (3.7.141)$$

is obtained, with $R_\mu = \frac{\Delta p}{A_{0_L} \Delta u}$.

Windkessel model with two elements (RC)

In this model a compliance C is added at the model with R_μ showed in Figure 3.10, (a). The electric circuit of the resulting model with lumped parameters is shown in Figure 3.10, (b), and the 0-D governing equations follows from (3.7.120) considering $L = 0$,

$$\begin{cases} C\frac{dp_{in}}{dt} + Q_{out} - Q_{in} = 0, \\ R_\mu Q_{out} + p_{out} - p_{in} = 0. \end{cases} \qquad (3.7.142)$$

These lead to

$$C\frac{dp_{in}}{dt} + \frac{p_{in} - p_{out}}{R_\mu} - Q_{in} = 0, \qquad (3.7.143)$$

which can be written in the discrete form using a first-order finite difference approximation in time, such that

$$p\left(A_{in}^n\right) = p\left(A_{in}^{n-1}\right) + \frac{\Delta t}{C}\left(Q_{in}^{n-1} - \frac{p\left(A_{in}^{n-1}\right) - p_{out}}{R_\mu}\right). \qquad (3.7.144)$$

A substitution of the tube law (3.2.11) in (3.7.144) gives

$$\sqrt{A_{in}^n} = \sqrt{A_{in}^{n-1}} + \frac{\Delta t A_{0_L}}{C \beta_L}\left[Q_{in}^{n-1} + \frac{1}{R_\mu}\left(p_{out} - p_0 + \right. \right.$$
$$\left. \left. - \frac{\beta_L}{A_{0_L}}\left(\sqrt{A_{in}^{n-1}} - \sqrt{A_{0_L}}\right)\right)\right]. \qquad (3.7.145)$$

This relation is connected to the 1-D formulation considering $(A^u)^n = A_{in}^n$, $(A^u)^{n-1} = A_{in}^{n-1}$ and $U_R = U_L$. For the first temporal step $(n = 1)$, A_{in}^0 is equal to the referring area at the final point of the 1-D arterial domain. The boundary condition is defined by the (3.7.71) with $A_{bc} = (A^u)^n$.

Windkessel model with three elements (RCR)

The RC model showed in the previous paragraph produces oscillations of pressure and flow which disappears when a second resistance in front of C is added. This leads to a model with two resistances, R_{μ_1} and R_{μ_2}, and a compliance C (Figure 3.10, (c)). This model is constitute by two coupled compartments: a model with one resistance (R_{μ_1}) coupled with the 1-D terminal branch, followed by a $R_{\mu_2}C$ model. The first resistanceR_{μ_1} is governed by the equation

$$Q_{in} = \frac{p_{in} - p_C}{R_{\mu_1}}, \tag{3.7.146}$$

and the system $R_{\mu_2}C$ by the equations

$$\begin{cases} C\frac{dp_C}{dt} + Q_{out} - Q_{in} = 0, \\ R_{\mu_2}Q_{out} + p_{out} - p_C = 0, \end{cases} \tag{3.7.147}$$

with p_C representing the pressure through C. The RCR model is coupled with the 1-D terminal branch assuming that the state (A^u, U^u) satisfies the equations (3.7.137)-(3.7.140), with $R_\mu = R_{\mu_1}$ and $p_{out} = p_C$. The value of A^u is obtained by (3.7.139) and the once of U^u by (3.7.140). The boundary condition is defined through the (3.7.72) with $U_{bc} = U^u$ and assuming $A_R = A_L$. At each time step n, p_C is determined by the resolution of a first-order time discretization of the mass conservation in (3.7.147),

$$p_C^n = p_C^{n-1} + \frac{\Delta t}{C}\left(Q_{in}^{n-1} - Q_{out}^{n-1}\right), \tag{3.7.148}$$

with $Q_{in}^{n-1} = (A^u)^{n-1}(U^u)^{n-1}$ and $Q_{out}^{n-1} = \frac{p_C^{n-1} - p_{out}}{R_{\mu_2}}$. The pressure p_C^{n-1} is assumed to be null for $n = 1$.

Since the resistance R_{μ_1} has been added in order to eliminate the oscillations of the $R_{\mu_2}C$ model, the wave coming from the 1-D terminal branch can reach C and R_{μ_2}, without been reflected in R_{μ_1}. This is obtained considering $R_t = 0$ in the compartment of R_{μ_1}, based on the (3.7.141), which leads to

$$R_{\mu_1} = \frac{\rho c_{0_L}}{A_{0_L}}. \tag{3.7.149}$$

The same algorithm is used to couple the 1-D linear formulation to a RCR windkessel model, even though the equation (3.7.139) has an analytic solution. According to (3.5.41), the equation (3.7.146) becomes

$$Q^u = A^u U^u = \frac{\frac{\rho\left(c_{0_L}\right)^2}{A_{0_L}}\left(A^u - A_{0_L}\right) - p_C}{R_{\mu_1}}, \tag{3.7.150}$$

and for the (3.5.42), the equation (3.7.138) takes the form

$$\Delta W_f\left(A_L, U_L\right) = U^u + \frac{c_{0_L}}{A_{0_L}}\left(A^u - A_{0_L}\right), \tag{3.7.151}$$

with $\Delta W_f\left(A_L, U_L\right) = U_L + \frac{c_{0_L}}{A_{0_L}}\left(A^u - A_{0_L}\right)$. A combination of (3.7.150) and (3.7.151) gives

$$R_{\mu_1}\frac{c_{0_L}}{A_{0_L}}\left(A^u\right)^2 + \left(\frac{\rho\left(c_{0_L}\right)^2}{A_{0_L}} - R_{\mu_1}\left(\Delta W_f + c_{0_L}\right)\right)A^u +$$
$$- \left(\rho\left(c_{0_L}\right)^2 + p_C\right) = 0. \tag{3.7.152}$$

Windkessel model with four elements (RCLR)

The last model considered includes the compliance of the wall, the fluid resistance and the inertia of the vessels beyond the terminal artery (Figure 3.10, (d)). The initial resistance R_{μ_1} is governed by the equation (3.7.146), and the system $R_{\mu_2}CL$ by the equations

$$\begin{cases} C\frac{dp_C}{dt} + Q_{out} - Q_{in} = 0, \\ L\frac{dQ_{out}}{dt} + R_{\mu_2}Q_{out} + p_{out} - p_C = 0, \end{cases} \tag{3.7.153}$$

with p_C the pressure across C. At the time step n, the equation (3.7.146) takes the form

$$Q_{in}^n = \frac{p_{in}^n - p_C^n}{R_{\mu_1}}.$$ (3.7.154)

The mass conservation equation in (3.7.153) is expressed with respect to the time in the first-order form as

$$p_C^n = p_C^{n-1} + \frac{\Delta t}{C}\left(Q_{in}^n - Q_{out}^n\right),$$ (3.7.155)

and the momentum equation as

$$Q_{out}^n = \left(1 - \frac{\Delta t R_{\mu_2}}{L}\right) Q_{out}^{n-1} + \frac{\Delta t}{L}\left(p_C^{n-1} - p_{out}\right).$$ (3.7.156)

Replacing (3.7.155) in (3.7.154), whit Q_{out}^n expressed by (3.7.156), there is

$$Q_{in}^n = \frac{1}{R_{\mu_1} + \frac{\Delta t}{C}}\left[p_{in}^n + p_C^{n-1}\left(\frac{\Delta t^2}{LC} - 1\right) + \right.$$

$$\left. + Q_{out}^{n-1}\left(1 - \frac{\Delta t R_{\mu_2}}{L}\right)\frac{\Delta t}{C} - p_{out}\frac{\Delta t^2}{CL}\right].$$ (3.7.157)

It is possible to verify that the state (A^u, U^u) satisfies the (3.7.157) with $Q_{in}^n = (A^u)^n (U^u)^n$ and $p_{in}^n = p\left((A^u)^n\right)$, according to the (3.2.11). A combination of (3.7.138) and (3.7.157) leads to a non-linear equation in A^u which can be solved using the Newton's method (with $A^u = A_L$ as initial hypothesis). Later, $(U^u)^n$ is computed using (3.7.138). The boundary condition is defined through the (3.7.72) with $U_{bc} = U^u$ and assuming $A_R = A_L$. The value of Q_{out}^n is updated at each time step, using the (3.7.156). Once that Q_{out}^n is known, p_C^n is updated through the (3.7.155), with $Q_{in}^n = (A^u)^n (U^u)^n$.

In the linear formulation, the equations (3.7.151) and (3.7.157) are combined to obtain a relation with A^u as unknown, with an analytic solution. The rest of the algorithm follows by the non-linear formulation.

3.8   Estimation of peripheral resistance, inertia and compliance

In this paragraph a technique based on scaling laws is proposed, in order to estimate the resistance, the flow inertia and the wall compliance of neglected vessels perfused by the terminal branches of the 1-D model. This technique assumes the radii constant and ignores the lengths of the neglected vessels (even though they vary in each junction), and it is supposed that the vessels are in a tree of junctions without the anastomosis present in the network formed by the peripheral vessels.

According to the researches of Papageorgiou and Jones [27], the radii and the length of the next generations of bifurcations can be approximated by geometrical series, that is, if R_0 is the initial radius and l_0 is the length of the terminal artery, then the radius R_1 and the length l_1 of its two daughters are given by

$$R_1 = \varphi R_0, \qquad l_1 = \lambda l_0,$$

with φ and λ constant scaling factors. Following the same procedure, the radius R_2 and the length l_2 of each of the four vessel generated after the second bifurcation can be expressed as

$$R_2 = \varphi R_1, \qquad l_2 = \lambda l_1.$$

Generalizing, for the nth bifurcation there is

$$R_n = \varphi R_{n-1}, \qquad l_n = \lambda l_{n-1}, \qquad (3.8.158)$$

with R_n and l_n the radius and the length of each of the 2^n vessels after the nth bifurcation. These values are connected to R_0 and l_0 through

$$R_n = \varphi^n R_0, \qquad (3.8.159)$$

$$l_n = \lambda^n l_0. \qquad (3.8.160)$$

Hence, the cross-sectional area of each vessel after the nth bifurcation is

$$A_n = \pi R_n^2 = \varphi^{2n} A_0, \qquad (3.8.161)$$

with A_0 the cross-sectional area of the terminal artery at the reference state $(A, p, U) = (A_0, p_0, U_0)$. The sum of the areas A_n of the 2^n vessels after the nth bifurcation, A_{T_n}, is

$$A_{T_n} = 2^n A_n = \left(2\varphi^2\right)^n A_0. \qquad (3.8.162)$$

Similarly, the volume of the 2^n vessels after the nth bifurcation, V_{T_n}, is

$$V_{T_n} = 2^n A_n l_n = \left(2\lambda\varphi^2\right)^n V_0, \qquad (3.8.163)$$

with $V_0 = A_0 l_0$. The lateral surface of the 2^n vessels after the nth bifurcation, S_{T_n}, is

$$S_{T_n} = 2^n 2\pi R_n l_n = \left(2\varphi\lambda\right)^n S_0, \qquad (3.8.164)$$

with $S_0 = 2\pi R_0 l_0$.
The value of φ and λ can be limited assuming that:

1. The radius of each vessel decreases after each bifurcation, that is $\varphi < 1$.

2. The length of each vessel decreases after each bifurcation, that is $\lambda < 1$.

3. The total cross-sectional area increases after each bifurcation to the capillaries, that is $2\varphi^2 > 1$.

4. The total volume decreases after each bifurcation, that is $2\lambda\varphi^2 < 1$.

5. The total lateral surface increases after each bifurcation, that is $2\lambda\varphi > 1$.

The latest two conditions aim to providing blood perfusion in a vessel with a small volume and a big lateral surface, the Figure 3.11 shows these conditions in the space (φ, λ). The shaded area contains the set of values of φ and λ which satisfy all constraints. The choice of a valid couple of values of φ and λ is bounded to a small region. For a given φ, λ is bounded by

$$\frac{1}{2\varphi} < \lambda < \frac{1}{2\varphi^2}. \qquad (3.8.165)$$
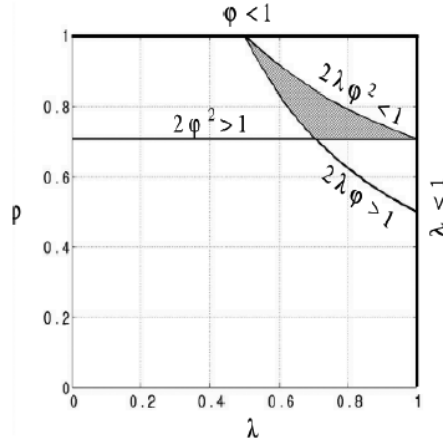
Figure 3.11 The scaling factors φ and λ, used to estimate the radius and the length of the blood vessels perfused by the 1-D terminal branches, are bounded to the shaded region, for the constrained described in the text.

In the next paragraphs the scaling law just proposed will be used to estimate total resistance, inertia and compliance of the vessels neglected by the 1-D model.

3.8.1   Resistance

In each vase, supposing to treat a Poiseuille's flow, the gradient of pressure Δp_n after the nth bifurcation is connected to the flow rate, Q_n, through

$$\Delta p_n = \frac{8\mu l_n}{\pi \left(R_n\right)^4} Q_n. \tag{3.8.166}$$

It is possible to observe that the Poiseuille's flow is an approximation of the pulse flow observed in small arteries and of the non Newtonian behavior of the blood in arterioles and capillaries. The flow rate is assumed to be the same in each of the 2^n vessels, then $Q_n = \frac{Q_0}{2^n}$, where Q_0 is the mean flow at the extremity of the terminal artery. Therefore, replacing the relations (3.8.159) and

(3.8.160) in (3.8.166) leads to

$$\Delta p_n = \left(\frac{\lambda}{2\varphi^4}\right)^n \frac{8\mu l_0}{\pi (R_0)^4} Q_0 = \left(\frac{\lambda}{2\varphi^4}\right)^n \Delta p_0, \qquad (3.8.167)$$

with Δp_0 the gradient of the mean pressure in the 1-D terminal artery.

According to (3.8.167), the gradient of the pressure is the same in all vessels after the nth bifurcation. So, in a network with N generations of bifurcations, the gradient of the pressure between the outlet of the terminal artery and the ones of the vessels after the Nth bifurcation, Δp_T, is the sum of the gradients of the pressure Δp_n after each bifurcation across the network, starting from the outlet of the terminal artery, that is

$$\Delta p_T = \sum_{n=1}^{N} \Delta p_n = \Delta p_0 \sum_{n=1}^{N} \left(\frac{\lambda}{2\varphi^4}\right)^n. \qquad (3.8.168)$$

Dividing Δp_T for Q_0, the resistance $R_{\mu_{T_N}}$ of a network with N generations of bifurcations related to the terminal artery is obtained by

$$R_{\mu_{T_N}} = R_{\mu_0} \sum_{n=1}^{N} \left(\frac{\lambda}{2\varphi^4}\right)^n, \qquad (3.8.169)$$

with $R_{\mu_0} = \frac{\Delta p_0}{Q_0}$. It is possible to observe that $\frac{\lambda}{2\varphi^4}$ is not always smaller than 1. If it is true, then $R_{\mu_{T_N}}$ converges to R_{μ_T} when N goes to infinity, with

$$R_{\mu_T} = \left(\frac{1}{1 - \frac{\lambda}{2\varphi^4}} - 1\right) R_{\mu_0} = \left(\frac{\lambda}{2\varphi^4 - \lambda}\right) R_{\mu_0}. \qquad (3.8.170)$$

3.8.2 Inertia

According to (3.7.118), the inertia L_n of the blood in a vessel after the nth bifurcation is

$$L_n = \frac{\rho l_n}{A_n}. \qquad (3.8.171)$$

A substitution of (3.8.160) and (3.8.161) in (3.8.171) gives

$$L_n = \left(\frac{\lambda}{\varphi^2}\right)^n L_0, \tag{3.8.172}$$

with $L_0 = \rho l_0 / A_0$. Since the inductances (or inertias) can be summed in the same way of the resistances, the total inertia L_{T_n} of the 2^n vessels after the nth bifurcation is

$$L_{T_n} = \frac{L_n}{2^n} = \left(\frac{\lambda}{2\varphi^2}\right)^n L_0. \tag{3.8.173}$$

The inertia L_T of the entire network related to the terminal artery is the sum of the L_{T_n} after each bifurcation (except for L_0). Since $\lambda < 1$ and $\varphi^2 > \frac{1}{2}$ (see figure 3.11), then $\frac{\lambda}{2\varphi^2} < 1$ and L_T converges to

$$L_T = \sum_{n=1}^{\infty} L_{T_n} = \left(\frac{1}{1 - \frac{\lambda}{2\varphi^2}} - 1\right) L_0 = \left(\frac{\lambda}{2\varphi^2 - \lambda}\right) L_0. \tag{3.8.174}$$

3.8.3   Compliance

According to (3.3.25), c_0 is proportional to $A_0^{-1/4}$. If c_n is assumed to be proportional to $A_n^{-1/4}$ for each generation of bifurcations, then from the (3.8.161),

$$c_n = \varphi^{-n/2} c_0, \tag{3.8.175}$$

is obtained. For the (3.7.119), the compliance of a vessel after the nth bifurcation is

$$C_n = \frac{A_n l_n}{\rho \left(c_n\right)^2}. \tag{3.8.176}$$

Replacing (3.8.160), (3.8.161) and (3.8.175) in (3.8.176) there is

$$C_n = \left(\lambda \varphi^3\right)^n C_0, \tag{3.8.177}$$

with $C_0 = \frac{A_0 l_0}{\rho (c_0)^2}$. The total compliance C_{T_n} of the vessels after the nth bifurcation is

$$C_{T_n} = 2^n C_n = \left(2\lambda\varphi^3\right)^n C_0. \tag{3.8.178}$$

The compliance C_T of the whole network related to the terminal artery is obtained by summing the compliances C_{T_n} after each bifurcation (except for C_0). Since $\varphi < 1$ and $2\lambda\varphi^2 < 1$ (see Figure 3.11), there is $2\lambda\varphi^3 < 1$ and C_T converges to

$$C_T = \sum_{n=1}^{\infty} C_{T_n} = \left(\frac{1}{1 - 2\lambda\varphi^3} - 1 \right) C_0 = \left(\frac{2\lambda\varphi^3}{1 - 2\lambda\varphi^3} \right) C_0.$$
(3.8.179)

This convergence is obtained after few generations, and so, the smallest arteries, arterioles and capillaries give a little contribution to the total peripheral compliance, which justifies the assumption of a pulsatile flow in its determination.

3.9 Optimal control of mean arterial pressure

In this paragraph the optimal control problem of achieving a prescribed mean arterial pressure by allowing for variable terminal resistance $R_t = R$ during the time period $[t_0, t_0 + T_{pulse}]$ of one heart beat, $T_{pulse} = 60/HR$, is considered. Note that the optimization on the heart rate HR is not performed, since the HR can be controlled separately.

The optimal control problem is formulated using the system:

$$\frac{\partial \mathbf{U}}{\partial t} + \frac{\partial \mathbf{F}(\mathbf{U})}{\partial x} = \mathbf{S}(\mathbf{U}),$$
(3.9.180)

and it is written as an initial value problem in the Hilbert space $X = L^2([0, M]) \times L^2([0, M])$:

$$\mathbf{U}'(t) = \mathcal{G}(t, \mathbf{U}(t), y), \quad \mathbf{U}(0) = \mathbf{U}_0$$

where $\mathcal{G}(t, \mathbf{U}, y) = -A_y(\mathbf{U}) + \mathbf{S}(\mathbf{U})$ and A_y is an unbounded operator on X

$$A_y(\mathbf{U}) = \frac{\partial \mathbf{F}(\mathbf{U})}{\partial x}$$

with domain

$$D(A_y) = \{\mathbf{U} = (A; U) \in X = L^2([0, L]) \times L^2([0, L]) : W_b = -yW_f\}$$

encodes the boundary conditions in terms of the control variable y (expressed as boundary control). In this application $y = R_t$ is the terminal reflection coefficient which is allowed to vary during the time period of one heart beat $T = 60/HR$.

The optimization task is defined as follows: determine the optimal terminal resistance that achieves the desired mean pressure. This is a nontrivial fact, since the external pressure is assumed variable (possibly due to a sudden drop or rise in pressure), the system tries to find the optimal value of the heart rate that achieves the desired goal.

The optimal control problem is to find $y = y(t)$ that minimizes the integral

$$J_1 = \int_0^T |P_{avg}(t) - P_{ref}|^2 \, dt = \int_0^T \left| \frac{1}{M} \int_0^M P(x, t) \, dx - P_{ref} \right|^2 \, dt.$$

Due to the non-standard nature of the Dirichlet boundary control problem posed, it is expected that the full PDE boundary control will lead to an adjoint formulation of the optimal control problem involving integral formulation of the necessary condition for optimality (see [23]). This will be pursued elsewhere. In the sequel it is turned to a pseudo spectral discretization of the optimal control problem [24], [35]. The discretization uses the same framework as the numerical scheme already discussed, using Legendre polynomials and Legendre Gauss nodes. For simplicity, this discretization procedure on an optimal control problem for the Dirichlet boundary control for the viscous Burgers equation is described:

$$\begin{cases} u_t + uu_x - \nu u_{xx} = f, & x \in [0, M], t \in [0, T], \\ u(x, 0) = u_0(x), & x \in [0, M], \\ u(0, t) = g(t), \quad u(M, t) = h(t), & t \in [0, T], \end{cases}$$

with g and h the controls, and cost functional to be minimized

$$J(g,h) = \int_0^T \int_0^M |u(x,t) - u_{ref}(x,t)|^2 \, dxdt,$$

where u_{ref} is a reference (desired) profile for the solution.

The Legendre-Gauss-Lobatto (LGL) points $-1 = x_0 < x_1 < \ldots x_{N-1} < x_N = 1$, (cf. [35]) have been chosen, where $x_1, \ldots x_{N-1}$ are the zeros of L'_N, the derivatives of the Legendre polynomial of degree N and the function u is approximated using the Lagrange interpolants for the points $(x_j, u(x_j))$. Then the approximate solution is introduced:

$$u^N(\xi) = \sum_{k=0}^N \widehat{u}^k L_k(\xi),$$

and the optimal PDE control problem is converted to the optimal ODE control problem:

$$\text{Minimize } \int_0^T \sum_{k=0}^K |\widehat{u}^k - \widehat{u_{ref}}^k|^2 dt,$$

subject to

$$\frac{d\widehat{u}^k}{dt} = \mathcal{F}_k(\widehat{u}^1, \ldots, \widehat{u}^K; g, h). \tag{3.9.181}$$

Here the right-hand side is obtained from the variational formulation of the PDE:

$$\frac{d}{dt}(u, \phi)_{L^2} - 1/2(u^2, \phi_x)_{L^2} + \nu(u_x, \phi_x)_{L^2} = (f, \phi)_{L^2}.$$

If the test functions are restricted to polynomials of degree N or less, then

$$\frac{d}{dt}(u^N, L_k)_{L^2} - 1/2((u^N)^2, (L_k)_x)_{L^2} + \nu(u_x^N, (L_k)_x)_{L^2} = (f, L_k)_{L^2},$$

or

$$\frac{d}{dt}\widehat{u}^k + 1/2\left(((u^N)^2)_x, L_k\right)_{L^2} - \nu\left(u^N, (L_k)_{xx}\right)_{L^2} + B_k = (f, L_k)_{L^2},$$

is obtained. Here the boundary contribution is

$$B_k = -1/2(u^N)^2 L_k + \nu (u^N L_k')\big|_{x=0}^{x=M}.$$

This leads to the expression for the right hand side in (3.9.181):

$$\mathcal{F}_k(\widehat{u}^1, \dots, \widehat{u}^K; g, h) =$$
$$= -1/2 \left(((u^N)^2)_x, L_k\right)_{L^2} + \nu \left(u^N, (L_k)_{xx}\right)_{L^2} - B_k + (f, L_k)_{L^2}.$$

Note that B_k can be written in terms of the boundary control as:

$$B_k = g(t)^2/2 - h(t)^2/2 + \nu(h(t)L_k'(M) - g(t)L_k'(0)).$$

Applying Pontryagin minimum principle an adjoint problem for the adjoint variables λ^k, $k = 0, \dots, K$ is obtained

$$\frac{d\lambda^k}{dt} = -\frac{\partial \mathcal{H}}{\partial \widehat{u}^k}, \tag{3.9.182}$$

where

$$\mathcal{H} = \sum_{k=0}^{K} |\widehat{u}^k - \widehat{u_{ref}}^k|^2 - \sum_{k=0}^{K} \lambda^k \mathcal{F}_k(\widehat{u}^1, \dots, \widehat{u}^K; g, h),$$

is the Hamiltonian. A necessary optimal condition is then $\nabla_{g,h}\mathcal{H} = 0$, for each fixed time t, which yields the optimal values $g^*(t)$ and $h^*(t)$.

A similar construction can be carried out for the inviscid Euler system (3.9.180), which yields, upon discretization using the same Gauss Legendre Lobatto points, the system

$$\frac{d\widehat{U}_i^k}{dt} = \mathcal{F}_i^k(\widehat{U}; g), \quad i = 1, 2 \quad k = 0, \dots, K.$$

The adjoint system takes the form

$$\frac{d\widehat{\Lambda}_i^k}{dt} = -\frac{\partial \mathcal{H}}{\partial \widehat{U}_i^k}$$

where the Hamiltonian function is

$$\mathcal{H}(\widehat{U}, \Lambda; g) = \mathcal{F}_0(\widehat{U}) - \Lambda_i^k \mathcal{F}_i^k(\widehat{U}; g).$$

Applying of the Pontryagin minimum principle leads to the computation of the optimal $g^*(t)$. It is possible to remark that while this is a nonstandard application of the Pontryagin minimum principle, it follows the same steps as the traditional principle where pure Dirichlet boundary conditions are involved.

Chapter 4

Numerical results

In this chapter several simulation results are discussed, considering different formulations of the model and different types of networks. In particular in the first paragraph the algebraic formulation for the pressure and four optimization scenarios on artificial networks are presented. As inflow condition a periodic flow is prescribed, in order to mimic the behavior of the cardiac valve. In the second paragraph, the algebraic formulation for the pressure is still used, but the tilt table test is performed, considering the 55-edge tree with the main arteries of the cardiovascular system. In this case the cardiac valve is modeled, taking into consideration the relation between the aortic pressure and the left ventricular pressure. In the last paragraph the convective term in the mathematical formulation is added and an optimization scenario is proposed. The aortic valve is modeled in this case too.

4.1 Optimization scenarios on artificial networks

In this section some simulation results addressing several scenarios are presented: (1) the effect that truncation in a fractal network has to the flow in the root edge; (2) the effect that adding or subtracting an edge has to the network dynamics; (3) the effect

that growth of a given network has on the dynamics when a desired total outflow is obtained and (4) optimization of the heart rate in the event of a blockage/unblockage of an edge or of an entire subtree.

The model considered is the following:

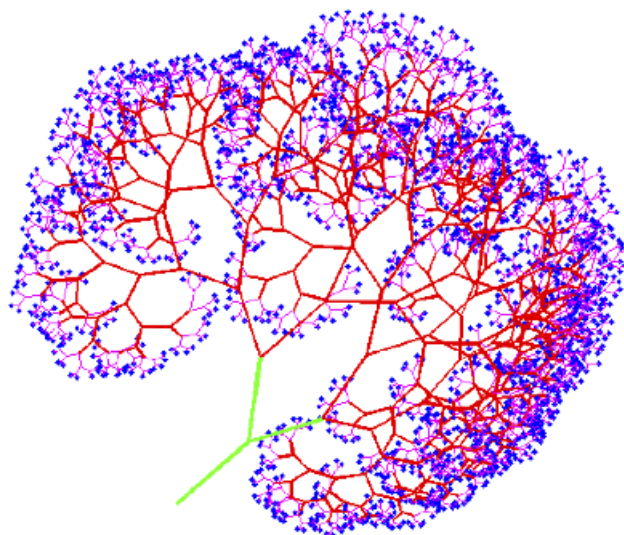$$\frac{\partial A}{\partial t} + \frac{\partial (AU)}{\partial x} = 0, \tag{4.1.1}$$

$$\frac{\partial U}{\partial t} + U\frac{\partial U}{\partial x} + \frac{\partial p}{\partial x} = f, \tag{4.1.2}$$

with

$$p = p_{ext} + \frac{\beta\sqrt{\pi}}{A_0}(\sqrt{A} - \sqrt{A_0}) \tag{4.1.3}$$

and $f = f(x,t)$ is a friction force, usually taken to be $f = -22\mu\pi U/A$, where μ is the fluid viscosity.

Figure 4.1 illustrates a fractal tree with $n = 10$ generations, although in the sequel the simulations will be restricted to fractal trees with smaller number ($n \leq 3$) of generations.


Figure 4.1   3D fractal tree with 10 generations.

For the simulations, a periodic inflow (at the root of the network) is prescribed, with period $T = 60/HR$, as $Q = Q_{bc}(t)$ in *liters/sec*, where

$$Q_{bc}(t) = \begin{cases} 6.75 \times 10^{-4} \sin\left(\dfrac{\pi t}{\tau}\right), & \text{for } t \in [0, \tau], \\ 0, & \text{for } t \in [\tau, T] \end{cases}$$

with $\tau = T/4$ is a quarter of the heart beat period. The following parameter values are used throughout the sequel: $\mu = 4 \times 10^{-3}\ Pa$ (viscosity of the blood), $\rho = 1050\ Kg/m^3$ (blood density), $p_0 = 1862\ Pa$ (external pressure).

Multiple runs were performed for various values of the resistance in an asymmetric tree with 2 generations ($R_t = 0.3$, $R_t = 0.8$, $R_t = 1$). The case $R_t = 1$ corresponds to zero outflow boundary condition (clamped terminal edges). In the case of low resistance no (or little) pressure build-up is observed, while for high resistance there is noticeable build up (see Figure 4.2). There is an almost linear buildup of the mean arterial pressure in the system, which continues until the rate of outflow balances the rate of inflow, at which time the pressure stabilizes.
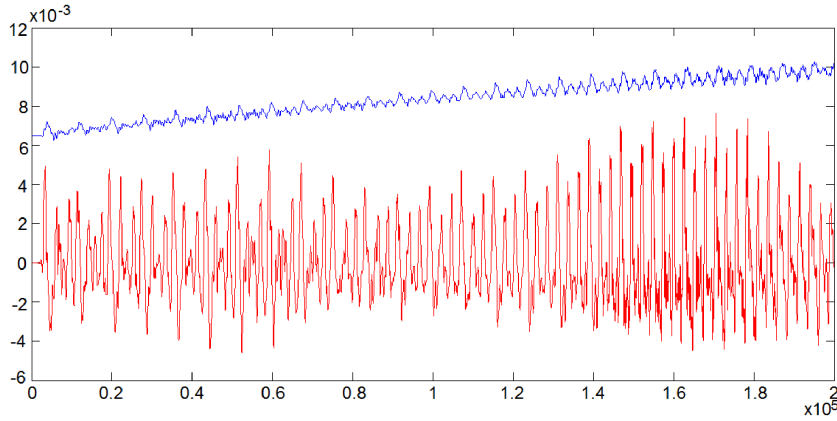
Figure 4.2 Oscillations in time ($R_t = 0.8$), during pressure build-up, with time step 10^{-4}. The blue line represents the pressure (scaled) and red line represents the flow velocity.

Even in artificial networks such as the ones considered here, one notices an oscillatory behavior of the flow (in the presence of the pressure build-up), in this case with a period of about 10 seconds. This resembles the physiological phenomenon of the Mayer waves present in the vascular system, although the $10\,sec$ period may be only coincidental. Mayer waves are oscillations at a much slower frequency (0.1 Hz) than the heart beat or even respiration (0.25-0.3 Hz), and are partly responsible for the variability of the heart rate, manifested in the autoregulation mechanism. Mayer's waves are sometimes attributed to the action of the nervous system, but these oscillations may be in part due to the spatial network itself, by triggering network-induced oscillations.

4.1.1   Effect of truncation of the network

The effect of truncation (by considering fewer generations of the same network) to the flow in the root edge is studied. This may suggest the effectiveness of modifications in the terminal conditions for the simplified tree in order to mimic the behavior in the larger tree.

A simple junction (3-edge tree) with root edge of length $l_1 = 1\,m$ and radius $r_1 = 10\,mm$ and children edges of lengths $l_2 = 0.9\,m$ and $l_3 = 0.8\,m$ and radii $r_2 = 9\,mm$ and $r_3 = 8\,mm$, respectively is considered to begin. A 2-generation self-similar tree based on this junction (see Figure 4.3) in built and the simulation is run using outflow conditions with $R_t = 0.8$.

For the truncation a 3-edge tree that has the same length and radii for the root edge ($\tilde{l}_1 = 1\,m, \tilde{r}_1 = 10\,mm$) is used, while the lengths of the children edges $\tilde{l}_2 = 2.439\,m$ and $\tilde{l}_3 = 1.952\,m$ are chosen to match the lengths of the longest path and shortest path, respectively. The radii in the children edges are $\tilde{r}_2 = 9\,mm$ and $\tilde{r}_3 = 8\,mm$, respectively.

Figure 4.3 The junction (0-gen tree) (left); and the 2-gen fractal tree (right).

Firstly the flow in the middle of the root edge is recorded, when the number of generations of the self-similar network change (from 0 to 2), using the same outflow conditions (R_t value for the terminal resistance). The reference flow profile in the root edge was obtained for terminal resistance $R_t = 0.3$. In Figures 4.4-4.5 temporal recordings for 0-generations and 2-generations are included respectively.
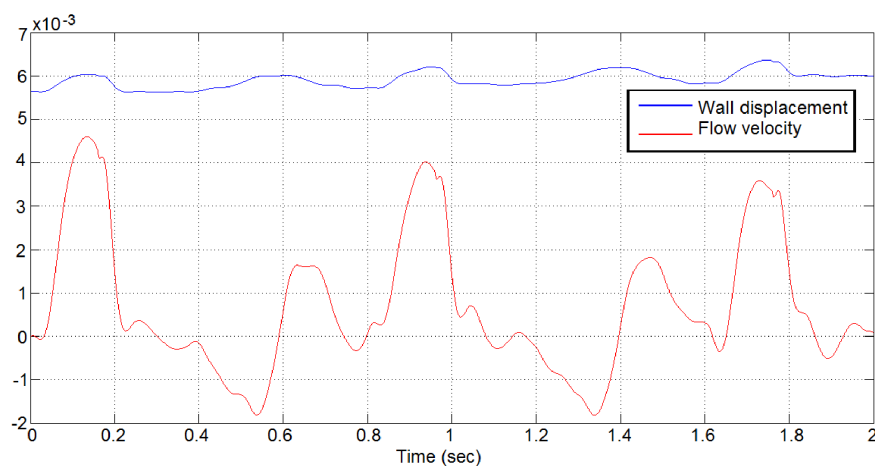
**Figure 4.4** Temporal recordings for 0 generations tree.
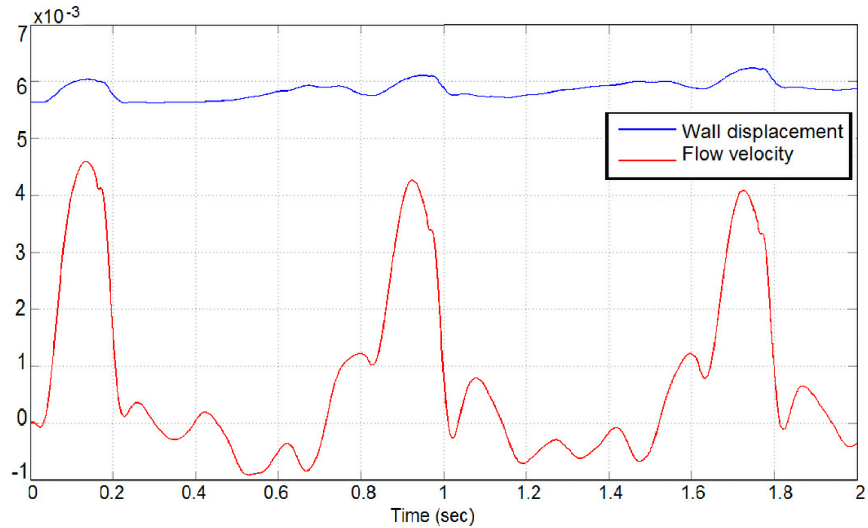
Figure 4.5 Temporal recordings for 2 generations tree.

Notable differences are due to the change in the reflected waves. Even though there is some pressure increase from beat to beat, the flow is close to being periodic and therefore the comparisons can be made even at these stages of the simulation.

Next a numerical optimization on the value of the terminal resistance R_t is performed to be used for the outflow conditions in the simplified tree in order to best match (in least square sense) the flow in the root edge of the simplified tree with the flow in the root edge of the larger tree.

The result of the optimization, which are performed using MATLAB's `minsearch` implementation of the derivative-free Nelder-Mead algorithm, shows that the optimal value for the resistance in the simplified tree is $R_t^* = -0.25$, as shown in Figure 4.6 (right).
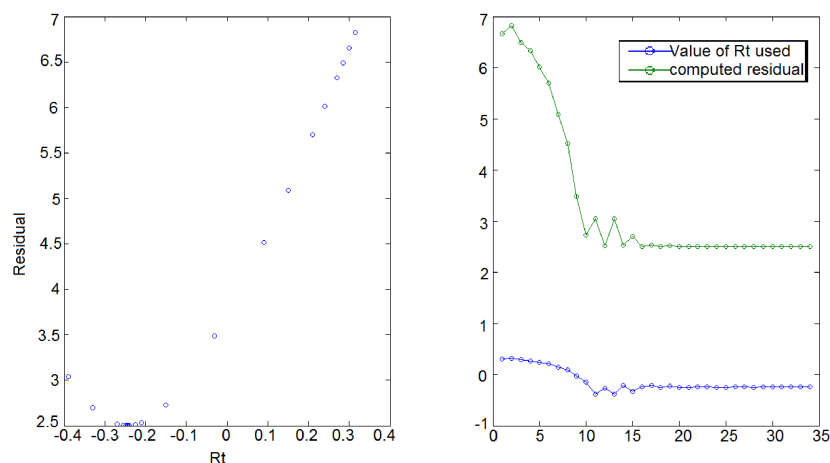
Figure 4.6 Optimization of the terminal reflection coefficient R_t.

Negative values of R_t^* indicates that in the truncated tree the optimal terminal conditions are in such a way that there is no reflected backward characteristics, hence the resistance to flow out is much smaller than in the referenced 2-gen tree.

4.1.2 Effect of adding/removing edges in a network

The effect of adding or subtracting an edge to a given network is investigated. In physiology this phenomenon has been observed (see e.g. [9]). The "efficiency" of the resulting network by measuring the total outflow of the network during a given period of time is studied here. For the simulations, a 7-edge network with cycles (see Figure 4.7) is used, and then the middle edge (see Figure 4.8) is removed.
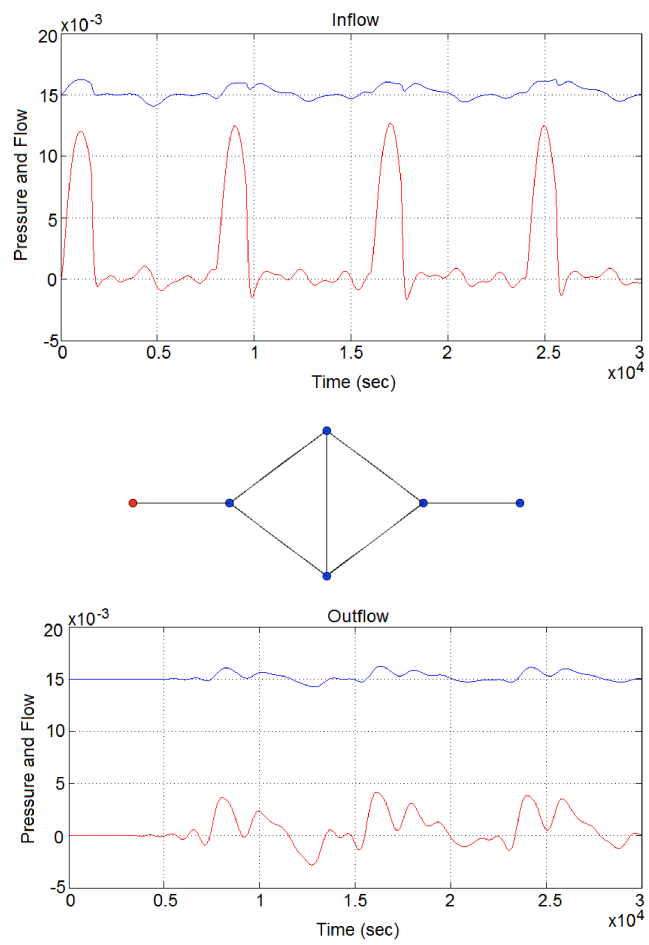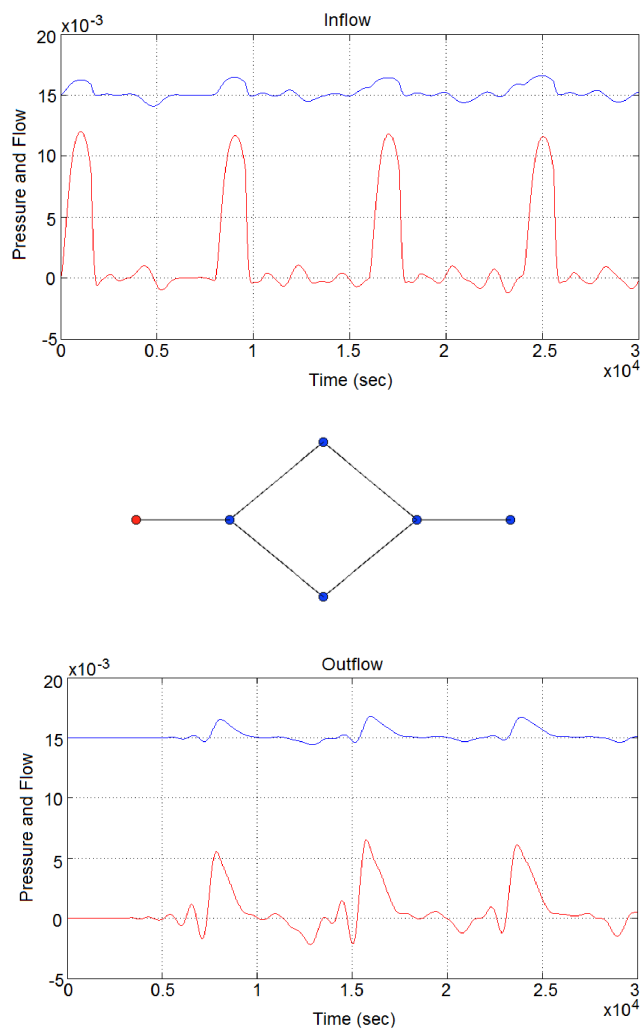
Figure 4.7 Flow and pressure in a network with cycle.

Figure 4.8 Flow and pressure in a network without cycle.

For this very simple network, a total outflow of 0.9552 cm^3 is computed in the presence of the central edge (Figure 4.7), while in its absence (Figure 4.8) the total outflow is increased to 1.0435 cm^3. The inflow during the 3 sec simulation was 3.0706 cm^3. These numerical values are obtained by integrating in time (over the 3 sec time interval) the flow $Q = AU$. Note that the outflow in

both cases is roughly one third of the inflow, the difference being accounted in the volume of fluid that has been "stored" in the network itself, which caused the pressurization of the network at equilibrium.

The results of simulation show that the flow through the network is enhanced when fewer edges (cycles) are present, similar to Braess's paradox in traffic flow, which states that adding extra capacity to a network can in some cases reduce overall performance.

4.1.3   Growth effects on the network dynamics

The effects of a growing network (in size, length and radii) on the heart rate is studied, assuming that this needs to adapt for delivering a desired outflow (per unit volume).

Here it is assumed that the network grows in time (s) at the following rates:

$$l(s) = s^{1/3} l_0, \quad r(s) = s^{1/6} r_0.$$

It is imposed that the desired outflow grows linearly with s:

$$Q^{out}(s) = s Q_0^{out},$$

which indicates that the body mass also grows linearly in time s. The desired outflow is taken proportional to the body mass, in order to deliver the same amount of blood per unit volume. The optimization parameter is taken to be the frequency (heart rate HR) of the inflow pulse (analog of the heart rate), measured in beats/minute. A relationship between the amplitude of the inflow and the HR is assumed (see Figure 4.9) to have a peak value at $HR = 150$ and behave quadratically on the range $50 < HR < 250$ (see [18])

$$\phi(HR) = 1 - 0.4 \left(\frac{HR - 150}{150} \right)^2.$$
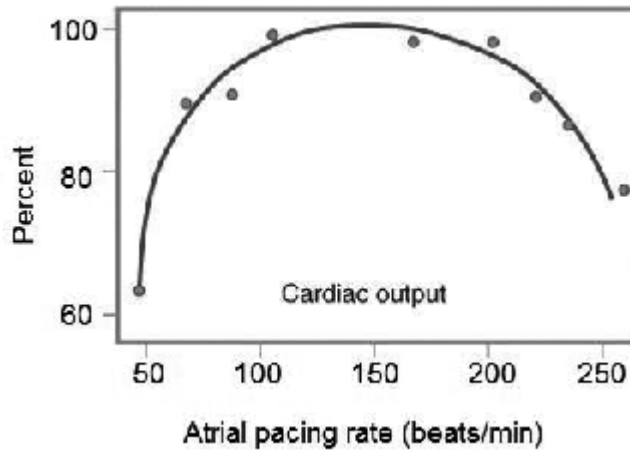
Figure 4.9 Percent of the cardiac output with respect to the atrial pacing rate.

This pacing-dependent amplitude can be attributed to the fact that at the inflow we normally have a valve (the aortic valve) and that the cardiac output is determined dynamically by the aortic pressure and the left ventricular pressure. Here a model of the valve is not included, instead the relationship above to mimic the same effect is used.

The inflow condition during one period of the pulse is chosen as

$$Q^{root} = \phi(HR) * Q_0^{root}.$$

The simulation performs a search for the optimal HR value that achieves the desired $Q^{out}(s)$ at the terminal edge(s) of the network. The network with 7 edges with cycles is used, so that there is only one outlet. The simulation is performed with different values of R_t. Figure 4.10 shows the results obtained using MATLAB's `minsearch.`For each value of s, several iterations are performed in order to find the optimal value of HR. When s is increased, the research starts from the optimal value of HR obtained for the previous value of s.
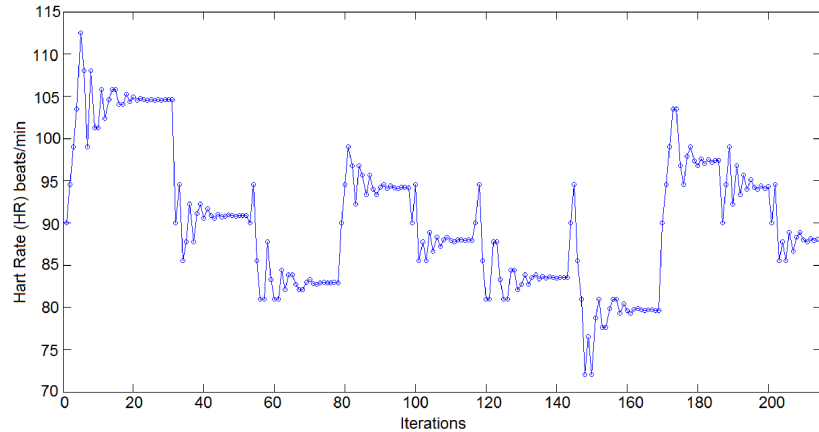
Figure 4.10 Optimization of the outflow to reach desired values using HR as the parameter, for successive values of $s = 1.1, 1.2, \ldots, 2$.

As the network grows from $s = 1$ to $s = 2$, (with $R_t = 0.5$) the optimal HR displays a piece-wise decreasing pattern, with discontinuities at $s = 1.3$ and $s = 1.7$ (Figure 4.10). This suggests that as the network grows in size, the set demand for outflow has a significant influence on the pacing of the pumping. A higher pacing does not necessarily translate into a higher output, partly due to the wave reflections and their timing, partly due to our design of the experiment. In fact, the contrary may true (for certain ranges of s): higher pacing leads to lower output. This decrease in HR is also witnessed in humans, as reported in Table 4.1. In growing vascular systems the optimal HR may actually decrease in time, due to the shift in the relationship of the HR and pump output. These simulation keeps this relationship fixed in time, and the results show a gradual increase in HR as time evolves (simulation runs over a 10 sec period). Another possible improvement of this model would include the baroreceptor control (which lowers the HR when the arterial pressure is elevated), which could also account for the overall decrease in HR, present in physiological growing networks.

4.1.4 Effect of blockages in a network on the flow

Here the time-optimal problem of returning to basal flow and pressure conditions on a network after a temporary blockage of a subnetwork has been removed is investigated. As network the fractal tree with 15 edges (2-generation tree) is considered again. A $20 - sec$ simulation is run for the flow in the entire network before any blockage is applied (see Figure 4.11), with a terminal resistance model and $R_t = 0.8$ for each of the terminal edges.
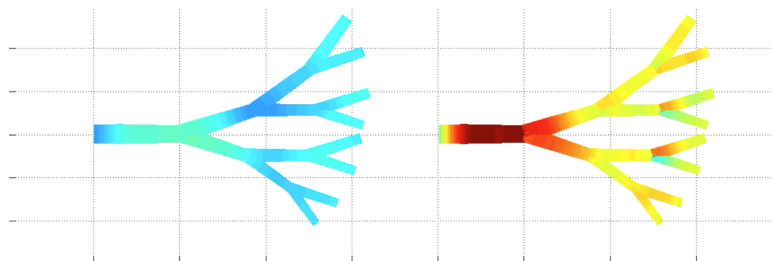
Figure 4.11 Pressure (left) and flow velocity (right) distributions in the network at a fixed time.

The transition time for the flow to settle varies slightly with the heart rate, but it is significantly less than the 20 seconds; e.g. for constant heart rate of $HR = 75$ beats/min, the periodic state

Table 4.1 HR values in human growth.

	HR range
Newborn:	$100 - 140$
One month:	$105 - 185$
One year:	$108 - 170$
$1 - 3$ years:	$90 - 150$
$3 - 5$ years:	$72 - 137$
$5 - 8$ years:	$65 - 132$
$8 - 12$ years:	$62 - 130$
$12 - 16$ years:	$62 - 120$

settles after roughly the first 5 seconds.

Exactly at 20 seconds, an instantaneous blockage at the end of edge 3 is introduced (hence the subnetwork having edge 3 as root is also blocked off - see Figures 4.12). This makes edge 3 a terminal edge (with $R_t = 1$), while the other terminal edges remain at $R_t = 0.8$. A $5 - sec$ simulation is run with this modified network, keeping the heart rate the same as before blockage.
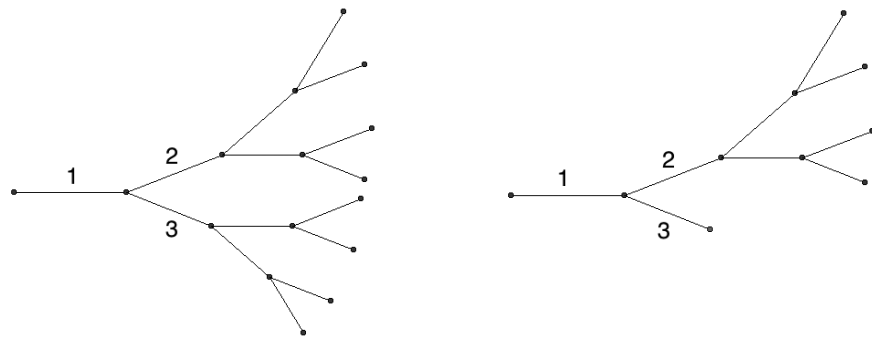
Figure 4.12 Network before and after blockage (left) and during blockage (right).

Finally, after 5 seconds of blockage is over (so at second 25 in the total simulation), the blockage is instantaneously removed and another 15-sec simulation on the original network is run. A return to the previous equilibrium in a certain amount of time is observed, which it is possible to call the recovery time. This is defined as the time that the system take to return at its initial state when the blockage is removed. For $HR = 75$, note that the recovery time is slightly higher than 5 seconds.
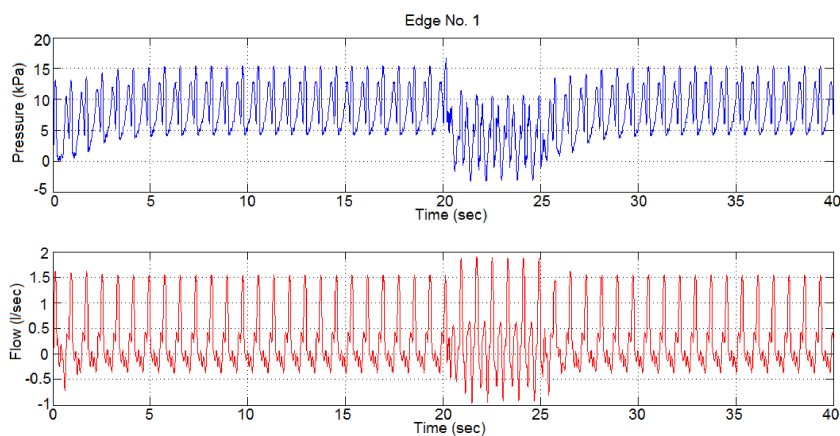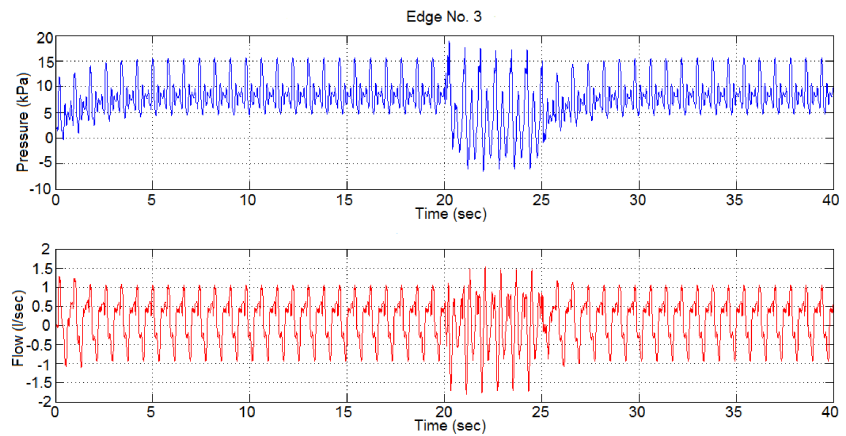
Figure 4.13 Pressure and flow before and after blockage removal in edge 1.

The entire 40-sec sequence of the pressure and flow dynamics in the middle of edge 1 (for $HR = 75$) is included above (see Figure 4.13) and in the middle of a few other edges - 3, 4, 8 - (see Figures 4.14–4.16). Note that during the blockage/unblockage sequence, pressure and flow behave differently in different parts of the network. Most notably, it is possible to see that the blockage happens during the diastolic period, and since it is instantaneous (like a clamping), all the fluid mass past edge 3 is lost and no backflow is generated, hence the upstream pressure (of edge 1) is elevated only for the next systolic period, after which the pressure settles around its new equilibrium value (in this case lower for edge 1). This decrease in steady state pressure values may be different than what is observed in the real vascular system. In that case, an amputation of the distal sub-network causes a significant increase in pressure in the upstream vessels [15].

In edge 3 (see below) the systolic pressure increases during the entire blockage, while in other edges (e.g. No. 4 & No. 8) there is a sustained decrease in systolic pressure. This is consistent with the fact that edge 3 is a terminal edge during the 5-sec blockage. Also, the fact that the bulk of the network is now past edge 4 ex-

plains why the new equilibrium pressures in the new network are lower while the flow is higher. This also suggests that the presence of significant bifurcations more distal is creating less pressure buildup in the upstream vessels.

Figure 4.14 Pressure and flow before and after blockage removal in edge 3.
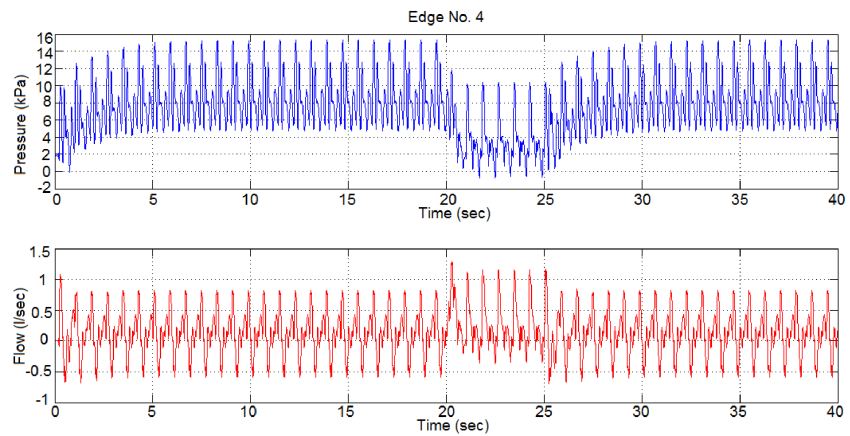
Figure 4.15 Pressure and flow before and after blockage removal in edge 4.
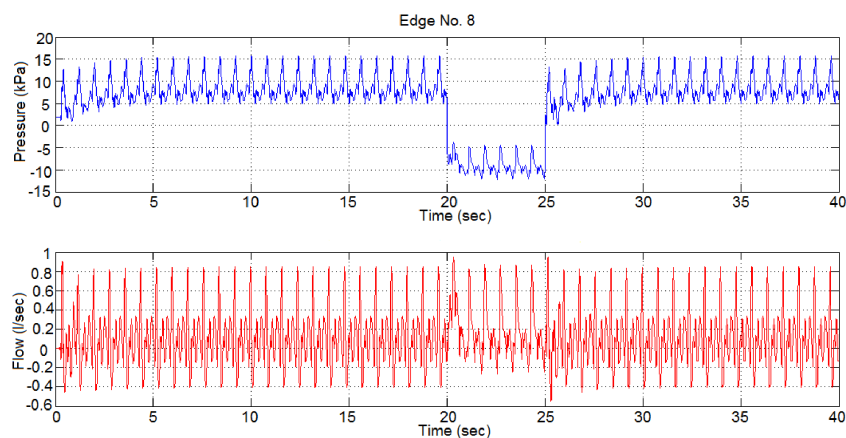
Figure 4.16 Pressure and flow before and after blockage removal in edge 8.

An optimization on the HR parameter is now performed, in order to minimize the recovery time. After 15 iterations *fminsearch* resulted in an optimal value of the parameter $HR = 72.2$ beats/min with a recovery time of 3.5 sec as reported in Figure 4.17.
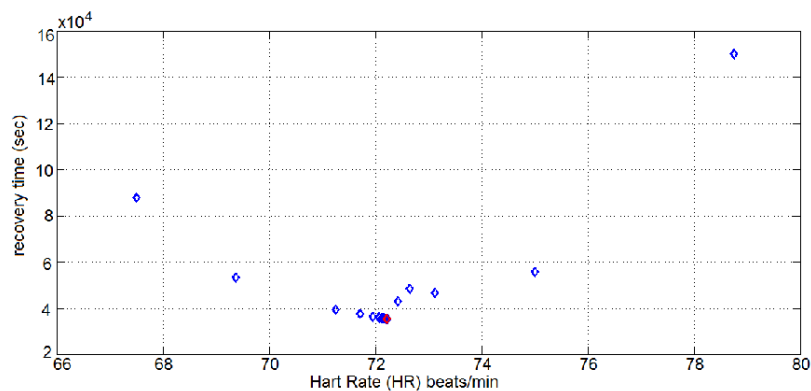
Figure 4.17 Optimization of the HR parameter value, for minimizing recovery time after removal of blockage

Note that values of HR below 70 or above 75 gave much longer

recovery times. In these simulations the mean pressure AMP was computed using a physiologically-inspired formula: $AMP = (P_h + 2 * P_l)/3$, where P_h and P_l are the highest and the lowest value of the pressure. The recovery time was computed when the mean pressure returned to the pre-blockage values.

This result indicates that increasing HR (hence cardiac output) does not necessarily translate to a quicker recovery time, which can be attributed to the reflections at junctions and at the terminal sites. The flows in edge 1 & 3 show an increase in magnitude of the reflected waves.

4.2   Tilt talbe test

In this section numerical results obtained by considering the 55-edge network representing the large arteries in a human are described, in order to simulate the tilt table test.

This test is a medical procedure often used to diagnose dysautonomia or syncope. A tilt table test consists of a table, on which the patient lies monitored in pressure, pulse, electrocardiogram and blood oxygen saturation. The table is suspended at an angle of about 90 degrees. Sometimes, the patient will be given a drug, such as Glyceryl trinitrate (nitroglycerin) or isoproterenol, to create further susceptibility to the test. The test either ends when the patient faints or develops other significant symptoms, or after a set period (usually from 20 to 45 minutes, depending on the facility or individualized protocol). The considered model is still given by 4.1.1, 4.1.2, 4.1.3. As inflow condition the valve model proposed in 3.7.1 is used, where the left ventricular pressure is prescribed equal to

$$p_{LV}(t) = p_{ext} + 3.75 \frac{HR}{75} 10^{-4} \sin \frac{\pi t}{\tau},$$

with HR representing the heart rate and τ the duration of the systole, taken to be a quarter of the heart beat ($\tau = 15/HR$). This model accounts for the fact that peak amplitude of the left

ventricular pressure depends on the heart rate. The terminal reflection coefficient has been chosen as terminal condition.

The labeling of the edges is taken from [1].
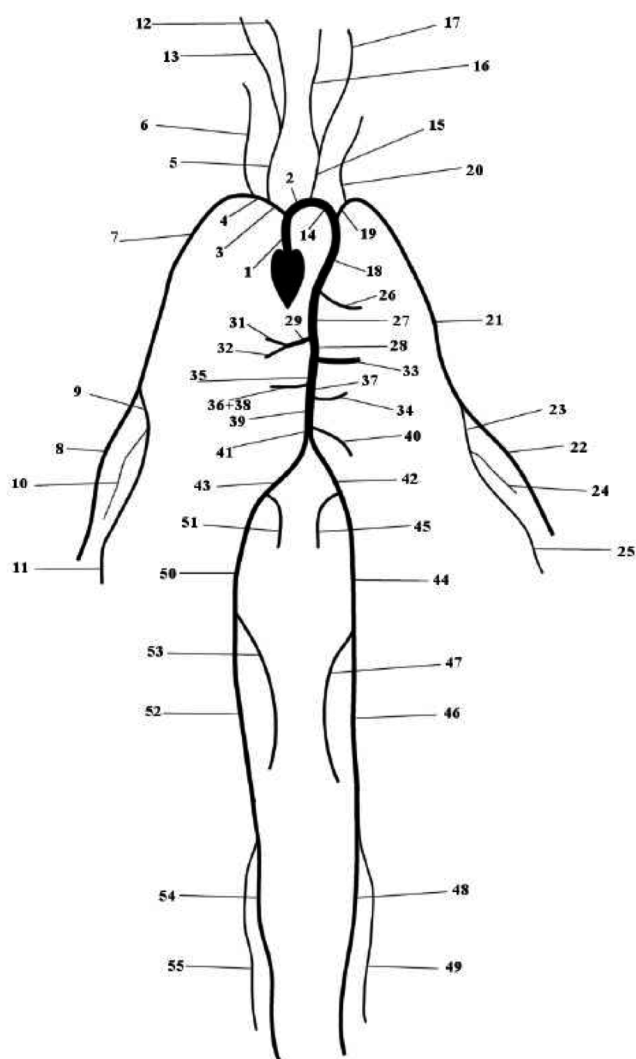
**Figure 4.18** The spatial domain is a 55-edge network.

Input data, such as length, radius, terminal coefficient and β for each edge have been taken from the following table [15].

Table 4.2 Data used in the computational model of the 55 arteries.

| #	Name of artery	Length (cm)	Area (cm^2)	β (Kg/s^2)	R_t
1	Ascending Aorta	4.0	5.983	388	-
2	Aortic Arch I	2.0	5.147	348	-
3	Brachiocephalic	3.4	1.219	932	-
4	R. Subclavian I	3.4	0.562	1692	-
5	R. Carotid	17.7	0.432	2064	-
6	R. vertebral	14.8	0.123	10360	0.906
7	R. Subclavian II	42.2	0.510	1864	-
8	R. Radial	23.5	0.106	11464	0.82
9	R. Ulnar I	6.7	0.145	8984	-
10	R. Interosseus	7.9	0.031	51576	0.956
11	R. Ulnar II	17.1	0.133	9784	0.893
12	R. Internal Carotid	17.6	0.121	10576	0.784
13	R. External Carotid	17.7	0.121	9868	0.79
14	Aortic Arch II	3.9	3.142	496	-
15	L. Carotid	20.8	0.430	2076	-
16	L. Internal Carotid	17.6	0.121	10576	0.784
17	L. External Carotid	17.7	0.121	9868	0.791
18	Thoracic Aorta I	5.2	3.142	496	-
19	L. Subclavian I	3.4	0.562	1664	-
20	Vertebral	14.8	0.123	10360	0.906
21	L. Subclavian II	42.2	0.510	1864	-
22	L. Radial	23.5	0.106	11464	0.821
23	L. Ulnar I	6.7	0.145	8984	-
24	L. Interosseus	7.9	0.031	51576	0.956
25	L. Ulnar II	17.1	0.133	9784	0.893
26	Intercostals	8.0	0.196	35.40	0.627
27	Thoracic Aorta II	10.4	3.017	468	-
28	Abdominal I	5.3	1.911	668	-
29	Celiac I	2.0	0.478	1900	-
30	Celiac II	1.0	0.126	7220	-
31	Hepatic	6.6	0.152	4568	0.925
32	Gastric	7.1	0.102	6268	0.921
33	Splenic	6.3	0.238	3324	0.93
34	Superior Mesenteric	5.9	0.430	2276	0.934
35	Abdominal II	1.0	1.247	908	-
36	L. Renal	3.2	0.332	2264	0.861
37	Abdominal III	1.0	1.021	1112	-
38	R. Renal	3.2	0.159	4724	0.861
39	Abdominal IV	10.6	0.697	1524	-
40	Inferior Mesenteric	5.0	0.080	7580	0.918
41	Abdominal V	1.0	0.578	1596	-
42	R. Common Iliac	5.9	0.328	2596	-
43	L. Common Iliac	5.8	0.328	2596	-
44	L. External Iliac	14.4	0.252	5972	-
45	L. Internal Iliac	5.0	0.181	12536	0.925
46	L. Femoral	44.3	0.139	10236	-
47	L. Deep Femoral	12.6	0.126	10608	0.885
48	L. Posterior Tibial	32.1	0.110	23232	0.724
49	L. Anterior Tibial	34.3	0.060	36972	0.716
50	R. External Iliac	14.5	0.252	5972	-
51	R. Internal Iliac	5.1	0.181	12536	0.925
52	R. Femoral	44.4	0.139	10236	-
53	R. Deep Femoral	12.7	0.126	10608	0.888
54	L. Posterior Tibial	32.3	0.110	23232	0.724
55	R. Anterior Tibial	34.4	0.060	36972	0.716

A 4-second simulation of the entire 55-edge network with variable external pressure (to account for respiration) is performed. The timing of the heart beat and respiratory cycle are taken from real data collected on a healthy individual in the physiology lab at University of Colorado (see Figure 4.19).
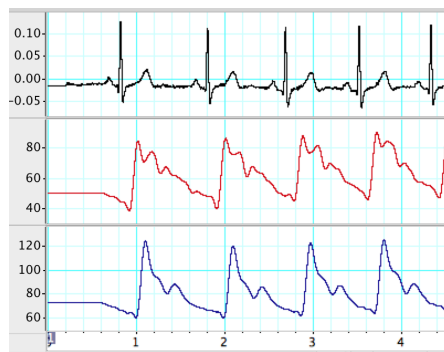

Figure 4.19 Real data for EKG (black), middle cerebral artery flow velocity in cm/s (red) and arterial blood pressure in mmHg (blue).

Since pressure and flow data are collected only at two sites in the network (radial artery for pressure and middle cerebral artery for flow), the simulation accomplishes to describe the dynamics in all other edges, hence completing the *picture* of the entire network. While the focus was on developing a working model, no data fitting was done for pressure and flow.
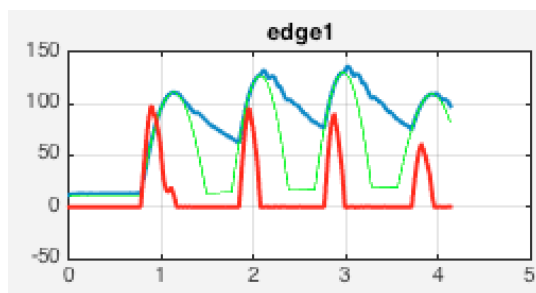
Figure 4.20 Simulated data in edge 1 (ascending aorta). Red line is the flow velocity (cm/s), blue is the arterial pressure (mmHg) and green line is the left ventricular pressure.
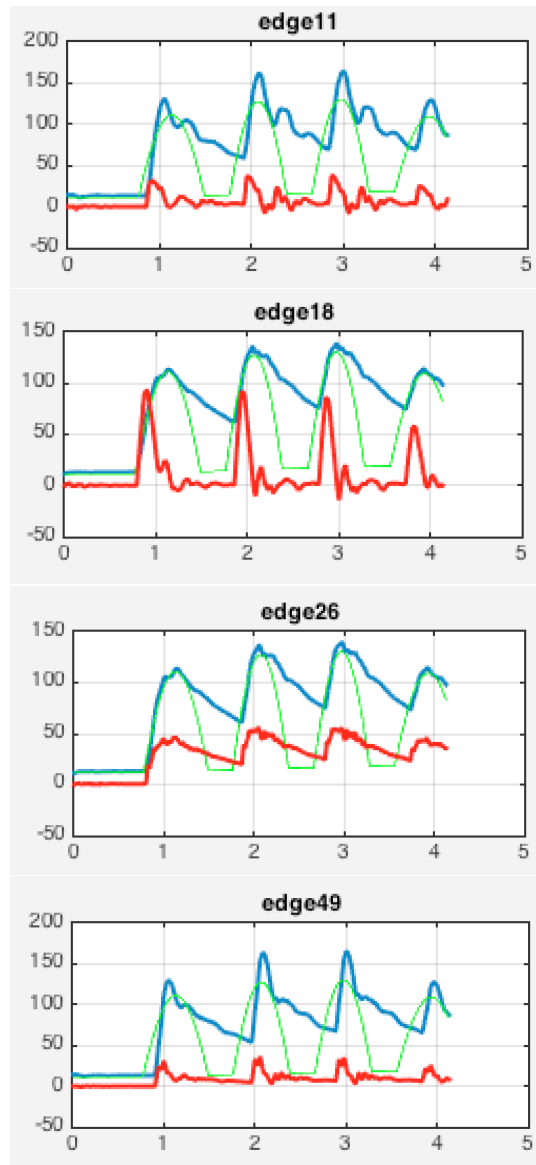
Figure 4.21 Simulated data in edge 11 (right ulnar artery), 18 (thoracic aorta), 26 (intercostal artery) and 49 (anterior tibial artery). Red line is the flow velocity (cm/s), blue is the arterial pressure (mmHg) and green line is the left ventricular pressure.

In the root edge (edge 1) the valve in action is showed: the valve

is closed hence zero flow goes through it when the left ventricular pressure is lower than the aortic pressure; the valve opens when the left ventricular pressure exceeds the aortic pressure. The timing of the opening of the valve is important, since it determines the total amount of cardiac output. At the other extreme, in edge 49, the pulsatility of the flow is minimal, but still the influence of the respiratory cycle is evident.

There are several noticeable features in this simulation results. The edges depicted in Figures 4.2-4.2 are chosen to illustrate the various aspects of the dynamics. Firstly, the slow variation of the left ventricular pressure (e.g. due to respiration) causes visible variation in the systolic pressure. Secondly, the characteristics of the pressure and flow dynamics is significantly different across the network: in some parts of the network there is small amount of backflow (e.g. edge 11, 18) while in others there is no backflow, (e.g. edge 26). In fact backflow is significant in edges 4, 7, 19 and 21 (only edge 4 is depicted below). Backflow is known to be physiological.
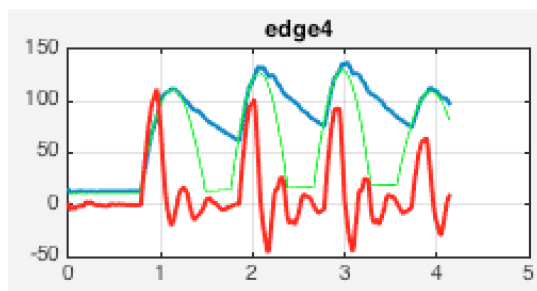
Figure 4.22 Simulated data in edge 4 (subclavian artery). For the color coding we refer to Figures 4.2-4.2.

For the remaining of this section, the numerical model to a different scenario is applied, that is a tilt table test: the body is initially on a horizontal bed, with no orthostatic pressure differences throughout the network. After 2 seconds, a tilt of the table is performed, in such a fashion that the level of the heart remains

the same. This means that the majority of the body is sent downward with the exception of the head and shoulders, creating an added orthostatic pressure value in most parts of the network.

Mathematically, this translates to a modification of the external pressure in the working model, to account for the gravitational effect (orthostatic pressure) as it appears during the tilt table test (see e.g. [26]).

$$p_{ext} = p_{ext}(t) = \rho g h(t) = \rho g \Delta h \sin \alpha t$$

where $\alpha = \frac{\pi}{2}$ is the angular velocity, chosen in such a way that after 1 second the tilt table is in upright position, $g = 9.8 m/s^2$ is the gravitational constant. Δh is elevation change between the middle of the edge and the heart when the person is upright. Δh can be positive (if the edge is below the heart) or negative (for edges that lie above the heart level.) Depending on what the center of the tilt is, Δh values would have more negative values.
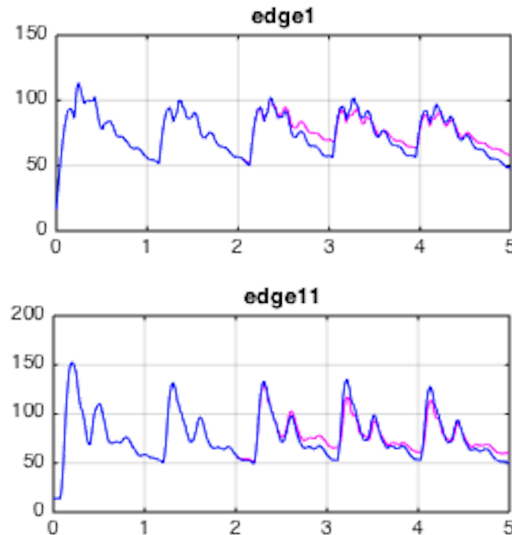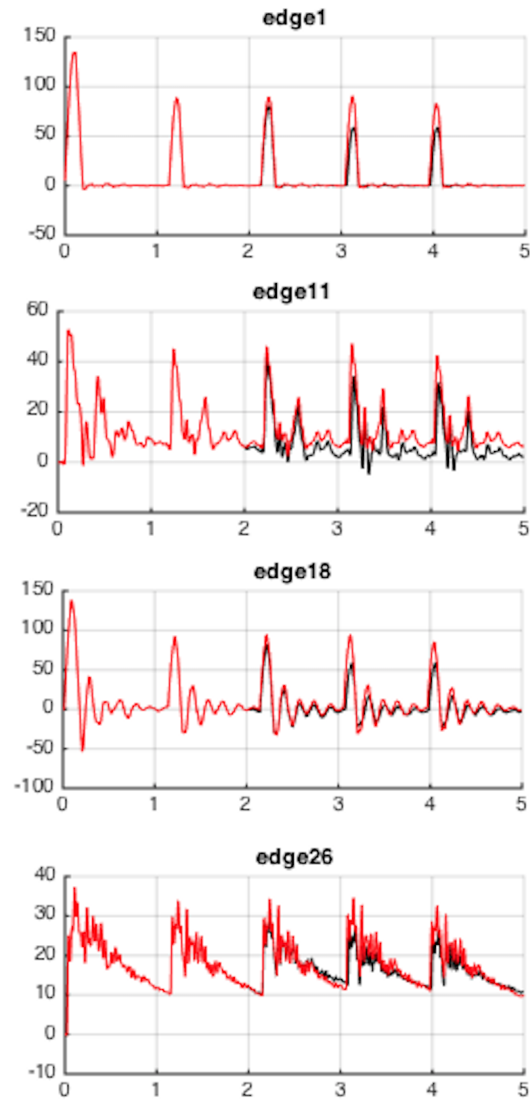

Figure 4.23 Comparison between the simulated pressure data (in mmHg) in normal conditions (blue) and in presence of the tilt (magenta) in edge 1 (ascending aorta) and 11 (right ulnar artery).
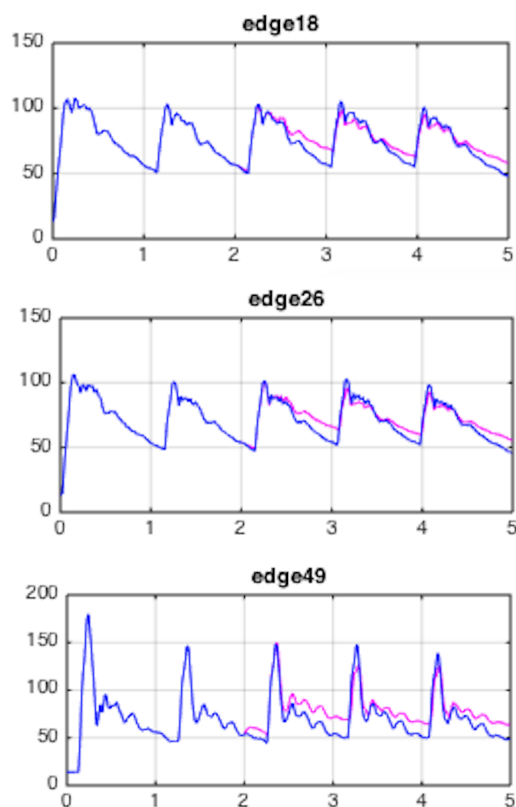
Figure 4.24 Comparison between the simulated pressure data (in mmHg) in normal conditions (blue) and in presence of the tilt (magenta) in edge 18 (thoracic aorta), 26 (intercostal artery) and 49 (anterior tibial artery)

Next the simulated data for the flow velocity for both horizontal position and during and after tilt are displayed, choosing the same edges as for pressure.

The tilt is performed for 1 second (seconds 2-3 after the beginning of the simulations), time in which the table is raised from horizontal to vertical positions. Then the table is left at that level.

Figure 4.25 Comparison between the simulated flow velocity data (in cm/s) in normal conditions (blue) and in presence of the tilt (magenta) in edges 1, 11, 18 and 26.
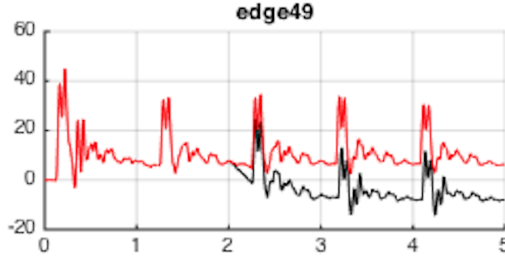
Figure 4.26 Comparison between the simulated flow velocity data (in cm/s) in normal conditions (blue) and in presence of the tilt (magenta) in edge 49.

Note that several edges come with negative external pressure. Nevertheless, the simulated data shows an increase of diastolic pressure throughout the board. At the same time, the picture with the flow pattern is much more diverse, several edges exhibiting a drop in flow velocity. The simulations are done without changing the heart rate calculations, for clarity of the comparison. In reality there is a response of the HR to the change in pressures (baroreceptor control), which would further alter the flow pattern. But even in absence of this complexity, it is possible to see that the systolic pressure is decreased immediately after the end of the tilt period, while the diastolic pressure is increased.

4.3 Optimization of mean arterial pressure

In this paragraph, the model considered is always the some (4.1.1, 4.1.2, 4.1.3), but a different choice for the pressure is done. The inertial effect of the wall motion is included, described by the wall displacement $\eta = \eta(x, t)$:

$$\eta = r - r_0 = \frac{1}{\sqrt{\pi}}(\sqrt{A} - \sqrt{A_0}).\qquad(4.3.4)$$

and hence the pressure is (see [8], [14])

$$p = p_{ext} + \frac{\beta}{r_0^2}\eta + \rho_\omega h \frac{\partial^2 \eta}{\partial t^2} = p_{ext} + \frac{\beta}{A_0}(\sqrt{A} - \sqrt{A_0}) + m\frac{\partial^2 A}{\partial t^2}, \quad (4.3.5)$$

where $r(x,t)$ is the radius, $r_0 = r(x,0)$, $A_0 = A(x,0)$, p_{ext} is the external pressure, $\beta = \frac{E}{1-\sigma^2}h$, σ is the Poisson ratio (usually taken to be $\sigma = \frac{1}{2}$), E is Young modulus, h is the wall thickness, $m = \frac{\rho_\omega h}{2\sqrt{\pi A_0}}$, ρ_ω is the density of the wall.
As inflow condition, the valve model presented in the previous chapter is considered, and the terminal reflection coefficient is used for the terminal condition.
Because of the addition of this extra term, the following system:

$$\begin{cases} A_t + (Au)_x = 0, \\ \left(u - \frac{\rho_\omega h r_0}{2\rho}u_{xx}\right)_t + \left(\frac{1}{2}u^2 + \frac{Eh}{\rho r_0^2}\left(\sqrt{A} - \sqrt{A_0}\right)\right)_x = f, \end{cases} \quad (4.3.6)$$

is obtained, which can be written in compact form:

$$\frac{\partial \mathbf{U}}{\partial t} + \frac{\partial \mathbf{F}(\mathbf{U})}{\partial x} = \mathbf{S}(\mathbf{U}), \quad (4.3.7)$$

where

$$\mathbf{U} = \begin{pmatrix} A \\ v \end{pmatrix}, \quad \mathbf{F}(\mathbf{U}) = \begin{pmatrix} Au \\ \frac{1}{2}u^2 + \frac{Eh}{\rho r_0^2}\left(\sqrt{A} - \sqrt{A_0}\right) \end{pmatrix},$$

$$\mathbf{S}(\mathbf{U}) = \begin{pmatrix} 0 \\ f \end{pmatrix}, \quad (4.3.8)$$

and $u = D^{-1}v$ is the solution of the boundary value problem

$$u - \frac{\rho_\omega h r_0}{2\rho}u_{xx} = v, \quad (4.3.9)$$

together with boundary conditions that are indicated above.
To approximate the second order derivative of u, it is used the

spectral method involving Chebyshev differentiation matrixes, defined for the Chebyshev collocation points $\{x_j\}_{j=0,...,N}$ as follows (see [45]):

$$(D_N)_{00} = \frac{2N^2 + 1}{6}, \quad (D_N)_{NN} = -\frac{2N^2 + 1}{6},$$

$$(D_N)_{jj} = -\frac{x_j}{2(1 - x_j^2)}, \quad j = 1, ..., N - 1,$$

$$(D_N)_{ij} = \frac{c_i}{c_j} \frac{(-1)^{i+j}}{(x_i - x_j)}, \quad i \neq j, \ i, j = 0, ..., N - 1,$$

where

$$c_i = \begin{cases} 2, & i = 0 \text{ or } N, \\ 1, & \text{otherwise.} \end{cases}$$

This discretization can be coupled with the discontinuous Galerkin scheme described above, by matching the solution at Chebyshev points, performing the derivative using these points, then returning back to the Legendre points.

The numerical model just developed is used to perform an optimization scenario. The goal is to maintain the mean arterial pressure close to a prescribed reference value (P_{ref}), in presence of external pressure changes. The external pressure p_{ext} is taken to vary with time, to mimic the respiratory cycle, according to

$$p_{ext}(t) = 14 + 7.5 \sin 2t \ (\text{mmHg}).$$

Here an arterial segment of length 0.5 m is considered. The following parameter values are used throughout the sequel: $\mu = 3 \times 10^{-5}$ $mmHg$ (viscosity of the blood), $\rho = 1050 \ Kg/m^3$ (blood density), $P_{ref} = 100 \ mmHg$ and the total time of the simulation is $t_{final} = 10 \ sec$.

The goal is to find the optimal HR (and later also terminal resistance R_t - assumed constant during one heartbeat) which leads to

the minimization of the following cost functional

$$J = \int_{t_0}^{t_0+T_{pulse}} |P_{avg}(t) - P_{ref}|^2 \, dt =$$

$$= \int_{t_0}^{t_0+T_{pulse}} \left| \frac{1}{L} \int_0^L p(x,t) \, dx - P_{ref} \right|^2 \, dt.$$

Here the integration is done using an entire heartbeat, with duration $T_{pulse} = 60/HR$. The systolic period is taken to be consistently one quarter of T_{pulse}.

Upon optimization on HR alone, the following $10 - sec$ recording of the aortic pressure is obtained, plotted together with the left ventricular pressure. The first heartbeat has not been included in the plot, since the initial condition is anomalous and does not affect the subsequent dynamics.
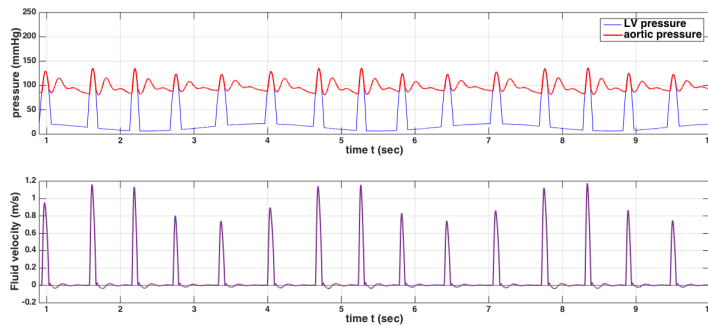

Figure 4.27   10-second recording of pressure and velocity with optimal HR.
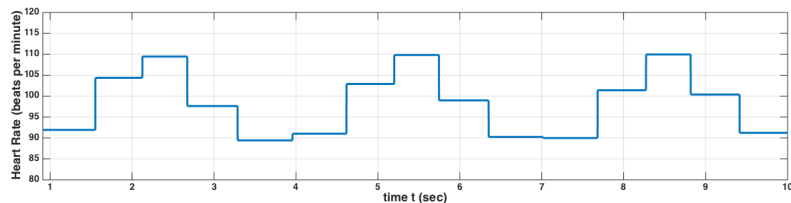
Figure 4.28   Optimal HR for maintaining constant mean pressure at 100 $mmHg$ ($R_t = 0.9$).

When including the terminal resistance as one of the optimization parameters, it is possible to notice a different pattern of the optimal HR, which is to be expected. The variability of the HR and terminal resistance R_t are shown in the figures below:
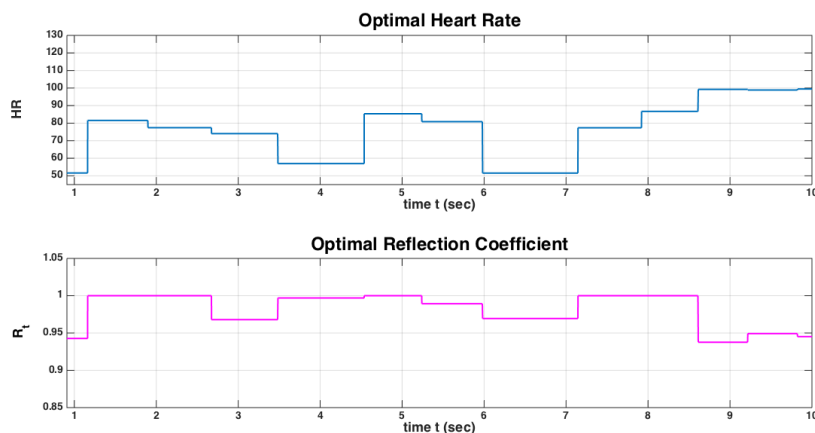

Figure 4.29 Optimal HR and R_t for maintaining constant mean pressure at 100 mmHg.

Observe that the terminal resistance R_t is close to 1, which means that there is almost a complete reflection of the characteristic waves and almost complete blockage in the terminal site. HR varies in sync with the respiratory cycle, but the presence of peripheral resistance mechanism is breaking the periodicity of the HR variability, which is what is observed in the real system. Also note that comparing this range of HR with the results above (when only HR was used in optimization, keeping $R_t = 0.9$ fixed), can lead to the conclusion that in order to maintain a prescribed mean pressure over one heart beat increasing the R_t (even to its maximal value) is more efficient than increasing the HR. Naturally, the consideration of a single arterial segment (aorta) avoids the effects of the complexity of the vascular network, which would add additional irregular behavior in the HR variability.

Using this method, it is also possible to compare dispersion ($\rho_w > 0$) and dispersionless ($\rho_w = 0$) models. A rather high density for

the wall is chosen, in order to underline the difference. The result of the simulation is given below:
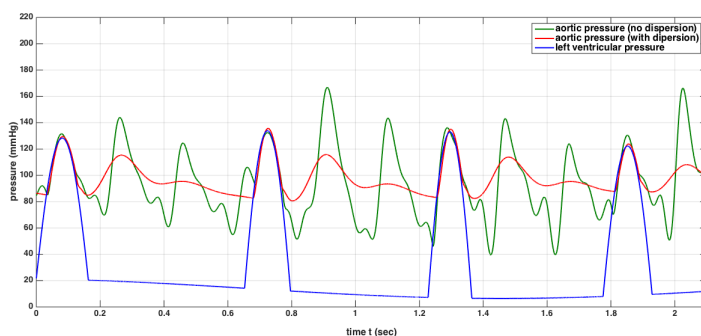
Figure 4.30 Comparison between aortic pressure in absence of dispersion (green) and aortic pressure in presence of dispersion (red).

Observe that for the dispersionless case, the multiple peaks between heartbeats indicate that the waves which originate during a systole reflect off the boundaries and travel back and forth (with decreased amplitudes) during the diastole. These can be used to compute the speeds of the pulse waves in relation to the heart rates, similar to [20].

In the dispersive case, the pressure waves have much fewer oscillations than in the dispersionless one. This can be explained by the higher density of the wall, hence higher wall inertia, and consequently fewer transversal oscillations. Since these are temporal recordings at one spatial location, these show an averaging effect due to dispersion of flow along the vessel, and not a dampening of the waves. In simulations a greater degree of the averaging is also witnessed, when the wall density increase. If on the other hand we keep all the parameters (e.g. wall density etc) but we consider a shorter length of the vessel M, then by rescaling the spatial variable $\tilde{x} = x/M$, one obtains a similar effect - of increasing the value of the wall density, and hence of averaging the pressure pulses originating from the left ventricle. Another effect which can be captured in our numerical model is the variable (along the vessel length) radii and elasticity.

Conclusions

Simulations of the mathematical models involving partial differential equations on networks such as those presented here reveal macroscopic phenomena that cannot be anticipated by looking at individual edge dynamics. The nature of phenomena such as appearance of low frequency oscillations in the network, time of recovery after blockage in a network is removed, truncation of a fractal tree network are revealed through these simulations and can help further study of the real phenomena observed in physiological conditions. Interpreting physically correct boundary conditions remains crucial for modeling long term behavior of the network dynamics. The numerical model, which has been developed here to simulate variable external conditions and their effect on the cardiovascular system, is presented in certain realistic physiological situations. The model includes a valve at the inflow, which accounts for change in the systolic pressure, while the variability of the diastolic pressure is due primarily to the external conditions. The focus has been on comparing the dynamics in various parts of the network in presence and absence of the changes. In addition, the obtained numerical optimization results are relevant for understanding how boundary control affects the dynamics of the pressure and flow in an arterial segment, via the valve model at the root of the vascular network and via peripheral resistance model at the outflow. The consideration of a single edge can be viewed as certainly restrictive from a physiological point of view, but can help in further studies where the entire vascular network is considered. The models described in this thesis can have other applications. The 1-D formulation can contribute to determine

the effects of medications, which changes the hemodynamic pro-
prieties of the arterial system, on the shape of the pulse waves. It
is possible to conduct such investigations supposing that this med-
ications determines some changes in compliance, geometry and/or
peripheral resistance of the arterial system, and compare the wave
form given by the 1-D simulation with the ones measured *in vivo*.
In addition, the introduced model can also be applied to study
the effect of some cardiovascular pathologies of the blood flow in
the arteries. For example, it is possible to analyze the effects of
arterial bleedings on the propagation of the pulse wave consider-
ing a 1-D model of the most wide arterial domain, simulating a
bleeding as a 1-D artery bifurcated from the point of the bleeding,
and finishing with a negative terminal reflection coefficient.

Bibliography

[1] J. Alastruey, *Numerical Modelling of Pulse Wave Propagation in the Cardiovascular System: Development, Validation and Clinical Applications*, PhD Thesis, Imperial College London, 2006.

[2] W.E. Bodley, *The non-linearities of arterial blood flow*, Phys. Med. Biol., 16:663-672, 1971.

[3] A. Bressan, *Hyperbolic Systems of Conservation Laws - The One-dimensional Cauchy Problem*, Oxford Univ. Press, 2000.

[4] A. Bressan, G. Crasta, B. Piccoli, *Well-Posedness of the Cauchy Problem for $n \times n$ Systems of Conservation Laws*, Memoirs of the American Mathematical Society, vol. 146, n. 694, 2000.

[5] B.S. Brook, S.A.E.G. Falle, T.J. Pedley, *Numerical solutions for unsteady gravity-driven flows in collapsible tubes: evolution and roll-wave instability of a steady state*, J. Fluid Mech., 396:223-256, 1999.

[6] B.S. Brook, T.J. Pedley, *A model for time-dependent flow in (giraffe jugular) veins: uniform tube properties*, J. Biomech., 35:95-107, 2002.

[7] S. Canic, E.H. Kim, *Mathematical analysis of the quasilinear effects in a hyperbolic model blood flow through compliant axisymmetric vessels*, Mathematical Methods in the Applied Sciences, 26: 1161-1186. 10.1002/mma.407, 2003.

[8] R.C. Cascaval, *A Boussinesq model for pressure and flow velocity waves in arterial segments*, Math Comp Simulation. 82(6), 1047-1055, 2012.

[9] Q. Chen, L. Jiang, C. Li, D. Hu, J. Bu, et al., *Haemodynamics-Driven Developmental Pruning of Brain Vasculature in Zebrafish*, PLoS Biol. 10(8): e1001374, doi:10.1371/journal.pbio.1001374, 2012.

[10] D. Elad, D. Katz, E. Kimmel, S. Einav, *Numerical schemes for unsteady fluid flow through collapsible tubes*, J. Biomed. Eng., 13:10-18, 1991.

[11] L.C. Evans, R. F. Gariepy, *Measure Theory and Fine Properties of Functions*, Studies in Advanced Mathematics, CRC Press, Boca Raton, FL, 1992.

[12] L. Formaggia, F. Nobile, A. Quarteroni, A. Veneziani, *Multiscale modelling of the circulatory system: a preliminary analysis*, Computing and Visualization in Science, 2:75-83, 1999.

[13] L. Formaggia, J.F. Gerbeau, F. Nobile, A. Quarteroni, *On the Coupling of 3D and 1D Navier-Stokes Equations for Flow Problems in Compliant Vessels*, Computer Methods in Applied Mechanics and Engineering, 191:561-582, 2001.

[14] L. Formaggia, D. Lamponi, A. Quarteroni, *One-dimensional models for blood flow in arteries*, J. Eng Math. 47, 251-276, 2003.

[15] L. Formaggia, D. Lamponi, M. Tuveri, A. Veneziani, *Numerical modeling of 1D arterial networks coupled with a lumped parameters description of the heart*, Comp. Meth. Biomech. Biomed. Eng., 9, 273-288, 2006.

[16] L. Formaggia, A. Veneziani, *Reduced and multiscale models for the human cardiovascular system*, Politecnico di Milano, 2003.

[17] L. Formaggia, A. Quarteroni, A. Veneziani, *Cardiovascular Mathematics: Modeling and Simulation of the Circulatory System*, Volume 1, Springer-Verlag Italia, 2009:395-446, 2009.

[18] M. Kumada, T. Azuma, K. Matsuda, *The cardiac output-heart rate relationship under different conditions*, Jpn J Physiol., 17, 538-555, 1967.

[19] C.W. Li, H.D. Cheng, *A nonlinear fluid model for pulmonary blood circulation*, J. Biomech., 26:653-664, 1993.

[20] J.S. Lillie et al., *Pulse Wave Velocity Prediction and Compliance Assessment in Elastic Arterial Segments*, Cardiovascular Engineering and Technology, 6 (1), 49-58, 2015.

[21] D.A. McDonald, *Blood flow in arteries*, Edward Alnord, London, 1974.

[22] V. Milisic, A. Quarteroni, *Analysis of lumped parameter models for blood flow simulations and their relation with 1D models*, ESAIM-Mathematical Modelling and Numerical Anslysis, 38: 613-632. 10.1051/m2an:2004036, 2004.

[23] B.S. Mordukhovich, *Variational Analysis and Generalized Differentiation II. Applications*, Springer, 2006.

[24] A. Noack, A. Walther, *Adjoint concepts for the optimal control of Burgers equation*, Comput Optim Applic 36m 109-133, 2007.

[25] M.S. Olufsen, *Structured tree outflow condition for blood flow in larger systemic arteries*, Am J Physiol, 276: H257-268, 1999.

[26] M.S. Olufsen, J.T. Ottesen, H.T. Tran, L.M. Ellwein, L.A. Lipsitz, V. Novak, *Blood pressure and blood flow variation during postural change from sitting to standing: model development and validation*, J Appl Physiol 99: 1523-1537, 2005.

[27] G.L. Papageorgiou, N.B. Jones, *Arterial system configuration and wave reflection*, J. Biomed. Engng., 9:299-301, 1987.

[28] K.H. Parker, C.J.H. Jones, *Forward and backward running waves in the arteries: analysis using the method of characteristics*, J. Biomech. Engng., 112:322-326, 1990.

[29] G. Pontrelli, E. Rossoni, *Numerical Modeling of the Pressure Wave Propagation in the Arterial Flow*, International Journal for Numerical Methods in Fluids, 43:651-671, 2003.

[30] G. Pontrelli, *A multiscale approach for modelling wave propagation in an arterial segment*, Comput. Methods Biomech. Biomed. Engin., 7:79-89, 2004.

[31] G. Porenta, D.F. Young, T.R. Rogge, *A finite-element model of blood flow in arteries including taper, branches, and obstructions*, J. Biomech. Eng., 108:161-167, 1986.

[32] A. Quarteroni, *Modellistica Matematica per il Sistema Cardiovascolare*, Leadership Medica, Anno XX-N.10/2004.

[33] P. Reymond, F. Merenda, F. Perren, D. Rufenacht, N. Stergiopulos, *Validation of a one-dimensional model of the systemic arterial tree*, Am. J. Physiol. Heart. Circ. Physiol., 297:H208-222, 2009.

[34] E. Rooz, D.F. Young, T.R. Rogge, *A finite-element simulation of pulsatile flow in flexible obstructed tubes*, J. Biomech. Eng., 104:119-124, 1982.

[35] I.M. Ross, M. Karpenko, *A review of pseudospectral optimal control: From theory to flight*, Annual Reviews in Control 36, 182-197, 2012.

[36] P. Segers, P. Verdonck, *Arterial Mechanics*, Notes published by IBITECH, University of Ghent, Belgium, 2003.

[37] S.J. Sherwin, V.E. Franke, J. Peirò, K.H. Parker. *One-dimensional modelling of a vascular network in space-time variables*, J. Engng. Maths., 47:217-250, 2003.

[38] S.J. Sherwin, l. Formaggia, V.E. Franke Formaggia L, Peir, *Computational Modeling of 1D Blood Flow with Variable Mechanical Properties and Application to the Simulation of Wave Propagation in the Human Arterial System*, International Journal for Numerical Methods in Fluids, 43:673-700, 2003.

[39] Y. Shi, P. Lawford, R. Hose, *Review of Zero-D and 1-D Models of Blood Flow in the Cardiovascular System*, BioMedical Engineering OnLine, 2011.

[40] N.P. Smith, A.J. Pullan, P.J. Hunter. *An anatomically based model of transient coronary blood flow in the heart*, SIAM J. Appl. Math., 62:990-1018, 2001.

[41] B.N. Steele, J. Wan, J.P. Ku, T.J. Hughes, C.A. Taylor, *In vivo validation of a one-dimensional finite-element method for predicting blood flow in cardiovascular bypass grafts*, IEEE Trans. Biomed. Eng., 50:649-656, 2003.

[42] V.L. Streeter, W.F. Keitzer, D.F. Bohr, *Pulsatile Pressure and Flow through Distensible Vessels*, Circulation Research, XIII:3-20, 1963.

[43] I. Surovtsova, *Effects of compliance mismatch on blood flow in an artery with endovascular prosthesis*, J. Biomech., 38:2078-2086, 2005.

[44] J. Wan, B. Steele, S.A. Spicer, S. Strohband, G.R. Feijoo, T.J. Hughes, C.A. Taylor, *A one-dimensional finite element method for simulation-based medical planning for cardiovascular disease*, Comput Methods Biomech. Biomed. Engin., 5:195-206, 2002.

[45] L.N. Trefethen, *Spectral Methods in Matlab*, SIAM, 2000.

[46] I. Vigono-Clementel, C.A. Figueroa, K.E Jansen, C.A. Taylor, *Outflow boundary conditions for three-dimensional finite element modeling of blood flow and pressure in arteries*, Computer methods in applied mechanics and engineering, 195: 3776-3796. 10.1016/j.cma.2005.04.014, 2006.

[47] J.J. Wang, K.H. Parker, *Wave propagation in a model of the arterial circulation*, J. Biomech., 37:457-470, 2004.

[48] J.J. Wang, A.B. O'Brien, N.G.Shrive, K.H.Parker, J.V. Tyberg, *Time-domain representation of ventricular-arterial coupling as a windkessel and wave system*, Am. J.Heart Circ. Physiol., 284:H1358-H1368, 2003.

[49] H. Watanabe, S. Sugiura, H. Kafuku, T. Hisada, *Multiphysics simulation of left ventricular filling dynamics using fluid-structure interaction finite element method*, Biophys J., 87:2074-2085, 2004.